9-1-2002

Mean Performance Optimization of an Orbiting Distributed Aperture by Warped Aperture Image Plane Comparisons

Timothy W. Parker

MEAN PERFORMANCE OPTIMIZATION OF AN ORBITING DISTRIBUTED APERTURE BY WARPED APERTURE IMAGE PLANE COMPARISONS

DISSERTATION

Timothy Wayne Parker
Major, USAF

AFIT/DS/ENY/02-3

DEPARTMENT OF THE AIR FORCE
AIR UNIVERSITY

AIR FORCE INSTITUTE OF TECHNOLOGY

Wright-Patterson Air Force Base, Ohio

Report Documentation Page

Report Date	Report Type	Dates Covered (from... to)
10 Sep 02	Final	Sep 99 - Sep 02

Title and Subtitle Mean Performance Optimization of an Orbiting Distributed Aperture by Warped Aperture Image Plane Comparisons	**Contract Number**
	Grant Number
	Program Element Number
Author(s) Major Timothy W. Parker, USAF	**Project Number**
	Task Number
	Work Unit Number
Performing Organization Name(s) and Address(es) Air Force Institute of Technology Graduate School of Engineering and Management (AFIT/EN) 2950 P Street, Bldg 640 WPAFB, OH 45433-7765	**Performing Organization Report Number** AFIT/DS/ENY/02-3
Sponsoring/Monitoring Agency Name(s) and Address(es) Dr. Andrew Sparks AFRL/VACA 2210 Eighth Street WPAFB OH 45433-7521	**Sponsor/Monitor's Acronym(s)**
	Sponsor/Monitor's Report Number(s)

Distribution/Availability Statement
Approved for public release, distribution unlimited

Supplementary Notes
The original document contains color images.

Abstract
This work models the aggregate performance of satellite receiver formations functioning as orbiting interferometers as compared to filled apertures of similar geometries. These models facilitate selecting initial conditions for formations such that their control-free dynamics yield interferometry performance with minimal errors as compared to the filled apertures. The solution method draws on the dynamic models of an orbiting planar satellite formation to define the size and shape of a reference aperture and to define the degrees of freedom for the formation memebers. The paths of formation elements yield geometries for which the aggregate performance of the array of discrete receivers may be calculated. The objective of the optimization process is therefore minimizing the time-average square of the difference between the filled aperture's intensity map and that generated by the discrete receiver array. This yields a formation whose configureation offers minimum errors for imaging processes beginning at any arbitrary start time. The problem as posed is non-convex, and requires implementation of a global search method. Genetic algorithms are used. The solution method includes a new analytic solution for the intensity map of an elliptical aperture and a technique for generalizing this solution to inclue the efects of non-ideal viewing geometries.

Subject Terms
Satellite Formations, Intergerometry, Optimization, Genetic Algorithms, Synthetic Apertures

Report Classification unclassified	**Classification of this page** unclassified

Classification of Abstract unclassified	**Limitation of Abstract** UU
Number of Pages 156	

The views expressed in this dissertation are those of the author and do not reflect the official policy or position of the Department of Defense or the United States Government.

AFIT/DS/ENY/02-3

MEAN PERFORMANCE OPTIMIZATION OF AN ORBITING DISTRIBUTED APERTURE BY WARPED APERTURE IMAGE PLANE COMPARISONS

DISSERTATION

Presented to the Faculty

Graduate School of Engineering and Management

Air Force Institute of Technology

Air University

Air Education and Training Command

in Partial Fulfillment of the Requirements for the

Degree of Doctor of Philosophy

Timothy Wayne Parker, B.S., M.E.

Major, USAF

September, 2002

AFIT/DS/ENY/02-3

MEAN PERFORMANCE OPTIMIZATION OF AN ORBITING DISTRIBUTED APERTURE BY WARPED APERTURE IMAGE PLANE COMPARISONS

Timothy Wayne Parker, B.S., M.E.

Major, USAF

Approved:

Lt Col David R. Jacques Thesis Advisor	Date
Dr. William E. Wiesel Committee Member	Date
Dr. Meir Pachter Committee Member	Date
Dr. Steven G. Tragesser Committee Member	Date
Dr. Gary B. Lamont Dean's Representative	Date

Robert A. Calico, Jr
Dean

Preface

I am deeply indebted to my advisor, Lt Col Dave Jacques, for his positive direction and steadfast "top cover" throughout this program. His willingness to spend the extra effort required to help a new-older student change fields and have a fighting chance made all the difference. His guidance in problem formulation and solution construction is evident throughout this work. I hope this dissertation reflects well upon his labors.

Dr. William Wiesel, Dr. Meir Pachter, and Dr. Steven Tragesser not only formed the rest of my very understanding committee, but offered hours of their office time to help piece together the wide ranging subject areas blended in this work. Dr. Wiesel in particular lent me his (occasionally frustrating) ability to see directly to the heart of interim problems, and greatly reduced the length of my solution efforts.

This work builds on the pioneering work done at the Massachusetts Institute of Technology by Edmund Kong, Dr. David Miller, and Dr. Raymond Sedwick. Their series of papers in *The Journal of the Astronautical Sciences*, reports to the TechSat 21 program, and some direct help via facsimile lent invaluable clarity and insight into formulating problems with workable solutions.

Outside of AFIT, I must acknowledge the support and encouragement from my folks who showed more than polite interest in my efforts and to the little guy that refocused my personal universe. My son's arrival punctuated the end of my prospectus research and proceeded to spice up the final year of work. He not only learned the attention grabbing power of the CPU reset button, but kept my study priorities in their proper order for the final phases of this program.

And bottom of the page but top of my list is my wife. She fully mastered the art of "That's nice, dear" and "Don't you have homework to do?" and persevered through more hours of solitude and more proof-reading sessions than any human should ever have to endure. No student could ever ask for a more positive cheerleader, partner, or spouse. (And she's really pretty, too.)

Timothy Wayne Parker

Table of Contents

Page

List of Figures

List of Tables

List of Symbols

Symbol — Page

Symbol Page

Symbol Page

Abstract

This work investigates the aggregate performance of satellite receiver formations functioning as orbiting interferometers as compared to filled apertures of similar geometries. The resulting models facilitate selecting initial conditions for formations such that their control-free dynamics yield interferometry performance with near-minimal errors as compared to the filled apertures. The solution method draws on the dynamic models of an orbiting planar satellite formation to define the size and shape of a reference aperture and to define the degrees of freedom for the formation members. The modelled paths of formation elements yield predictable geometries at any time for which the aggregate performance of the array of discrete receivers may be calculated. The objective of the optimization process is to minimize the time-averaged square of the difference between the filled aperture's intensity map and that generated by the discrete receiver array. This yields a formation whose configuration offers near-minimum errors for imaging processes beginning at any arbitrary start time. The problem as posed is non-convex, and requires implementation of a global search method. Genetic algorithms are used. The genetic algorithms construct populations of generic coefficients, adaptable to the number of degrees of freedom for each proposed formation. The fitness assigned to members of each population is the average aggregate error its formation generates over the simulation duration. The solution method includes a new analytic solution for the intensity map of an elliptical aperture and a technique for generalizing this solution to include the effects of non-ideal viewing geometries.

MEAN PERFORMANCE OPTIMIZATION OF AN ORBITING DISTRIBUTED APERTURE BY WARPED APERTURE IMAGE PLANE COMPARISONS

I. Introduction

1.1 Overview

The notion of creating satellite formations for distributed missions is by no means new, but has received renewed interest in the past few years. Distributing a satellite mission over a formation of smaller vehicles offers the potential advantages of very large (although sparse) effective apertures, modular maintainability and upgradability, graceful degradation, and greatly reduced life cycle costs.

Distributed satellite systems (DSSs) are among the most challenging conceptual design problems, since modelling such systems requires nonlinear, high order, often coupled mathematics [55, 54, 18]. The Air Force and NASA spurred feasibility research in the creation of distributed satellite missions through the TechSat 21 research initiative. The TechSat 21 program encouraged investigation into not only satellite formation dynamics, but also micro-satellite and micro-propulsion design, distributed mission architecture, sparse aperture sensing, collaborative behavior, and micro-nano-technology [41]. These investigations resulted in tremendous advancements in the science of modelling the dynamics of satellite formations and optimizing control use for their maintenance and reconfiguration. Other work has addressed the potential uses of formations for communications, radar, astronomy [6, 17], and moving target identification [38, 39]. Many of these works addressed optimization approaches for formations used for interferometry missions [9, 20, 23, 7].

This interdisciplinary work draws from the fields of astrodynamics, physics, electrical engineering, and mathematics. It melds the disparate sciences of orbital mechanics, optics, and optimization to build a solution methodology for shaping satellite formations. The basic nature of formations makes them attractive platforms for receiver arrays performing interferometry. Shaping a formation to optimize its performance is necessarily both an

optical problem and an orbital mechanics problem. Orbital mechanics restricts the design choices for formation shapes and dictates how receivers move within that formation. The science of optics defines both the performance of a filled aperture of size comparable to the formation and the aggregate performance of the formation's discrete receivers. Building these elements into the fitness model offers a methodical approach to minimizing the difference between the outputs of these two apertures by adjusting the defining parameters of the formation's members.

Optimal geometries are a key element in the employment of distributed receivers for astronomical observations [42, 28], but are not limited to stellar targets. Optimizing receiver arrays for point sources is a logical approach for maximizing performance in imaging very small targets. Literally dozens of metrics for performing formation optimization have been designed. Some minimize control usage or reconfiguration time. The thesis and series of papers by Sedwick, Miller, and Kong at MIT [21] optimized instantaneous performance of a formation by comparison to a filled aperture. This work generalizes this approach to minimize errors over an arbitrary imaging time. This approach requires taking into account the loci swept out by the formation receivers by shaping the reference aperture to match these loci. Therefore the control-free dynamics of a formation are used to define an appropriately shaped aperture, and candidate formations are compared to this baseline. The intensity map generated by a simple circular aperture is a well-known solution and is the reference nearly always used in previous works. Such a reference is inefficient since it inherently either includes receiver paths not unreachable due to the formation dynamics or ignores beneficial paths that are reachable. This work includes a new solution method for mapping physical distortions of a circular aperture from the physical or spatial frequency domain through the Point Spread Function into the spatial domain of the image intensity map. Developed first for an ideal viewing geometry, this solution method is then generalized to include the apparent aperture distortions generated by realistic, non-ideal viewing geometries.

The optimization task is therefore one of selecting the defining parameters of a formation such that the the average difference between a reference aperture's intensity map and that generated by the aggregate performance of the discrete receivers is minimized.

This turns out to be a non-convex problem. The lack of convexity is overcome by making a few simplifying assumptions and exploiting the powerful global search capabilities of genetic algorithms. The defining parameters of formation dynamics limit the number of degrees of freedom in a series of increasingly complex problems, each optimized by genetic search routines. As the simplifying assumptions are relaxed, the search procedure selects a growing set of generic coefficients each adaptable to the varying dimensionality of the increasing degrees of freedom. With greater numbers of receivers in the formation and increasing flexibility in their initial conditions, the discrete array's ability to synthesize the performance of a filled aperture grows rapidly. As the formation size grows, the aggregate error dwindles to near-zero indicating that the shaped aperture reference is indeed a valid ideal, theoretically reachable by an infinite number of receivers.

1.2 Research Contributions

Though this work relies heavily on the pioneering efforts of many experts in the fields of optics [13], interferometry [46, 35], orbital mechanics [50], and formation dynamics [56, 4], it offers significant advancement in several aspects of both formal problem definition and adaptation of global search algorithms for its solution. The purpose of this research is to encapsulate the relevant dynamics of satellite formations and the physics of interferometry, specifically as it relates to receiver arrays both liberated and restricted by placement in orbit. By applying the science of optics to both an aggregate aperture and a filled aperture, a metric is defined as a comparison of the two, then expanded to include time variations. Employing this as the measure of merit for simplified formations gives rise to a non-convex problem. The global search techniques of genetic algorithms are well suited to non-convex problems and provide acceptable numerical solutions. The specific contributions stemming from this problem definition and solution are as follows:

i. The model built in this research characterizes the process for building an intensity map generated by an aggregate aperture of discrete receivers, $\overline{\mathbf{I_P}}(\xi, \eta, t)$, and formalizes the mathematics for building a complete set of baselines for a generalized set of asymmetrically placed receivers.

ii. The second-order instantaneous metric of previous work [20] is extended to include variations over a finite dwell time. This metric holds the promise of yielding formations whose control-free motion yields near-minimal imaging errors for any arbitrary start time.

iii. The mathematically simple circular reference aperture is discarded in favor of more complex shapes which cover *all* available receiver loci and include *none* that are unreachable due to the formation dynamics.

iv. Both a numerical and an analytic solution are offered for the intensity map, $\mathbf{I_o}(\xi, \eta)$, of a filled *elliptical* aperture of arbitrary eccentricity. An aperture with this shape covers all relative loci of formation elements in control-free motion (as viewed from directly above). The intensity map offered by the analytic solution is shown to match the less efficient but mathematically simpler numerically derived map.

v. The analytic solution for an elliptical aperture is extended to include the distorting effects of general viewing geometries. These geometries are determined by the Keplerian elements defining the reference orbit and by the inertial locations of targets.

vi. The generalized aperture solution demonstrates a new technique for generating an analytic intensity map for *any* (circular or elliptical) aperture distorted as viewed from general locations. The solution method may readily be adapted for use with any orbital reference or target mapping convention.

vii. Global search techniques are adapted to generate generic coefficients which select the defining parameters of simplified formations. The generic coefficient approach allows for the selection of larger sets of defining parameters of each formation element without significant code rewriting. The varying dimensionality of these parameters is likewise transparent to the selection routine.

1.3 Dissertation Outline

This dissertation consists of 8 chapters, including this introduction. Chapter 2 reviews the extensive literature on modelling the dynamics of satellite formations and the limitations of several leading model solutions. Each model, despite extensive differences

in their formulations, is shown to limit the formation designer's choices to a maximum of four degrees of freedom per element.

Chapter 3 summarizes the basic science of interferometry from the nature of a single pair of interfered wave forms out to the synthesis of an entire aperture's intensity map. Chapter 4 reviews the extensive literature on moving interferometry-based receivers out to orbital platforms and the assumptions and limitations inherent in the various system descriptions. The analytic solutions for aggregate aperture performance are re-derived for symmetric arrays to provide background for the more general formalized treatment of asymmetric arrays. These are incorporated into the development of a time-averaged comparison metric. It formalizes the aggregate aperture construction, the selection of an appropriately shaped reference aperture, and determines a conservative size for the image plane over which the comparison is performed.

Chapter 5 takes the basic technique of integrating a point spread function, **PSF**, over an aperture to generate its intensity map and applies it to apertures with simple geometries. Beginning with a simple one-dimensional aperture (a slit), it is then applied to simple two-dimensional shapes. The elliptical aperture derivation at the end illustrates the basic technique for warping a circular intensity map in one direction, a technique generalized in chapter 7.

The nature of the optimization problems based on the metrics of chapter 4 is addressed in chapter 6. It begins with the simplest possible one-dimensional formation to illustrate the convexity of the problem and gradually expands the trial formations to more realistic relative geometries and more freedom for receiver loci selection. Chapter 7 finally adds in the apparent distortions caused by viewing formations from non-ideal directions. These distortions affect both the receiver loci and the filled aperture. Four example stars are used to demonstrate the nature of each step in the process of distorting the apparent loci of receivers about a reference orbit and mapping the distortions' effects to the image plane. The elliptical aperture solution from chapter 5 is expanded to likewise include these distortions to a filled aperture. This solution is incorporated as the reference map, $\mathbf{I_o}(\xi, \eta)_\star$, in the metrics of chapter 4 and several example formations are optimized using the techniques of chapter 6. The optimized formations included there and in Appendix F

illustrate the aggregate error approaching zero for formations with increasing numbers of receivers. The remaining appendices describe known solutions for formation dynamics and interferometer performance all adapted to the standardized notation of this research.

II. Satellite Formation Dynamics

Describing the dynamics of a satellite formation relative to a localized frame is a surprisingly difficult problem. The models used to describe the motion of formation elements determine both the available degrees of freedom for choosing their configurations and the relative loci that receivers trace out over time. This chapter begins with the earliest treatment of this problem by Clohessy and Wiltshire, as expanded by Hill, and improved by Schaub and Alfriend to reveal the constraints on element paths. The final section describes the latest modelling improvements by Wiesel that vastly improve the fidelity of element propagation, but still exhibit the four degree of freedom limitation of earlier models.

2.1 Clohessy-Wiltshire Dynamics

The dynamics of satellite formations in a local coordinate system had its first useful treatment by W. H. Clohessy and R. S. Wiltshire [5] back in 1960, as they sought a simple solution to be used for short time-frame orbital rendezvous. Clohessy and Wiltshire simplified the problem by linearizing the orbital dynamics about an unperturbed circular orbit. This circular orbit provided the origin for a local coordinate system, with axes directed along the radial, velocity[1], and orbit plane orthogonal directions. The first-order linearization of the orbital dynamics in this reference frame yields a constant coefficient system. The resulting solution, see Appendix A,

$$\begin{aligned} \ddot{x} &= 2\omega\dot{y} + 3\omega^2 x \\ \ddot{y} &= -2\omega\dot{x} \\ \ddot{z} &= -\omega^2 z \end{aligned} \tag{2.1}$$

hereafter referred to as the C-W solution, has provided at least the initial setup for most investigations into formation dynamics and control.

The basic C-W solution is an adequate model for short-term applications (hours), and has been used for rendezvous studies. Guelman and Aleshin [12] used the basic linear

[1]The original paper by Clohessy and Wiltshire actually chose the *anti*velocity, radial, and orbit normal directions for the local coordinate system. The more conventional choice of radial, velocity, and orbit normal directions is used throughout this work.

dynamics to generate rendezvous maneuvers that minimized fuel usage with arbitrary constraints on thrust. Unfortunately, since the linearized solution does not incorporate even the $J_{2\oplus}$ perturbation, it lacks sufficient fidelity for long term control law synthesis. The higher order effects not modelled by the C-W solution incite unacceptably high control usage and reduce satellite life spans to impractical durations.

Schaub and Alfriend [37] extended the C-W solution to include *first* order oblateness effects (effects of order $J_{2\oplus}^2$ or higher are ignored). Their solution described the relative orbits in terms of the Delaunay orbital elements [50] (l, g, h, L, G, H), where l is the mean anomaly, g is the argument of perigee, h is the right ascension of the ascending node, and $(L,\ G,\ H)$ are the associated generalized momenta. Since the first order $J_{2\oplus}$ effects are not a function of the mean orbital elements (l, g, h), these are unconstrained. It is not possible to eliminate the drift rates of each orbit element, so Schaub and Alfriend sought in their formulation to keep the differences in mean orbit element growths to zero, thus eliminating relative secular growth. However eliminating relative secular rates places two constraints on the choices of $(\dot{l}, \dot{g}, \dot{h})$. Choosing any of the first three orbital elements and any one of the momenta completely determines the other two momenta. This creates a four degree of freedom system rather than six for each formation element. Eliminating *all* of the drift rates actually places a third constraint on the momenta, completely determining the formation from the angular elements and severely limits the choices for formation design.

The orbital period constraints on each element are more readily seen in Hill's parameterization [14] of the C-W solution. Appendix B summarizes the description of formation orbits in terms of six constants (a_H, b_H, ρ_H, m_H, n_H, and θ_H,), of which a_H must be 0 for each element to eliminate secular growth in its path. The parameter b_H is simply an offset of the entire formation along the velocity vector direction, $\hat{e}_y$. Since introducing a constant offset in the $\hat{e}_y$ direction adds nothing to interferometry performance, without loss of generality this parameter is assumed 0 for each element. Again, this yields four

degrees of freedom per formation element.

$$\begin{aligned} x(t) &= \rho_H \sin(\omega t + \theta_H) + a_H \\ y(t) &= 2\rho_H \cos(\omega t + \theta_H) - \tfrac{3\omega}{2} a_H t + b_H \\ z(t) &= m_H \rho_H \sin(\omega t + \theta_H) + n_H 2\rho_H \cos(\omega t + \theta_H) \end{aligned} \tag{2.2}$$

Yeh and Sparks [56] analyzed Hill's equations to develop geometries of free-flying satellite formations without the use of controls. Control-free formations limited their design degrees of freedom to four per satellite, in agreement with the initial formulations of Schaub and Alfriend. Inspection of equation 2.2 reveals that each element in the formation traces out an elliptical path with a 2:1 ratio of major to minor axes.

A variety of optimal control schemes have been developed using the limited fidelity solutions discussed above. Yeh, Nelson, and Sparks [55] developed a methodology for generating control laws using a sliding mode framework. Their work, based on the basic C-W solution, incorporated $J_{2\oplus}$ effects by increasing the controller bandwidth. The thesis by Irvin [15] investigated minimum fuel reconfiguration techniques using the C-W solution and a variety of feedback design techniques (linear, LQR, SDRE, sliding mode). He found that formation reconfiguration could be accomplished for minimal fuel usage using the simplest of linear techniques. Chichka [4] modelled satellite formations to remain in a constant apparent distribution *as viewed from the planet surface*, not an inertial or co-orbiting reference. His selection of formation geometry was strongly driven by viewing angles from a surface location, but did demonstrate the feasibility of creating the formations. DeCou [9] used the basic C-W solution to develop a station-keeping strategy for three satellites forced to remain in the $(\vec{u}\ \vec{v})$ plane (see Section 3.2 for a description of the $(\vec{u}\ \vec{v})$ plane). This plane was to be oriented at an arbitrary angle to the orbital plane, specifically for performing interferometry. The scheme assumed a constant thrust (via ion engines) available for the control system's use, and sought to minimize propellant usage.

Sedwick, Miller, and Kong [40] used the dimensional equation techniques of Buckingham [3] to include more perturbation effects into Hill's equations. The dimensional equations cite that a system with σ characteristics of interest with dimensionality η, should be describable by $\sigma - \eta$ dimensionless parameters. Looking only at planar arrays, this pro-

duced two descriptive constants (similar to the four degrees of freedom from Appendix B, if $m_H = n_H = 0$). They found that first order $J_{2\oplus}$ effects were far stronger than any other perturbations, even out past geosynchronous altitudes. The differential $J_{2\oplus}$ effects were comparable with solar radiation pressure, and the two effects dominated the perturbations of a .5 km diameter cluster at the TechSat 21 altitude of 800 km. Most of the errors from the linearizations in Hill's equations were found to be periodic in nature, with an amplitude of about one sixth of the differential $J_{2\oplus}$ effects. Kong, Miller and Sedwick [22] went on to use these enhanced modelling equations to analyze minimum propellant configurations for optical interferometry formations imaging the Earth from geosynchronous altitudes.

Sabol, Burns, and McLaughlin [36] used the enhanced Draper Semi-analytic Satellite Theory (DSST) to propagate averaged equations of motion for a formation in the presence of a 21st order gravitational field, lunar and solar third body, atmospheric drag, and solar wind perturbations. Their work cataloged the basic geometries of symmetric formations, from the simplest in-plane formation to projected circular orbits, all with an eye towards required propellant usage for formation station keeping.

2.2 Wiesel-Floquet Dynamics

The fidelity of modelling formation dynamics was advanced by more than three orders of magnitude by the work of Wiesel [54]. Wiesel recognized that the elements of a formation follow periodic paths about the local origin, and though the locations change over time, they are bounded (assuming no secular growth). He devised a method for translating an inertial frame Hamiltonian to the same reference frame used by Clohessy, Wiltshire, and Hill. Keeping the Hamiltonian terms out to second order yields a matrix linear system of the familiar form $\dot{\Phi}(t,0) = \mathbf{A(t)}\Phi(t,0)$. Using the techniques of Floquet [25, 29], the state transition matrix may be factored and solved, see Appendix C.

$$\Phi(t,0) = \mathbf{F(t)}e^{\mathbf{J}t}\mathbf{F(0)}^{-1} \tag{2.3}$$

The result is a very high fidelity propagation algorithm that includes potentially *all* of the zonal harmonics and any other conservative and non-conservative perturbations whose

potential functions may be added into the Hamiltonian.

$$\mathcal{X}(t) = \mathbf{F}(t)e^{\mathbf{J}t}\mathbf{F}(0)^{-1}\mathcal{X}(0) \tag{2.4}$$

The thesis by Bordner [1] used this technique to generate extremely accurate estimates of satellite positions in a formation. Bordner implemented Wiesel's solution in a Bayes filter estimation algorithm using noise-corrupted GPS measurement data, carrier-phase differential GPS data, and inter-satellite measurement data.

Wiesel further investigated including second order 2-body terms and zonal perturbations in the Floquet solution [52]. He found that sectoral and tesseral harmonics only perturb the *periodic* orbit, leaving the relative motion unaffected. The second order 2-body and zonal terms do modify the $\mathbf{F}(t)$ matrix, but do not introduce instabilities into the relative motion dynamics. This formulation also introduced a change of variables to a set of six modal variables $\mathcal{Z}$, see section C.3. The physical interpretation of these modal variables is more intuitive than the raw $\mathcal{X}$(t) vector from the first formulation [54], and yields a dynamics description in the familiar linear, constant coefficient form

$$\frac{d}{dt}\mathcal{Z} = \mathbf{J}\mathcal{Z}. \tag{2.5}$$

The solution further reveals two constraints, requiring two of the modal variables to be 0 to prevent secular growth in the relative satellite paths (yielding the four degrees of freedom cited by Schaub and Alfriend). In a third advancement [51], Wiesel used his higher fidelity modelling to determine a theoretically feasible long-term control usage level for station-keeping within the cluster. The level of required control usage falls easily within the capabilities of current proposed spacecraft designs.

2.3 Summary

The models available for describing relative satellite motion from the simple Clohessy-Wiltshire solution to the Wiesel-Floquet dynamics vary greatly in sophistication and fidelity. Each, however, reveals a maximum of four degrees of freedom in choosing the

configuration of a satellite formation. Adding an arbitrary assumption of *planar* formations reduces this to two since the assumption imposes two more constraints.

III. Interferometry Basics

Optimizing a satellite cluster for the specific mission of interferometry requires a more than cursory knowledge of the science and techniques of imaging at radio wavelengths via distributed receivers. This chapter begins with the earliest construction by Michelson of a one-dimensional optical interferometer, then expands the description to incorporate multiple receivers. Modelling the aggregate performance of multiple receivers demonstrates how the target's intensity map is imbedded within a two-dimensional Fourier transform of the image. The necessary frequency and density of measurements of this transformed image (spatial frequency measurements) are described to yield insight into nature of "important" and "redundant" baselines, and the spatial frequencies they measure.

3.1 Michelson Interferometry

The use of interferometric techniques date back to the work of Albert Michelson[1] who applied them to determine the diameter of some of the nearer and brighter stars (Arcturus and Betelgeuse). The basic interferometer combines two samples of incident radiation from a distant source into one receiver. The image plane of an optical telescope forms a rudimentary correlator. In figure 3.1, incident light a_1 and b_1 travel equal distances to the receiver. Light a_2 and b_2, approaching at an incident angle θ, travel paths that differ by a distance, $\Delta = D \sin\theta$, and are therefore out of phase, Ψ, by

$$\Psi = \left(\frac{2\pi}{\lambda_o}\right) D \sin\theta \approx \left(\frac{2\pi}{\lambda_o}\right) D\theta \tag{3.1}$$

The composite image from the two signals displays light and dark patterns due to interference. Michelson proposed that the quality of these fringes could be quantified by the fringe visibility function, V_{fringe}, in terms of the intensity of the light and dark bands, $I_{\max}$ and $I_{\min}$,

$$V_{\text{fringe}} = \frac{I_{\max} - I_{\min}}{I_{\max} + I_{\min}}. \tag{3.2}$$

[1]This is the same Michelson interferometer later used for the first accurate measurement of the speed of light in 1879, and in the famous Michelson-Morley experiment that ended ether-based theory, eventually leading to Einstein's relativity theory.

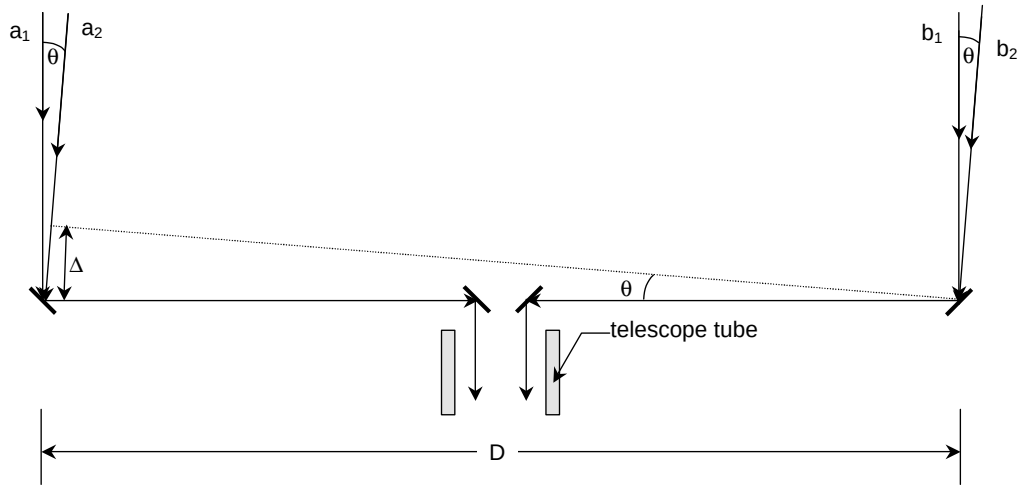

Figure 3.1 The basic Michelson Interferometer combines reflected radiation from two mirrors into a single receiver. The constructive and destructive interference generates a fringe pattern, a simple function of the angle θ and the baseline distance, D (or when measured in wavelengths, D_λ [46]).

The period of these fringes is a direct measure of the small angle θ and the wavelength of the radiation. This rudimentary interferometer can measure the small angle θ by varying the interferometer baseline, D. As the baseline is transformed into different domains, it is nearly always expressed as a unitless number of wavelengths, therefore λ_o is converted to a subscript on the baseline, or $D_\lambda = \frac{D}{\lambda_o}$.

If the width of the star is small compared to θ, the entire image is covered with light and dark bands. The dark bands arise as the phase difference becomes π.

$$\begin{aligned} \pi &= \left(\tfrac{2\pi}{\lambda_o}\right) D\theta \\ \theta &= \tfrac{\lambda_o}{2D} \end{aligned} \tag{3.3}$$

For stars comparable in width to the spacing between maxima, the image can be thought of as resulting from a continuous series of points across the stellar disk. The maxima and minima from different points do not coincide, and the images blend into a smooth continuum. Two interfered images of a circular source have a V_{fringe} determined [13] by a

first order Bessel function.

$$V_{\text{fringe}} = 2\left|\frac{J_1\left(\frac{D\pi\theta}{\lambda_o}\right)}{\frac{D\pi\theta}{\lambda_o}}\right| \tag{3.4}$$

By tuning the interferometer until the image is a single maxima with no fringes, $V_{\text{fringe}} = 0$, the image is termed "resolved."[2] The first order Bessel function has its first $J_1 = 0$ at $\frac{D\pi\theta}{\lambda_o} = 3.83$. Therefore a resolved image first occurs when the baseline is sufficiently long to satisfy

$$\theta = 1.22\frac{\lambda_o}{D}. \tag{3.5}$$

The interferometer may be used to resolve smaller sources by increasing D (therefore the phase difference for smaller θ) or using shorter wavelengths, λ_o.

3.2 Multi-receiver Interferometers

Modern interferometers include far more than two separated receivers, often on moveable supports. The Very Large Array (VLA) on the Plains of St. Agustin, west of Socorro, New Mexico, has 27 individual receivers, each capable of limited repositioning.

Figure 3.2 The Very Large Array (left) near Socorro, New Mexico has its 27 antennas mounted on rails for limited repositioning capability to 72 different antenna stations. The Nobeyama Solar Radio Observatory (right) in Nobeyama, Japan has its 84 antennas permanently spaced for optimum observations of the solar disk.

[2]Betelgeuse, the first star resolved by Michelson's interferometer is a known distance away. Using the measured θ, its diameter was calculated to be roughly 280 times that of our Sun.

3.2.1 Coherence, Correlation, and the van Cittert-Zernike Theorem. The simple Michelson interferometer was adequate for determining a one-dimensional measurement: diameter of the source. It is not, however, sophisticated enough to yield an image equivalent to that obtained by an instrument with a single large aperture. The technique for doing so requires multiple measurements of interfered signals, measurements of the signals' coherence.

To see how these coherence measurements arise, begin by defining the generic coherence, Γ, of a monochromatic waveform, of field strength U, received at two points P_1 and P_2 at times differing by τ by

$$\begin{aligned} \Gamma(P_1, P_2, \tau) &= \lim_{T\to\infty} \frac{1}{2T} \int_{-T}^{T} U(P_1, t) U^*(P_2, t+\tau) dt & \text{(3.6a)} \\ &= \langle U(P_1, t), U(P_2, t+\tau) \rangle. & \text{(3.6b)} \end{aligned}$$

The intensity of the waveform is just its self coherence at any point, $I(P) = \Gamma(P, P, 0)$, or the square of the field strength [13] $I(P) = |U(P)|^2$. Since the generic wave function for a wave propagating in the $\vec{z}$ direction is $U(P,t) = Ue^{i(\frac{2\pi}{\lambda} z - \omega t)}$, the coherence function at P_1 and P_2 may be determined by direct calculation as

$$\begin{aligned} \Gamma(P_1, P_2, \tau) &= \lim_{T\to\infty} \frac{1}{2T} \int_{-T}^{T} Ue^{i\left[\frac{2\pi z_1}{\lambda} - \omega t\right]} Ue^{-i\left[\frac{2\pi z_2}{\lambda} - \omega(t+\tau)\right]} dt \\ &= \lim_{T\to\infty} \frac{U^2}{2T} \int_{-T}^{T} e^{i\left[\frac{2\pi}{\lambda}(z_1 - z_2) - \omega t + \omega t + \omega\tau\right]} dt \\ \Gamma(P_1, P_2, \tau) &= |U|^2 e^{i\left[\frac{2\pi}{\lambda}(z_1 - z_2) + \omega\tau\right]}. \end{aligned}$$

Now consider two incoherent point sources, both being received at P_1 and P_2, as in figure 3.3. By the superposition principle, the received field strength at each point is simply $U = U_a + U_b$. Since the discrete point sources are not strictly on $\vec{s}$, these functions no longer propagate strictly along $\vec{z}$. The component of propagation may be calculated by the inner product of the look vectors from each receiver, $\vec{s}_a$ and $\vec{s}_b$, and their location

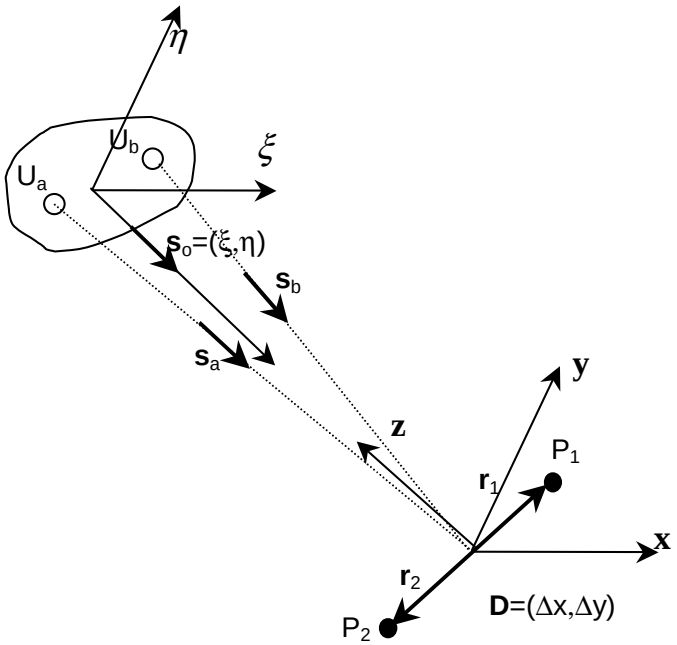

Figure 3.3 Adapted from Rohlfs, since the field strengths of two *incoherent* sources are uncorrelated. Even when measured at the same point, their coherence function is 0.

vectors, $\vec{r}_1$ and $\vec{r}_2$. Dropping the phase offset, their wave functions become

$$\begin{aligned} U_a &= U_a e^{(\frac{2i\pi}{\lambda})(\vec{s}_a \cdot \vec{r})} \\ U_b &= U_b e^{(\frac{2i\pi}{\lambda})(\vec{s}_b \cdot \vec{r})}. \end{aligned} \tag{3.8}$$

Their coherence function is almost as simple.

$$\begin{aligned} \langle U(P_1,t_1)U^*(P_2,t_2)\rangle &= \langle [U_a(P_1,t_1)+U_b(P_1,t_1)],[U_a(P_2,t_2)+U_b(P_2,t_2)]\rangle \\ &= \langle U_a(P_1,t_1),U_a(P_2,t_2)\rangle + \langle U_a(P_1,t_1),U_b(P_2,t_2)\rangle + \\ &\quad \langle U_b(P_1,t_1),U_a(P_2,t_2)\rangle + \langle U_b(P_1,t_1),U_b(P_2,t_2)\rangle \end{aligned}$$

Since the sources are incoherent, the field strengths U_a and U_b are uncorrelated, so the cross terms are zero and

$$\begin{aligned} \Gamma(P_1,P_2) &= \langle U_a(P_1,t_1),U_a(P_2,t_2)\rangle + \langle U_b(P_1,t_1),U_b(P_2,t_2)\rangle \\ &= |U_a|^2 e^{\left(\frac{2i\pi}{\lambda}(\vec{s}_a\cdot(\vec{r}_1-\vec{r}_2))\right)} + |U_b|^2 e^{\left(\frac{2i\pi}{\lambda}(\vec{s}_b\cdot(\vec{r}_1-\vec{r}_2))\right)}. \end{aligned}$$

Extending this to M sources, the coherence function is simply a function of the distance between the receivers, $\mathbf{D} = \vec{r}_1 - \vec{r}_2$.

$$\Gamma(\mathbf{D}) = \sum_{n=1}^{M} |U_n(\vec{s})|^2 e^{\left(\frac{2i\pi}{\lambda}(\vec{s}_n \cdot \mathbf{D})\right)}$$

In the limit as $M \to \infty$, simply integrate across the entire area of the source (the source goes to zero outside a small angle, so the limits may be set to $\pm\infty$ without loss of generality)

$$\Gamma(\mathbf{D}) = \int_{-\infty}^{\infty}\int_{-\infty}^{\infty} |U(\vec{s})|^2 e^{\left(\frac{2i\pi}{\lambda}(\vec{s}\cdot\mathbf{D})\right)} d\Omega \tag{3.12}$$

where, $U(\vec{s})$ is the field strength per solid angle (steradian). Note that $|U(\vec{s})|^2$ is just the intensity of the source at each point $\vec{s} = (\xi, \eta)$, so $|U(\vec{s})|^2 = \mathbf{I}(\xi, \eta)$. The dot product $\vec{s} \cdot \mathbf{D}$ may be simplified as well. Since it is a scalar value derived from vectors whose components are expressed in different coordinate systems, its value is not affected by the unitary matrix necessary to rotate from one to the other. Therefore it may be written simply as $\vec{s} \cdot \mathbf{D} = |\vec{s}||\mathbf{D}| \cos(\angle \vec{s}\mathbf{D}) = \Delta x \xi + \Delta y \eta$.

$$\Gamma(\mathbf{D}) = \int_{-\infty}^{\infty}\int_{-\infty}^{\infty} \mathbf{I}(\xi, \eta) e^{\left(\frac{2i\pi}{\lambda}(\Delta x\xi + \Delta y\eta)\right)} d\xi d\eta. \tag{3.13}$$

This is the monochromatic version of the van Cittert-Zernike Theorem. It shows how the coherence function for a monochromatic wave field that is built up from plane waves is related to the intensity map [35]. This intensity map[3], $\mathbf{I}(\xi, \eta)$, is the desired image. It may be solved for if $\Gamma(\mathbf{D})$ can be measured over a sufficiently diverse set of $\mathbf{D}$. Measuring interfered signals gives just such a set of coherence function measurements.

3.2.2 Synthesizing an Aperture. Terrestrial interferometry arrays synthesize a large aperture telescope using a large array of discrete receivers. The signals from multiple pairs of receivers are sent to a correlator (a device that multiplies and time-averages the incoming signals). The correlator's response is not quite a direct measure of $\Gamma(\mathbf{D})$ since

[3]Texts on interferometry refer to the structure of an image over the viewing angles (ξ, η) as either the intensity, $\mathbf{I}(\xi, \eta)$, or the brightness, $\mathbf{B}(\xi, \eta)$. By Rohlfs [35], the two terms are interchangeable, but "intensity" is the preferred term here.

antenna beam patterns are not perfect and cannot discriminate discrete points (ξ, η) in the source.

Consider the delay time, τ, for an inbound signal as received by a pair of receivers, figure 3.4, from a differential area of the source, $\mathbf{I}(\xi, \eta)$. From Rohlfs [35], the differential

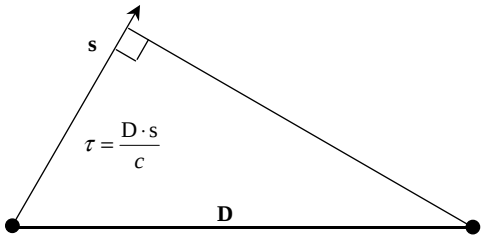

Figure 3.4 The delay time, τ, between receivers receiving signals from $\vec{s}$ is a simple function of the baseline dot product with $\vec{s}$.

receiver response, d$\mathbf{R}$, due to this delay is

$$d\mathbf{R}(\mathbf{D}) = \mathbf{A}_N(\xi, \eta)\mathbf{I}(\xi, \eta)e^{2i\pi\nu\tau}d\xi d\eta, \tag{3.14}$$

where $\mathbf{A}_N(\xi, \eta)$ is the normalized antenna beam pattern specific to the type of receiver and antenna employed. (If antennas with infinite apertures were available, $\mathbf{A}_N(\xi, \eta) = 1$, and it would be possible to directly measure $\Gamma(\mathbf{D})$.) Integrating this response over the source yields

$$\mathbf{R}(\mathbf{D}) = \int_{-\infty}^{\infty}\int_{-\infty}^{\infty} \mathbf{A}_N(\xi, \eta)\mathbf{I}(\xi, \eta)e^{\left(2i\pi\nu\frac{D\cdot\vec{s}}{c}\right)}d\xi d\eta \tag{3.15a}$$

$$= \int_{-\infty}^{\infty}\int_{-\infty}^{\infty} \mathbf{A}_N(\xi, \eta)\mathbf{I}(\xi, \eta)e^{\left(\frac{2i\pi}{\lambda}(\Delta x\xi + \Delta y\eta)\right)}d\xi d\eta. \tag{3.15b}$$

In actual systems, well made antennas have $\mathbf{A}_N(\xi, \eta)$ going to essentially zero outside of a very narrow beam, so the integration limits may be safely set to infinity. Note that this is not quite the coherence function of equation 3.13, but it is close. It differs only by the factor $\mathbf{A}_N(\xi, \eta)$, a known function of the antenna.

With sufficiently extensive measurements of $\mathbf{R}(\mathbf{D})$ over large variations in $\mathbf{D}$, a function mapping $\Gamma(\mathbf{D})$ may be synthesized with high fidelity. Further, the inverse transform

of equation 3.13 yields the high resolution image, $\mathbf{I}(\xi, \eta)$, that a single large aperture would have given.

In practice, the process of obtaining an image involves taking the Fourier transform of the interferometer's coherence measurements at *all* available spatial frequencies, determined by the geometry and spacing of the receiver elements. As the correlator records these interfered waveforms of the same wavefront received at various separations, it yields spatial frequency measurements. Different measurements can then be gathered by changing the baseline separation between the receivers. For arrays on the ground, the Earth's rotation provides these changes by moving the entire array, rotating the receiving pairs through a predictable locus of viewing geometries.

The $\frac{1}{\lambda}$ factor in equation 3.15 suggests the convention of defining receiver locations at any time in terms of dimensionless numbers of wavelengths rather than units of length, figure 3.5. Appendix D summarizes how this local coordinate system may also be in-

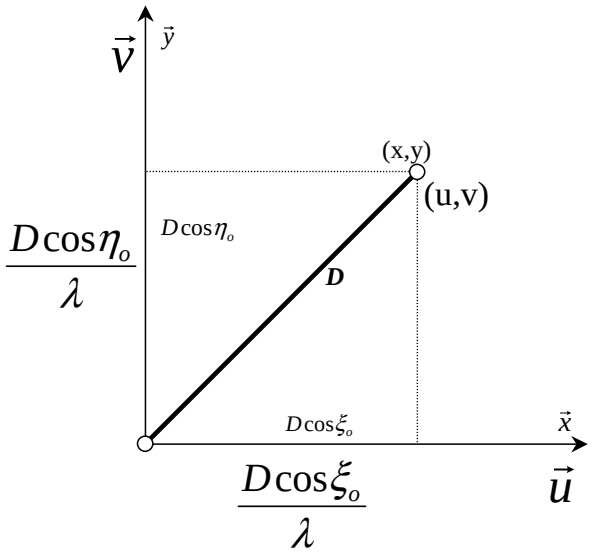

Figure 3.5 Applying the factor $\frac{1}{\lambda}$ to both x and y coordinates defines a reference frame in terms of dimensionless numbers of wavelengths. Its coordinates, (u, v), are defined by the target center (ξ_o, η_o), and are the antenna spacing components orthogonal to the viewing direction.

terpreted as components of spatial frequency [46]. For a source located at some angles (ξ, η) from the array normal, figure 3.5 define the values $u = \frac{D\cos\xi_o}{\lambda_o}$ and $v = \frac{D\cos\eta_o}{\lambda_o}$ as

the components of antenna spacing orthogonal to the view direction (the $\vec{w}$ axis). The aperture plane, or $(\vec{u}\ \vec{v})$ plane, is just the Fourier transform of the image plane over its viewing angle variables (ξ, η). The baseline distance, D_λ from figure 3.1, between receivers in the $(\vec{u}\ \vec{v}\ \vec{w})$ reference system has components (u, v, w), all in dimensionless numbers of wavelengths. Figure 3.6 shows this basic geometry of a two-receiver array, imaging a distributed source, S.

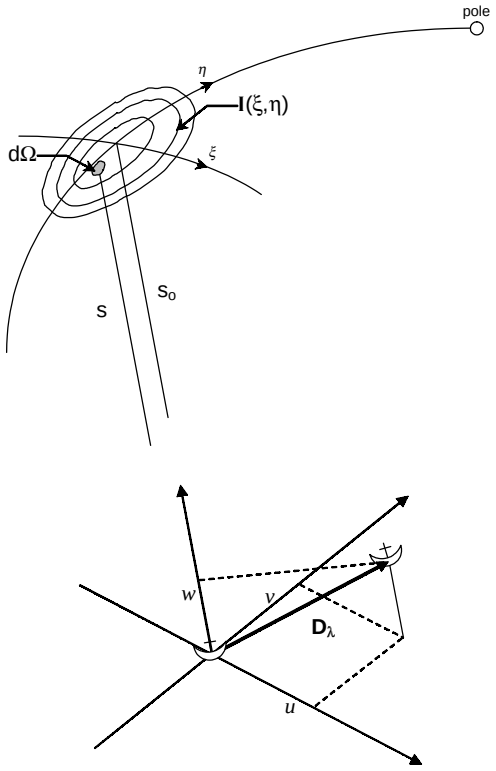

Figure 3.6 The spatial frequency coordinate system used to describe a multiple receiver interferometer is the $(\vec{u}\ \vec{v}\ \vec{w})$ frame. The frame's orientation directs the $\vec{w}$ axis toward the source, S, and arrays the receivers about in the $(\vec{u}\ \vec{v})$ plane. The receiver locations determine spatial frequency measurements.

Most research on interferometry construction focuses on receiver motion within the $(\vec{u}\ \vec{v})$ plane since this directly determines which spatial frequency measurements will be recorded by the array. To appreciate the spacing loci required to image a source, consider the use of a two-dimensional discrete Fourier transform to image an object of size $(\Delta\xi, \Delta\eta)$. To reconstruct such an image, measurements are required on a rectangular grid [27, 46] with spacing no greater than $\Delta u = \frac{1}{\Delta\xi}$ and $\Delta v = \frac{1}{\Delta\eta}$. Unless receivers have exactly

measured the coherence function at each of these locations (never the case), the values must be interpolated from measurements obtained as the receivers swept through some locus in the plane (see figure 3.7). Therefore, it is obviously desirable to fill the $(\vec{u}\ \vec{v})$ plane

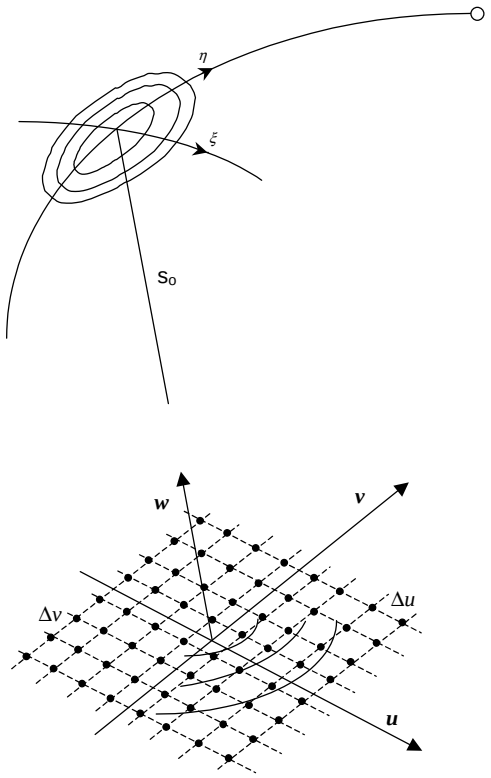

Figure 3.7 To image a source of size $(\Delta\xi, \Delta\eta)$ at a bandwidth of $\Delta\lambda$ centered at λ_o, measurements in the $(\vec{u}\ \vec{v})$ plane are required at spacing no larger than $\Delta u = \frac{\Delta\lambda}{\lambda_o}\frac{1}{\Delta\xi}$ and $\Delta v = \frac{\Delta\lambda}{\lambda_o}\frac{1}{\Delta\eta}$.

as densely as possible with measurements. Increasing the size of the $(\vec{u}\ \vec{v})$ plane allows larger sources to be imaged, or smaller sources to be imaged with greater resolution.

For optical wavelength instruments, most practical arrays rigorously control their receivers to physically remain within the $(\vec{u}\ \vec{v})$ plane, since removing $\vec{w}$ components from the coherence measurement requires knowledge of the signal's phase. Location tolerances for radio frequencies are more relaxed since it is possible to accurately measure the phase of longer wavelengths. This is currently not possible for the short wavelengths of visible light.

The quality and distribution of each measurement taken in the $(\vec{u}\ \vec{v})$ plane may be more completely specified by defining the spatial frequency analog of the intensity map. From Thompson [46], rewrite the response function of equation 3.15 in terms of variables (ξ', η') for integration about each set of viewing angles (ξ, η).

$$\mathbf{R}(\xi,\eta) = \int_{-\infty}^{\infty}\int_{-\infty}^{\infty} \cos\left[2\pi D_\lambda \cos\theta\right] \mathbf{A}(\xi-\xi',\eta-\eta')\mathbf{I}(\xi',\eta')d\xi' d\eta' \tag{3.16}$$

This allows the response function or measurement to be expressed as a more general visibility function of the spatial frequency variables, $\mathcal{V}(u,v,w)$ by the general two dimensional Fourier transform[4]

$$\mathcal{V}(u,v,w) = \int_{-\infty}^{\infty}\int_{-\infty}^{\infty} \mathbf{A}_N(\xi,\eta)\mathbf{I}(\xi,\eta) e^{-2i\pi\left[u\xi+v\eta+w\left(\sqrt{1-\xi^2-\eta^2}-1\right)\right]} \frac{d\xi d\eta}{\sqrt{1-\xi^2-\eta^2}}. \tag{3.17}$$

This function is truly a measure of how visible each spatial frequency measurement is. If the viewed source ($\Delta\xi$ and $\Delta\eta$) is small enough, then $\left(\sqrt{1-\xi^2-\eta^2}-1\right) w \approx -\frac{1}{2}\left(\xi^2+\eta^2\right) w$ and the visibility function is simplified in the $(\vec{u}\ \vec{v})$ plane [6] to $\mathcal{V}(u,v)$ by

$$\mathcal{V}(u,v) = \int_{-\infty}^{\infty}\int_{-\infty}^{\infty} \mathbf{A}_N(\xi,\eta)\mathbf{I}(\xi,\eta) e^{-2i\pi(u\xi+v\eta)} \frac{d\xi d\eta}{\sqrt{1-\xi^2-\eta^2}}. \tag{3.18}$$

The entire mathematical relationship between $\mathcal{V}(u,v)$, $\mathbf{I}(\xi,\eta)$, the received power, and the spectral sensitivity are summarized in figure 3.8[5]. Note how in the $(\vec{u}\ \vec{v})$ domain, the spectral sensitivity, $\mathcal{W}(u,v)$, is just the transfer function of linear system. In control theory, a linear system's transfer function is the transform of the response of a system to a temporal delta function (which transforms to a uniform input across all frequencies). An interferometer's transfer function is the two-dimensional transform of the system's response

[4] Rohlfs [35], who actually cites Thompson frequently in her work, defines the transformation from the $(\vec{\xi}, \vec{\eta})$ domain to the $(\vec{u}\ \vec{v})$ domain with an $e^{2i\pi}$ and the *inverse* transformation with $e^{-2i\pi}$. Either convention will work, provided it is applied consistently. This work adopts Thompson's convention.

[5] Though this figure is directly from Thompson, it displays a minor inconsistency. Equation 3.18, also from Thompson, obviously includes the effects of the antenna beam patterns in what is labelled the "Visibility Function." Equation 3.18 apparently describes the Fourier transform of the "Output Map," or the "*Measured* Visibility."

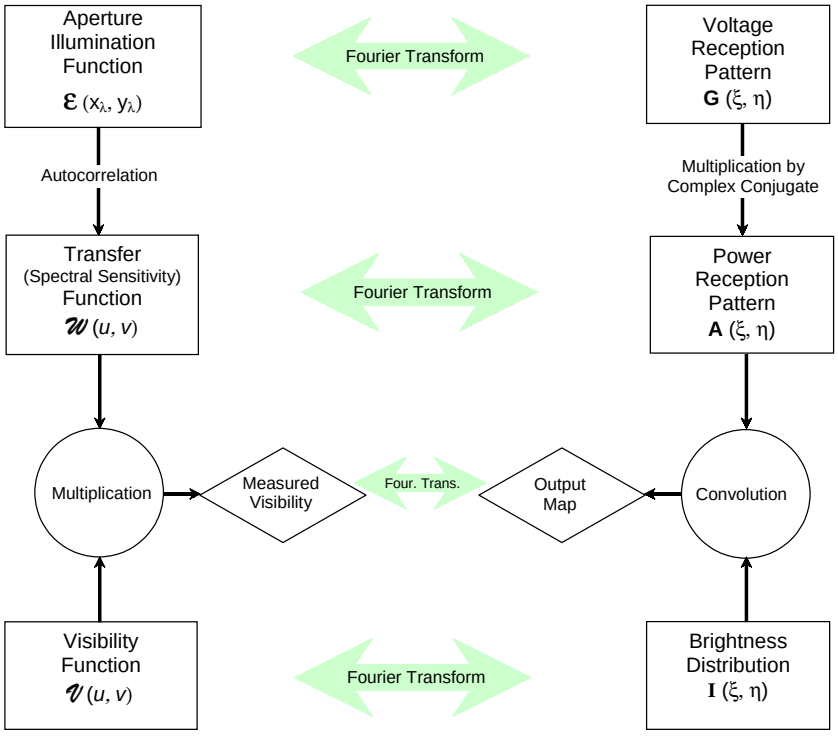

Figure 3.8 From Thompson [46], the Spectral Sensitivity, Visibility Function, Power Reception Pattern, and Brightness Distribution are all related by Fourier transformations.

to a two-dimensional delta function in the spatial domain (which transforms to a uniform input across all spatial frequencies). A true point source would generate a perfect wave front, and thus be mapped to a uniform input at any spatial frequency. The frequency domain for the interferometer transfer function is one of spatial frequency ($\frac{\text{cycles}}{\text{radian}}$). The $\mathcal{W}(u, v)$ is a direct description of how sensitive the system actually is to these frequencies, hence its other name, "spectral sensitivity."

The terms "high" and "low" spatial frequencies may seem unfamiliar. Their contributions to the final image quality are readily illustrated by qualitatively separating each in the construction of an example image, figure 3.9[6]. By themselves, the low spatial frequencies build the relatively poor image resembling that offered by a small aperture system. The high spatial frequencies refine the small details (rapid changes in the spatial domain,

[6]This series of images was created using the Filter Design and Analysis Toolbox tool in MatLab's Signal Processing Toolbox 5.0.

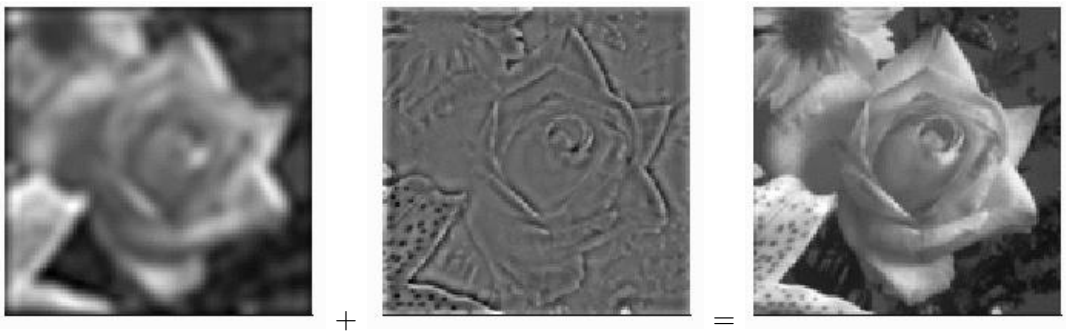

Figure 3.9 The overall image quality is a composite of the regional intensities offered by low spatial frequencies and the edge-defining properties of the high spatial frequencies.

often called "edge detection") but are insufficient by themselves to build the complete image.

Historically, the layout of terrestrial based interferometer arrays sought to optimize high and low spatial frequency measurements and minimize interpolation by sampling $\mathcal{V}(u, v)$ as uniformly as possible, through all available spatial frequencies. Evenly spacing the loci traced out by the receivers in the $(\vec{u}\ \vec{v})$ plane do minimize the interpolation required to map out the coherence function over the plane. Redundant loci and redundant spacings add little to the resolution, and were therefore avoided for computational (and fiscal) frugality. This drove early arrays to seek minimum spacing redundancy. An early

Figure 3.10 This five antenna array suggested by Bracewell only has redundancy in the unit spacing.

paper by Bracewell [2] presented a 1-dimensional spacing scheme for up to 5 receivers in a discretized linear array with minimal redundancy (figure 3.10). More capable arrays added rail systems, allowing the antenna spacing to be varied even more. Using these arrays to image stellar sources entails observation times on the order of 12 hours. Half of one Earth rotation traces out a locus for the receiver pairs that just repeats during any portion of the next half rotation (with the receiver positions reversed).

The "Y" shape of the VLA, figure 3.11, shows some of the linear geometry dictated by the limited railroad hardware, but is also the result of a 0^{th} order optimization study. As

Figure 3.11 The "Y" shape of the VLA was chosen to minimize the number of $(\vec{u}\ \vec{v})$ cells not intersected by a receiver locus over a viewing period.

described by Napier [27], Mather discretized the $(\vec{u}\ \vec{v})$ plane into viewing "cells" and computed the 27 antenna loci over a viewing period of ± 4 hours. The optimization minimized the number of viewing cells not intersected by one of the receiver loci through one viewing period, constrained by the quasi-linear geometry. The 27 antennas yield $\binom{27}{2} = \frac{27!}{2!25!} = 351$ antenna pairs at any time. Each antenna pair provides two measures of fringe visibility, which are complex conjugates of each other, symmetric about the $(\vec{u}\ \vec{v})$ origin.

The 702 points actually constitute an *instantaneous* transfer function, $\mathcal{W}(u, v)$, of the array [45] (the 702 discrete spatial frequency responses to an impulse function, often referred to as the "snapshot" mode of the VLA). These are concentrated along six radial lines resulting from the three linear lines of antennas.

3.3 Summary

The science of interferometry is concerned principally with positioning pairs of receivers to measure received signals over enough spatial frequencies to yield an image resembling a large aperture's rendering of the source. Since the relative receiver locations give measurements that are Fourier transforms of the image frequencies, the techniques naturally address aperture locations in terms of the spatial frequencies measured. From the earliest interferometer that measured a single spatial frequency, the science has grown

to large arrays. Increasing the number of individual receivers in an array rapidly increases the number of measurable baselines at any instant, since receivers' outputs are interfered pairwise. Moving individual receivers or the entire array offers still more spatial frequency measurements.

IV. Satellite-Based Interferometry

This chapter addresses moving interferometry-based receivers to orbital platforms as a logical extension from terrestrial based systems. Orbiting receivers offer both freedom from atmospheric distortion and the potential for extremely long baselines. This promise has prompted much previous work, and has resulted in the basic formulation of simple metrics. These metrics as developed for simple symmetric formations, are disassembled and addressed piece by piece, then generalized to include time variations.

4.1 Previous Proposals and Investigations

Satellite-based interferometry is conventionally divided into the two regimes of optical and radio systems. This division is principally driven by the need for temporal coherence in the received signals. Optical systems typically preserve this coherence by tightly controlling the optical pathways from receivers to correlator forcing them to be identical. For high contrast fringes, this equates to physically controlling pathlengths down to the order of $\frac{\lambda_o^2}{\Delta\lambda}$, where λ_o is the mean design wavelength and $\Delta\lambda$ is the passband for the system [42][1].

The short wavelengths of visible (and infrared) light nearly always require practical designs to incorporate some physical connection between the receivers or mirrors to rigidly control the optical pathlengths [28]. Radio wavelength systems have a more relaxed tolerance on the receivers. Thus the receivers may be physically disconnected, provided that their relative positions can be determined to less than the proscribed pathlength tolerance.

As early as 1983, Preston et al. [33], seeing the capabilities of the newly completed VLA, suggested placing at least one element of a terrestrial array into near-Earth orbit and using Very Long Baseline Interferometry (VLBI) techniques to correlate its signals with those received on the ground. Such an orbiting element would not only greatly increase the array's baseline, but offer improved ($\vec{u}$ $\vec{v}$) coverage of low declination sources, and shorten required viewing times (well below the 12-hour dwell times typical of surface arrays) for short duration targets. The coverage of such a system was nowhere near uniform, and relied

[1] Stachnik and Gezari's actual tolerance is given as $\lambda_o^2\Delta\lambda$, but a quick dimensional analysis shows this to be an apparent typographical error.

heavily on the terrestrial elements to fill in the center of the ($\vec{u}$ $\vec{v}$) plane. One suggested method of reducing the ($\vec{u}$ $\vec{v}$) "holes" was simply adding more orbiting receivers, essentially driving planners to build a constellation (with minimal reconfiguration capability, and some very long wait times, $\sim$20 days).

DeCou [9] used the basic C-W dynamics model to analyze a trio of vehicles (two receivers, one correlator) imaging an arbitrary $\vec{w}$ direction. His development assumed a constant thrust engine and yielded a scheme to gradually fill in the ($\vec{u}$ $\vec{v}$) plane by spiraling the loci outward from an initial starting geometry (an optimistic scheme also suggested by Kibblewhite [19] back in 1984). DeCou's interferometer description was for optical wavelengths, so he accordingly insisted that the receivers be controlled to remain within the ($\vec{u}$ $\vec{v}$) plane (the required fidelity of control was not addressed). He also developed a methodology for repositioning the formation to image a different desired inertial target.

Johnston and Nock [17], from the Jet Propulsion Laboratory, analyzed the requirements for another three vehicle formation, intended to perform optical interferometry. Since the vehicles were not physically connected, much of the work centered on ensuring the equal optical pathlengths between the two telescope vehicles and the single combining station vehicle. Using the basic C-W solution (with origin at the combining station vehicle), it was possible to generate a methodology for selecting a free-flying formation that kept the two pathlengths equal, driven by the location of the target source, the length of the baseline (a modest 10 kilometers, maximum), and the angular velocity of the reference orbit. Like DeCou, maintaining the optical pathlengths was all important, with no metrics devised for image quality.

The notion of flying an optical interferometer was formalized in the Spacecraft Array for Michelson Spatial Interferometry (SAMSI) program [42]. This system architecture consisted of three or two vehicles (by perhaps combining one of the telescopes with the combiner station), figure 4.1. Though not physically connected, the precise receiver location criteria was proposed to be handled by laser-locating each telescope vehicle, and physically contracting/extending the optical pathlength within the combiner vehicle. The physical size of the combiner therefore proved to be a limiting factor on the allowable variance in relative orbit location. Filling in the ($\vec{u}$ $\vec{v}$) plane with adequate samplings of

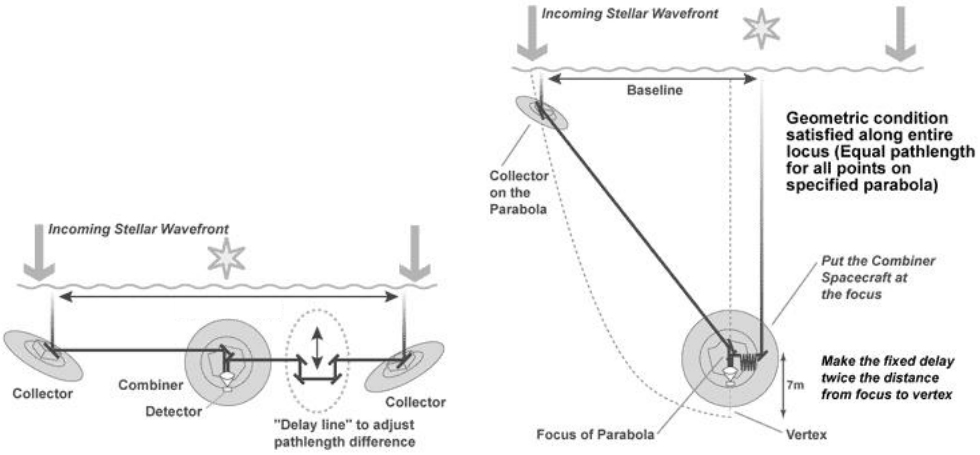

Figure 4.1 The SAMSI program sought to perform optical interferometry via two or three vehicles with a modest baseline. After accurately measuring the receiver position(s), the optical pathlengths could be physically matched aboard the combiner.

$\mathcal{V}(u, v)$ also drove the designers to include ion thrusters to drive the receivers around in an expanding $(\vec{u}\ \vec{v})$ spiral. Sampling criteria for the short wavelengths limit such a spiral to a diameter of roughly 100 meters.

4.2 Formation-Based Interferometry

Employing a satellite formation for performing interferometry missions offers several advantages over a constellation, a pair, or a trio. Since a cluster can more densely populate the $(\vec{u}\ \vec{v})$ plane with receivers, it offers shorter required observation times to yield adequate samplings of the visibility function over the image plane. These samples may cross the complete image plane rather than some locus which excludes the center (constellations cannot have receivers passing through the center of the inertial orbit plane). Formation dynamics also offer low-control use reconfigurations as mentioned in section 2.1. This allows relatively cheap reorientation for optimal geometries to view new targets.

Several recent works have analyzed potential uses for formations capable of receiving and correlating visible or radio signals. Each was faced with the difficult task of defining a metric for a desirable quality in the interferometer.

Mallory et al. [23] analyzed a formation, actually a constellation of geosynchronous orbits, selected to have overlapping ground traces. Since the ground traces of geosynch orbits close on themselves, the orbital paths naturally filled in the $(\vec{u}\ \vec{v})$ plane as mapped onto an orthogonal projection about the constellation's nadir. Their choice of a performance metric was simply a statistical accounting of the number of receiver pairings in a discretized $(\vec{u}\ \vec{v})$ plane covered over time, compared to the total number of possible pairings (similar to Mather's work on optimizing the VLA spacings). Though simple, this metric did acknowledge time dependency.

Sedwick, Kong, and Miller [39] used the basic C-W solution parameterized into Hill's equations, and added in perturbations from atmospheric drag, solar wind, and magnetic forces. Their performance measure of merit was based on the point spread function, **PSF**. This **PSF** was refined and integrated by Sedwick, Hacker, and Miller [38]. Adopting Thompson's notation of ξ and η for image angular coordinates, it may be expressed

$$\mathbf{PSF}(\xi,\eta) = \left[\text{Gain}\,(D_\lambda,\theta)\left|\sum_{k=1}^{N} e^{-(2i\pi(u_k\xi+v_k\eta))}\right|\right]^2, \tag{4.1}$$

where u_k and v_k are locations in the $(\vec{u}\ \vec{v}\ \vec{w})$ reference frame. The **PSF** shows the effects of including or excluding available baselines from the compilation of an image. By discretizing all possible positions of satellites in a plane, Sedwick and Kong created a reference array and performed a point by point comparison of possible formations to this fully filled array. Though image quality was mentioned, the work focused on evaluating synthetic aperture radars for moving target identification (MTI). The integrated, or cumulative distribution of the Probability of Detection, yields the Availability of Detection as a figure of merit. The Availability of Detection offers a measure of the fraction of time that a given MTI performance can be expected. In this use, the statistics' dependence on time was apparent, but was not judged to be critical due to the short duration of MTI missions.

Kong and Miller [20] had earlier developed an instantaneous performance metric of image quality for an array restricted to symmetric (u,v) and $(-u,-v)$ receiver pair locations. They assumed a "stop and stare" mode (a necessary simplification for their work at the time), and applied it to optical sensing. The intensity map of a given source

may be transformed to that received by such a restricted pair by a technique described by Hecht [13]. Hecht begins by convolving a two-dimensional point source at (u, v) with the Point Spread Function.

$$\mathbf{I}(\xi,\eta) = \int_{-\infty}^{\infty}\int_{-\infty}^{\infty} \delta(x'-u)\delta(y'-v)\mathrm{PSF}(x',y',\xi,\eta)dx'dy' \tag{4.2}$$

Kong and Miller used as the **PSF** the two variable Fourier transform from equation 4.1 with a gain specified by the generic directivity, $\mathcal{D}(\theta)$, of an optical system. For a target at off-axis angle θ, this incorporates the fringe visibility function (converting Kong and Miller's original notation with $\frac{D}{\lambda_o} = D_\lambda$) to yield

$$\mathcal{D}(\theta) = \left[\pi(1+\cos\theta)D_\lambda\left(\frac{J_1\left(D_\lambda\pi\sin\theta\right)}{D_\lambda\pi\sin\theta}\right)\right]^2. \tag{4.3}$$

Using this as the **PSF** gain, $\mathbf{I}(\xi,\eta)$ becomes

$$\mathbf{I}(\xi,\eta) = \int_{-\infty}^{\infty}\int_{-\infty}^{\infty} \delta(x'-u)\delta(y'-v)\left[\pi(1+\cos\theta)D_\lambda\left(\frac{J_1\left(D_\lambda\pi\sin\theta\right)}{D_\lambda\pi\sin\theta}\right)\right]^2\left|\sum_{k=1}^{N} e^{-2i\pi(x'_k\xi+y'_k\eta)}\right|^2 dx'dy'. \tag{4.4}$$

This relation may be used to map the symmetric pair assumed by Kong and Miller. Convolving the impulse functions with the receiver locations yields

$$\mathbf{I}(\xi,\eta) = \int_{-\infty}^{\infty}\int_{-\infty}^{\infty} \delta(x'-u)\delta(y'-v)\mathcal{D}\left|e^{-2i\pi(x'\xi+y'\eta)} + e^{-2i\pi(-x'\xi-y'\eta)}\right|^2 dx'dy'. \tag{4.5}$$

By the sifting property of the δ function this is easily seen to be[2]

$$\begin{aligned}
\mathbf{I}(\xi,\eta) &= \mathcal{D}\left|e^{-2i\pi(u\xi+v\eta)} + e^{-2i\pi(-u\xi-v\eta)}\right|^2 \\
&= \mathcal{D}\left|\cos 2\pi(u\xi+v\eta) - i\sin 2\pi(u\xi+v\eta) + \cos 2\pi(u\xi+v\eta) + i\sin 2\pi(u\xi+v\eta)\right|^2 \\
&= \left[\pi(1+\cos\theta)D_\lambda\left(\frac{J_1\left(D_\lambda\pi\sin\theta\right)}{D_\lambda\pi\sin\theta}\right)2\cos 2\pi(u\xi+v\eta)\right]^2.
\end{aligned}$$

[2]Kong and Miller's actual presented expression was $\left[\pi(1+\cos\theta)D_\lambda\left(\frac{J_1(D_\lambda\pi\sin\theta)}{D_\lambda\pi\sin\theta}\right)2\cos\pi(u\xi+v\eta)\right]^2$, but that result is respectfully disputed here.

Using the property of the Bessel function that $\lim_{a\to 0} \frac{J_1(a)}{a} = \frac{1}{2}$ simplifies $\mathbf{I}(\xi,\eta)$. For $\theta = 0$, the condition that occurs when $\vec{w}$ is defined to point directly at the source,

$$\begin{aligned} \mathbf{I}(\xi,\eta) &= \left[\pi(1+1)D_\lambda\left(\frac{1}{2}\right)2\left(\cos 2\pi(u\xi+v\eta)\right)\right]^2 \\ &= \left[2\pi D_\lambda \cos 2\pi(u\xi+v\eta)\right]^2. \end{aligned} \tag{4.7a}$$

The contributions of N symmetrically spaced receiver pairs can be summed up to yield an effective intensity map, $\overline{\mathbf{I}}(\xi,\eta)$, via

$$\overline{\mathbf{I}}(\xi,\eta) = \frac{(2\pi D_\lambda)^2}{N}\left[\sum_{k=1}^{N}\left(\cos 2\pi(u_k\xi+v_k\eta)\right)^2\right]. \tag{4.8}$$

which provides an instantaneous assessment of the received intensity for any location (ξ,η) by all receivers in the formation. This relation was further used to determine an $\mathbf{I_o}(\xi,\eta)$ function that would be generated if receivers occupied *all* symmetric locations (u,v) in a discretized formation plane. This instantaneous measure of the best image obtainable by a discretized formation was analyzed over a discretized $m \times m$-pixel image field to yield the aggregate mean square error.

$$MSE = \frac{\sum_{i=1}^{m}\sum_{j=1}^{m}\left(\overline{\mathbf{I}}(\xi_i,\eta_j) - \overline{\mathbf{I}}_\mathbf{o}(\xi_i,\eta_j)\right)^2}{m\times m} \tag{4.9}$$

Kong and Miller discretized the imaging field into such an $m \times m$ grid and performed a 0^{th} order optimization through a simulated annealing technique [16]. Each iteration of this technique compared combinations of possible receiver pairings to the summation, $\overline{\mathbf{I}}_\mathbf{o}(\xi_i,\eta_j)$, of *all* possible (2601 permutations in their model) symmetric receiver pairings of (u,v) and $(-u,-v)$.

4.3 Analyzing a Comparison Metric

The logic put forward by Kong and Miller of comparing the intensity map from a discrete receiver array to a filled aperture of equal size is almost inarguable. A filled

aperture is essentially an infinite number of receivers. Comparing the discrete receivers' performance to this infinite number basically picks out which receivers' outputs are crucial, and which are redundant. While advancing the logic used in Kong, Miller, and Sedwick's investigation, there are several issues that bear scrutiny. The selection of an appropriate $\mathbf{I_o}(\xi, \eta)$ has several possibilities. The calculation of $\overline{\mathbf{I}}(\xi, \eta)$ is somewhat complex for asymmetrical formations. Furthermore, the size of the image plane over which the comparison is performed has some effect on the calculated optimal configuration and a *huge* effect on the calculation budget necessary to determine that optimum. The metric, its aggregate aperture, and the image plane size are formalized here. The reference apertures are addressed in chapter V.

Performing a comparison of a pair of two-dimensional functions over an area is necessarily a double integration. The aggregate aperture $\overline{\mathbf{I}}(\xi, \eta, t)$ is a function of the receiver locations at any time, and $\mathbf{I_o}(\xi, \eta)$ is determined by the chosen aperture geometry. Employing a second order metric, this becomes

$$\mathbf{J}_{\text{image}}(\text{path}, t) = \int_{\eta_o}^{\eta_f} \int_{\xi_o}^{\xi_f} \left[\overline{\mathbf{I}}(\xi, \eta, t) - \mathbf{I_o}(\xi, \eta)\right]^2 d\xi d\eta. \tag{4.10}$$

Kong, Miller, and Sedwick's report [21] to the TechSat 21 office included an outstanding discussion of optimization techniques based on a metric of comparison with a filled aperture. Kong's thesis (a subsection of their report) developed a filled circular aperture, discretized the image plane into $m \times m$ cells, and performed a point by point comparison, using the metric put forth in his paper with Miller [20], equation 4.9. Minimizing such a metric provides an image with a minimum instantaneous error. Their pioneering work showed the advantages of departing from earlier, geometrically symmetric configurations, to yield minimal errors over appropriate portions of the image plane. They further investigated propellant budgets needed to reconfigure formations to these optimal geometries.

4.3.1 Comparing Apertures. Using the image plane to compare outputs of different apertures is essentially a differencing of two energy fluxes. Each aperture generates an intensity map carrying units of $\frac{\text{watts}}{\text{steradian}}$, and the comparison process requires calculating

the flux generated by each aperture at locations (ξ, η) across the image plane and performing the subtraction $\overline{\mathbf{I}}(\xi, \eta, t) - \mathbf{I_o}(\xi, \eta)$. A well matched pair of apertures yields only slight differences at each location, and the normalized sum in equation 4.9 is just an average of small numbers.

To illustrate the nature of this comparison sum, consider a one-dimensional filled aperture, $\mathbf{I_o}(\xi)$, compared to a discrete aperture, $\overline{\mathbf{I}}(\xi)$ (developed in the next section) of just two receivers. The filled aperture's map is readily generated using equation 5.1, and equation 4.11 gives the aggregate aperture's map. The driving question arising from the

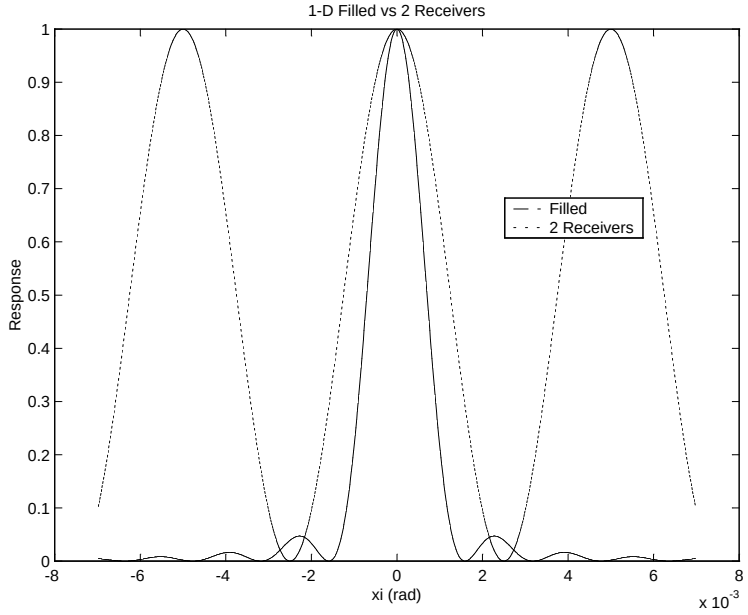

Figure 4.2 Placing two receivers at the maximum limits of a filled 1-dimensional aperture yields a poor approximation.

comparison is where to place the two receivers to most closely match the two intensity maps across the image line. In figure 4.2 this equates to minimizing the *area* between the graphs for the filled and the two-receiver aperture. From the Michelson interferometer of figure 3.1, the initial temptation for an aperture of width D_λ is to place the two receivers as far apart as possible, or at the ends of the slit D_λ apart. This actually yields a poor approximation of the complete filled aperture since its measurement of only the highest spatial frequency comes at the expense of generating large sidelobes in the reception pattern. These sidelobes represent reception angles receiving large amounts of interference. Moving the receivers

closer together reduces the size of these sidelobes, at the expense of widening the central peak. Across a finite image line, there is certainly an optimum separation of the two receivers to minimize the sum. Adding more discrete receivers to the aperture can shape the aggregate intensity map to look more and more like the filled aperture.

For an actual two-dimensional image plane, the comparison process is still the same, but another consideration arises. Whereas a one dimensional reference aperture has length as its only parameter, a two dimensional aperture has a size and a *shape*. For space-based interferometry, the shape of the reference should be influenced by the achievable loci of receiver paths. From the dynamics descriptions of section 2.1 and inspection of equations 2.2, the relative loci are *elliptical*, tracing out ellipses with a 2:1 ratio of major to minor axes. Ignoring these loci and choosing a circular shape for the comparison aperture is understandable since it has a known solution (section 5.2.2) and matches the shape of most primary mirrors, lenses, or filled antennas. Though mathematically simple this comparison is best limited to either instantaneous use or to receivers tracing out circular loci (*not* the case for a formation). Trying to force a formation's performance to mimic a circular aperture spawns the question of what to choose for the size of the circle; choosing either the major or minor axis causes difficulties, figure 4.3. A minor axis-sized aperture

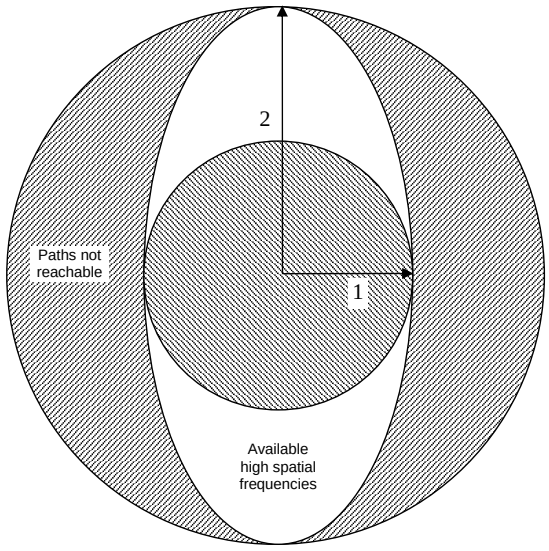

Figure 4.3 Comparing receivers tracing out elliptical loci to a *circular* aperture is dubious, whether the circle is defined as circumscribed or inscribed.

ignores fully half of the higher spatial frequencies measurable by receivers orbiting out to the extreme portions of the ellipse. An aperture sized to the major axis compares the receivers aggregate intensity map to an aperture with areas not reachable by the dynamics of the formation. Therefore, matching the comparison aperture shape to the receiver paths ensures that all achievable baselines are considered and that no potentially useful paths are ignored. With the reference aperture properly shaped, it offers the optimization routine a complete set of possible baselines and no impossible ones. The optimization process then has the task of choosing the most beneficial baselines to be sampled from this set.

4.3.2 Aggregate Apertures. Replacing a continuous aperture with a set of discrete receivers necessarily degrades its performance, but calculating the aggregate performance is not computationally challenging. The Superposition Principle [13] allows the signals from each receiver pair to be simply added algebraically. Consider the one-dimensional aggregate aperture in the last section with pair spacings A_k. Since each pair produces the map of a point source, the aperture's map is simply a finite summation of the real part[3] of the **PSF** for each pair. The normalized aggregate intensity map from equation 4.1 for N receiver pairs becomes

$$\overline{\mathbf{I}}(\xi) = \left[\frac{1}{N}\sum_{k=1}^{N}\mathbf{Re}\left(e^{-2i\pi A_k \xi}\right)\right]^2 . \tag{4.11}$$

Inspection of equation 4.11 reveals that each receiver pair contributes a $(\cos)^2$ function whose frequency is determined by the size of the spacing between the pair.

In two dimensions, each receiver pair contributes a baseline that supplies the $(\cos)^2$ distribution in one direction on the image plane, and a *constant* along the perpendicular direction, figure 4.4. Mimicking the filled two-dimensional aperture is therefore a search for optimal baseline lengths and orientations such that the aggregate intensity map resembles that generated by the filled aperture through a comparison at each (ξ, η) location.

[3]Due to the symmetry of the **PSF**, its imaginary part could just as well be chosen and squared to yield the intensity without loss of generality [13].

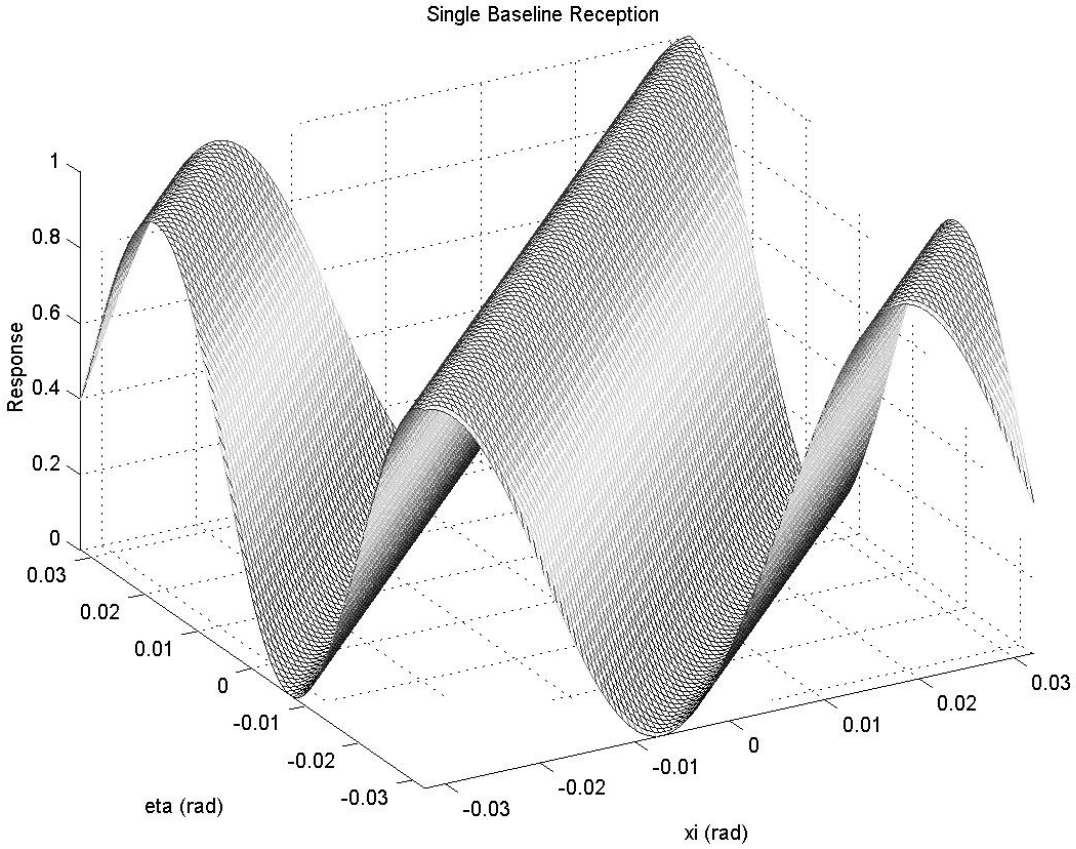

Figure 4.4 Each baseline contributes a two-dimensional $(\cos)^2$ function parallel to the baseline.

As discussed in section 4.2, early work by Kong and Miller [20] simplified the geometry of their search by assuming formations of matched pairs of receivers. This leads to simplified analytical expressions for the aggregate intensity map generated by N pairs of receivers, but this simplification was at the expense of inherently creating redundant baselines, figure 4.5.

By the Binomial Theorem, for $M = 4$ receivers, there are actually $P = \frac{M!}{2(M-2)!} = 6$ baselines. By forcing M receivers into symmetric pairs, baselines (4) and (6) are redundant. This redundancy is easily removed by no longer insisting on symmetric pairs. (In his thesis [21], Kong's optimizations allowed full two degree of freedom for receiver placement.)

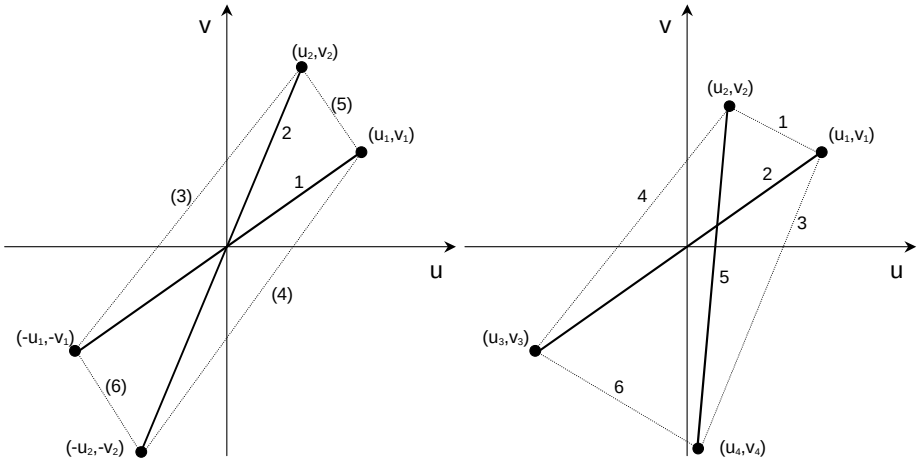

Figure 4.5 Summing the contributions from $N = 2$ pairs overlooks four other baseline pairings available. Individually locating $M = 4$ receivers potentially creates 6 unique baselines, therefore 6 spatial frequency measurements.

This generation of permutations may be easily formalized. Let P be the number of pair permutations that exist in the set of M receivers, and let $\mathbb{P}_2^M$ be the mapping that generates $\mathcal{B}$, the set of P pairs without order. The right diagram in figure 4.5 has a $\mathcal{B}$ of

$$\mathcal{B} = \mathbb{P}_2^M \left(\left\{ \begin{array}{c} (u_1, v_1) \\ (u_2, v_2) \\ (u_3, v_3) \\ (u_4, v_4) \end{array} \right\} \right) = \left\{ \begin{array}{c} (u_1, v_1)(u_2, v_2) \\ (u_1, v_1)(u_3, v_3) \\ (u_1, v_1)(u_4, v_4) \\ (u_2, v_2)(u_3, v_3) \\ (u_2, v_2)(u_4, v_4) \\ (u_3, v_3)(u_4, v_4) \end{array} \right\} = \left[\begin{array}{c} \mathcal{B}_1 \\ \mathcal{B}_2 \\ \mathcal{B}_3 \\ \mathcal{B}_4 \\ \mathcal{B}_5 \\ \mathcal{B}_6 \end{array} \right]. \tag{4.12}$$

Using this set, it is possible to generate the more complete permutational aggregate image intensity, $\overline{\mathbf{I_P}}(\xi, \eta, t)$.

$$\overline{\mathbf{I_P}}(\xi, \eta, t) = \sum_{k=1}^{P} \mathbf{I}(\mathcal{B}_k(t)) \tag{4.13}$$

Recall from Rohlfs [35], the absolute position of each receiver within the $(\vec{u}\ \vec{v})$ plane is not important. Measurements of the coherence function are strictly a function of the difference

between the positions[4] (equation 3.13). Therefore, for ease of visualization, translate the six permutations to give origin-centered loci.

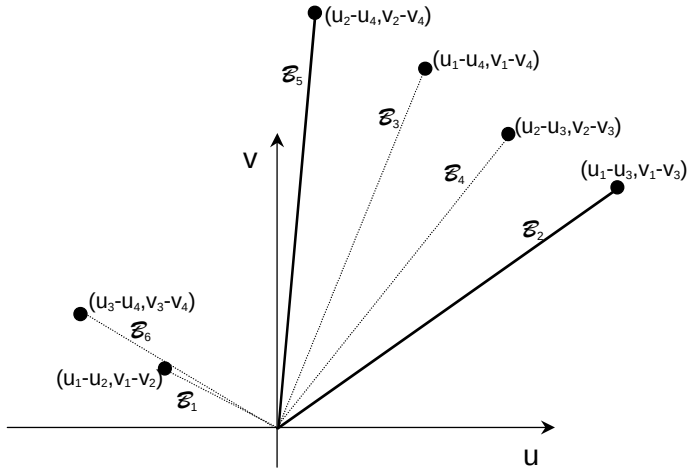

Figure 4.6 The six permutations available from four receivers can be translated to the origin, without changing the spatial frequency measurement.

Therefore the aggregate aperture intensity map of equation 4.11 expanded to two dimensions must be summed from 1 to P to include all permutations. For the full planar map, the normalized intensity becomes

$$\overline{\mathbf{I_P}}(\xi,\eta,t) = \left[\frac{1}{P}\sum_{k=1}^{P}\mathbf{Re}\left(e^{-2i\pi(\Delta u_k\xi+\Delta v_k\eta)}\right)\right]^2. \tag{4.14}$$

This is the normalized instantaneous aggregate intensity map.

The size of the image plane over which the comparison is performed has a direct impact on the required computation budget. Doubling the length of the axes quadruples the number of image intensity points that must be calculated and compared (unless the discretization is made more coarse). Note from figure 4.2 that the Bessel function which nearly always occurs in the $\mathbf{I_o}(\xi,\eta)$ for filled apertures falls off rapidly outside the central peak. Indeed, it is almost negligible after the third zero crossing. Looking at a generic

[4]Rohlfs' equations 6.10 and 6.17.

function of the form

$$\text{Response} = \left(\frac{J_1(A)}{A} \right)^2 \tag{4.15}$$

reveals zeroes at $A = [3.8317 \quad 7.0156 \quad 10.1735 \quad ...]$, figure 4.7. Limiting the plane of

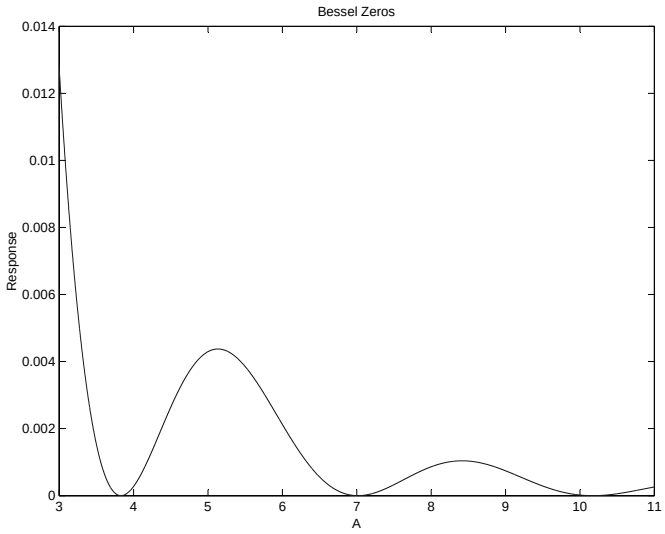

Figure 4.7 Graphing the square of a generic Bessel function from equation 4.15 out past 10 reveals zeros at $A = [3.8317 \quad 7.0156 \quad 10.1735]$.

comparison to lie within the first zero is overly restrictive, and essentially assumes a very sparsely filled image (objects in the sidelobe viewing locations are few). Moving out to the second Bessel zero creates a fairly large image plane. Moving out to the third Bessel zero creates a *very* large image plane with most of the reference function nearly zero. Such a comparison plane assumes a very densely populated image, and will drive an optimized array towards small spatial frequencies to yield these regions of near zero. This suggests performing the comparison over an image plane whose size is determined by the aperture D_λ, such that

$$\pi \ \xi_{\max} \ D_\lambda = \pm 7.0156 \quad . \tag{4.16}$$

This encompasses the first natural sidelobe or ring in the Airy disk, but does not devote expensive computation cycles to vast areas of near zero gain. (The effects of the regions between the second and third zeros are not totally ignored. The corners of a square image plane extend out into the small non-zero region between 7.0156 and 10.1735.)

4.4 Mean Formation Metrics

Nearly all interferometers increase the number of baselines sampled by dwelling on a target for some finite duration, during which time the receivers trace out paths in the $(\vec{u}\ \vec{v})$ plane. The aggregate intensity map of the previous section only yields an *instantaneous* measure of image errors. For receivers in constant independent motion, this metric may be generalized to include these instantaneous errors averaged over a finite time. For a satellite formation, such a metric offers optimal receiver paths such that imaging over time from *any* start time will suffer from minimal errors over some finite dwell time. Aside from reinforcing the need to consider path shapes as described in section 4.3.1, this adds yet another integral to the metric.

$$\mathbf{J}_{\text{image}}(\text{path}) = \int_{t_o}^{t_f} \int_{\eta_o}^{\eta_f} \int_{\xi_o}^{\xi_f} \left[\overline{\mathbf{I_P}}(\xi,\eta,t) - \mathbf{I_o}(\xi,\eta)\right]^2 d\xi d\eta dt \tag{4.17}$$

Since baseline geometries repeat every half rotation, a logical dwell time for a satellite formation might well be one half orbital period, $\frac{T}{2}$. Discretized over an $m \times m$ image plane and n time steps, this becomes

$$\mathbf{J}_{\text{image}}(\text{path}) = \frac{1}{n(m \times m)} \sum_{k=1}^{n} \sum_{j=1}^{m} \sum_{i=1}^{m} \left(\overline{\mathbf{I_P}}(\xi_i,\eta_j,t_k) - \mathbf{I_o}(\xi_i,\eta_j)\right)^2 . \tag{4.18}$$

Note that as developed, $\mathbf{J}_{\text{image}}(\text{path})$ is the average of the instantaneous metric over a imaging dwell time, *not* the effects of all baselines over time as compared to a perfect aperture. This is an important difference, as it generates optimal paths for yielding minimal image errors for *any* start time.

4.5 Summary

Moving interferometric receivers into orbit is a logical extension from terrestrial based arrays. The idea dates back to the early 1980s and fostered preliminary work on how to compare the performance of prospective arrays. The current best measure of merit for an array is a summation of its image plane intensity map errors as compared to a filled aperture. This is a difficult comparison. Assuming symmetric receiver placement yields

simple analytic expressions for discrete array performance, but at the cost of creating redundant baselines. Generalizing the mathematics to describe asymmetric arrays and time-dependence is not difficult, but keeping track of the rapidly expanding number of baselines with larger numbers of receivers is challenging. The aperture used as a reference must also be selected with the nature of receiver motion in mind if the metric is expanded to include time variations. A logical image plane size for the comparison may readily be found by observing the nature of a filled aperture's $\mathbf{I_o}(\xi, \eta)$. Several of these filled aperture maps are developed in the next chapter.

V. Apertures, Apertures, Apertures

A rigorous analysis of an optimal distributed aperture is not possible without first analyzing the basic physics of the finite, filled apertures used as references. This chapter reviews the intensity map generated by several regularly shaped apertures receiving electromagnetic radiation, then moves on to develop the output of an asymmetric aperture. Each is derived by integrating the **PSF** over the aperture geometry.

5.1 One Dimensional Apertures

The nature of a comparison-based image quality metric is most easily seen by first addressing a 1-dimensional continuous aperture (a slit). Though not particularly practical for generating an image[1] (an ideally focused image would only be ideal in one dimension), its performance is easily displayed. The 1-dimensional point spread function is readily integrated across a slit of width D_λ.

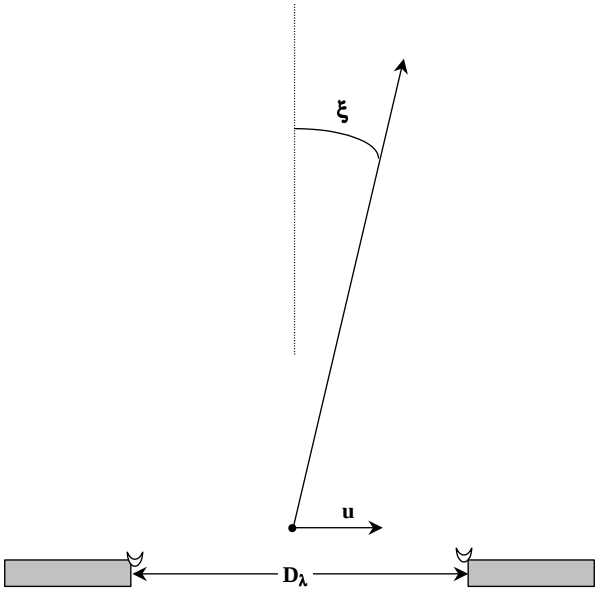

Figure 5.1 Integration of the point spread function across a 1-dimensional aperture, yields the intensity map over the single angular variable, ξ.

[1] The original Michelson interferometer was indeed a 1-dimensional system, but he sought only to measure the widths of nearby stars not to generate images of them. Therefore he was only interested in measuring the highest spatial frequency available to yield the best possible edge-detection of the stars' disks.

$$\mathbf{I_o}(\xi)_{1-\mathrm{D}} = \left[\int_{-\frac{D_\lambda}{2}}^{\frac{D_\lambda}{2}} e^{-2i\pi(u\xi)}du\right]^2 \tag{5.1a}$$

$$= \left[D_\lambda\left(\frac{e^{i\pi D_\lambda\xi} - e^{-i\pi D_\lambda\xi}}{2i\pi D_\lambda\xi}\right)\right]^2 \tag{5.1b}$$

$$= \left[D_\lambda\left(\frac{\cos\pi D_\lambda\xi + i\sin\pi D_\lambda\xi - \cos\pi D_\lambda\xi + i\sin\pi D_\lambda\xi}{2i\pi D_\lambda\xi}\right)\right]^2 \tag{5.1c}$$

$$= D_\lambda^2\left[\frac{\sin(\pi D_\lambda\xi)}{\pi D_\lambda\xi}\right]^2 \tag{5.1d}$$

The shape of the intensity mapping is determined by D_λ over all viewing angles ξ, and increases overall with increased slit width (easily normalized).

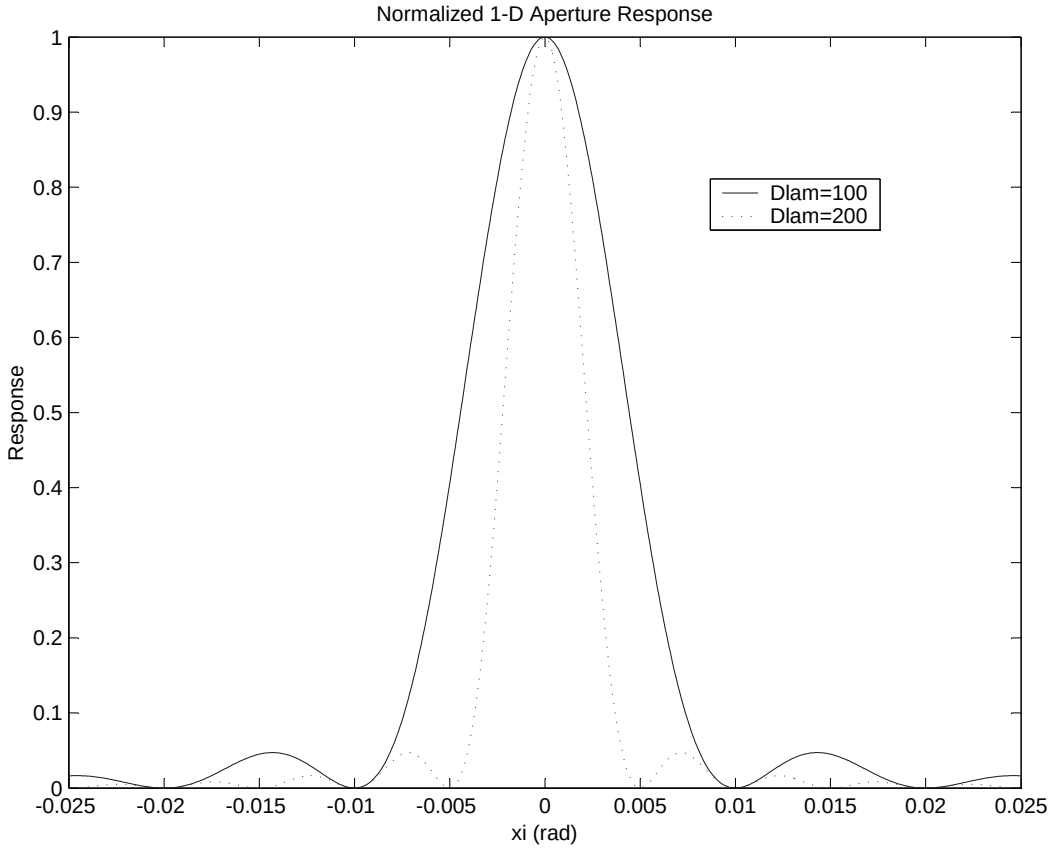

Figure 5.2 The single dimension, D_λ, of a one-dimensional aperture determines the shape of the intensity map over all look angles ($D_\lambda = 100$ wavelengths and $D_\lambda = 200$ wavelengths shown).

5.2 Two Dimensional Apertures

Filled two-dimensional apertures have some geometry in the ($\vec{u}$ $\vec{v}$) plane covered by a continuous receiver of some sort (the objective lens or primary mirror of a telescope are common examples). The intensity map created by such an aperture is generated by integrating the two-dimensional **PSF** over the whole aperture for each pair of viewing angles. For apertures with simple geometries (circles, squares), analytic solutions exist for the image plane intensity maps. An analytic solution for an *elliptical* aperture also has been developed[2], and the derivation is shown in section 5.2.3.

5.2.1 Square Apertures. The mathematically simplest aperture to integrate is certainly a square, since the point spread function may be split into two independent functions along the ξ and η axes.

$$\mathbf{I_o}(\xi,\eta)_{\text{square}} = \left[\int_{-\frac{D_\lambda}{2}}^{\frac{D_\lambda}{2}}\int_{-\frac{D_\lambda}{2}}^{\frac{D_\lambda}{2}} e^{-2i\pi(u\xi+v\eta)}dudv\right]^2 \tag{5.2a}$$

$$= \left[\int_{-\frac{D_\lambda}{2}}^{\frac{D_\lambda}{2}} e^{-2i\pi u\xi}du\int_{-\frac{D_\lambda}{2}}^{\frac{D_\lambda}{2}} e^{-2i\pi v\eta}dv\right]^2 \tag{5.2b}$$

$$= \left[D_\lambda\left(\frac{e^{i\pi D_\lambda\xi}-e^{-i\pi D_\lambda\xi}}{2i\pi D_\lambda\xi}\right)D_\lambda\left(\frac{e^{i\pi D_\lambda\eta}-e^{-i\pi D_\lambda\eta}}{2i\pi D_\lambda\eta}\right)\right]^2 \tag{5.2c}$$

$$= \left[D_\lambda\left(\frac{\cos\pi D_\lambda\xi+i\sin\pi D_\lambda\xi-\cos\pi D_\lambda\xi+i\sin\pi D_\lambda\xi}{2i\pi D_\lambda\xi}\right)\right.$$
$$\left.D_\lambda\left(\frac{\cos\pi D_\lambda\eta+i\sin\pi D_\lambda\eta-\cos\pi D_\lambda\eta+i\sin\pi D_\lambda\eta}{2i\pi D_\lambda\eta}\right)\right]^2 \tag{5.2d}$$

$$= \left[D_\lambda^2\left(\frac{\sin(\pi D_\lambda\xi)}{\pi D_\lambda\xi}\right)\left(\frac{\sin(\pi D_\lambda\eta)}{\pi D_\lambda\eta}\right)\right]^2 \tag{5.2e}$$

[2]Based on extensive literature search, the author believes this to be an *original* derivation for this type of aperture.

Mapped over a discretized image plane, this generates a planar-symmetric intensity map, figure 5.3.

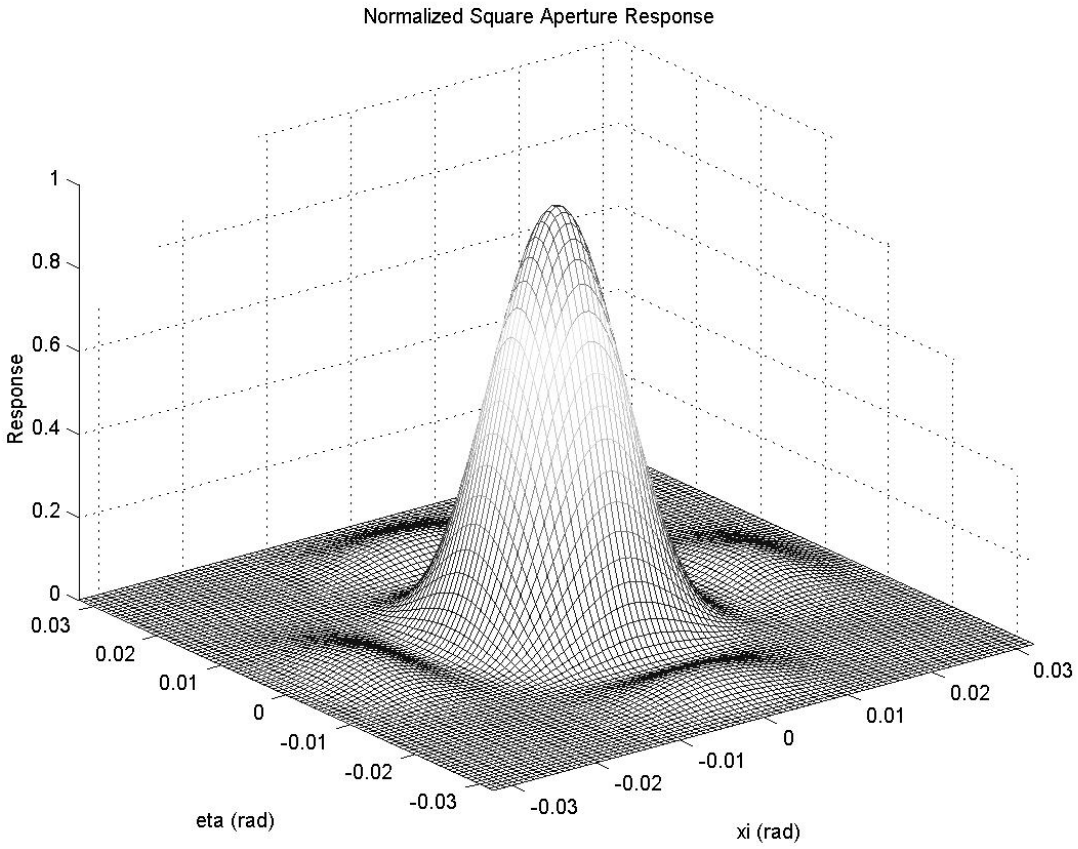

Figure 5.3 A square aperture's intensity map is the product of two 1-dimensional maps. This map is generated by a square aperture $D_\lambda = 100$ each side. The intensity or response given over the image plane is depicted as the *height* of the surface.

Though seldom used, this is the best response a square lens or primary mirror of dimension D_λ could yield for a point source.

5.2.2 Circular Aperture. As discussed in section 4.3.1, a circular aperture's intensity map is not quite adequate for use as a reference for formation performance. Its derivation is worthwhile, however, since it may be extrapolated to an elliptical aperture. A normalized intensity map of an aperture may be stepwise built by determining the Fourier transform of the point spread function from the spatial frequency domain, normalizing it by the *maximum* power reception pattern, then squaring it to yield an intensity [13].

$$\mathbf{I_o}(\xi,\eta) = \left[\frac{f(\xi,\eta)}{f_{\max}(\xi,\eta)}\right]^2 \tag{5.3}$$

With this approach, the square aperture derivation may be modified to a more practical circular aperture by a natural conversion to polar coordinates in both the spatial and spatial frequency domains. Following a derivation by Rohlfs [35], convert aperture positions (u,v) to the polar coordinates (r,θ) and viewing angles (ξ,η) to the coordinates (ρ,ϕ).

$$\begin{aligned} u &= r\cos\theta & \qquad \xi &= \rho\cos\phi \\ v &= r\sin\theta & \qquad \eta &= \rho\sin\phi \end{aligned}$$

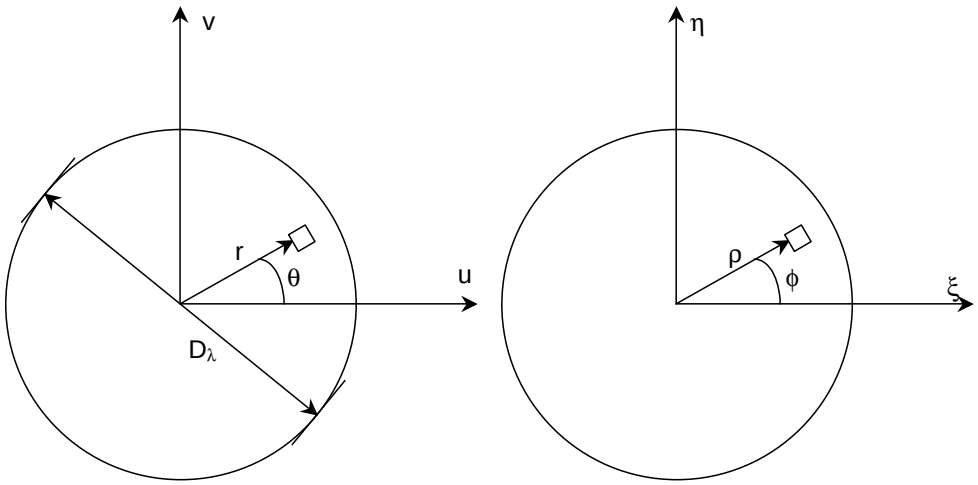

Figure 5.4 In the spatial frequency domain, convert aperture positions (u,v) to the polar coordinates (r,θ). In the spatial domain, shift viewing directions (ξ,η) to the coordinates (ρ,ϕ).

The non-normalized power reception pattern is converted by

$$f(\xi,\eta) = \frac{1}{2\pi}\iint_A e^{2i\pi(u\xi+v\eta)}dudv \tag{5.4a}$$

$$f(\rho) = \frac{1}{2\pi}\int_0^{\frac{D_\lambda}{2}}\int_0^{2\pi} e^{2i\pi\rho(r\cos\theta)}\ r\ d\theta dr, \tag{5.4b}$$

where the reception pattern dependence on ϕ is immediately removed by axial symmetry. One integral may be removed by rearranging,

$$f(\rho) = \int_0^{\frac{D_\lambda}{2}} \frac{1}{2\pi} \int_0^{2\pi} e^{2i\pi\rho(r\cos\theta)} d\theta \; r \; dr, \tag{5.5}$$

and noting the definition of the Bessel function (J_o) of the first kind of order 0 for any value α

$$J_o(\alpha) = \frac{1}{2\pi} \int_0^{2\pi} e^{i\alpha\cos\theta} d\theta. \tag{5.6}$$

Setting $\alpha = 2\pi\rho r$ allows equation 5.5 to be rewritten as

$$f(\rho) = \int_0^{\frac{D_\lambda}{2}} J_o(2\pi\rho r) \; r \; dr. \tag{5.7}$$

The normalized intensity map may now be constructed by noting the maximum value of J_1 is 1. Performing the normalization and squaring yields

$$\mathbf{I_o}(\rho) = \left[\frac{\int_0^{\frac{D_\lambda}{2}} J_o(2\pi\rho r) r dr}{\int_0^{\frac{D_\lambda}{2}} r dr} \right]^2. \tag{5.8}$$

A change of variables $z = 2\pi\rho r$ allows[3]

$$\begin{aligned} \mathbf{I_o}(\rho) &= \left[\frac{\int_0^{D_\lambda \pi\rho} J_o(z) \frac{z}{2\pi\rho} \frac{dz}{2\pi\rho}}{\int_0^{\frac{D_\lambda}{2}} r dr} \right]^2 && \text{(5.9a)} \\ &= \left[\frac{\frac{1}{4\pi^2\rho^2} \int_0^{D_\lambda \pi\rho} J_o(z) z dz}{\frac{D_\lambda^2}{8}} \right]^2 && \text{(5.9b)} \\ &= \left[\frac{2}{D_\lambda^2 \pi^2 \rho^2} \int_0^{D_\lambda \pi\rho} J_o(z) z dz \right]^2 && \text{(5.9c)} \end{aligned}$$

[3]This point in the derivation corrects a misprint by Rohlfs who asserted $\frac{2}{D_\lambda \pi\rho}$ 5.9c.

Again noting the property of Bessel functions [13] that

$$\int_0^\beta \alpha J_o(\alpha) d\alpha = \beta J_1(\beta), \tag{5.10}$$

allows the last integral to be replaced by a Bessel function (J_1) of the first kind of order 1.

$$\mathbf{I_o}(\rho) = \left[\frac{2}{D_\lambda^2 \pi^2 \rho^2}(D_\lambda \pi \rho) J_1(D_\lambda \pi \rho)\right]^2 \tag{5.11a}$$

$$= \left[\frac{2J_1(D_\lambda \pi \rho)}{D_\lambda \pi \rho}\right]^2 \tag{5.11b}$$

This intensity map yields the classic Airy disk pattern with a central peak of width inversely proportional to the aperture diameter D_λ, figure 5.5. Note that the pattern is symmetric

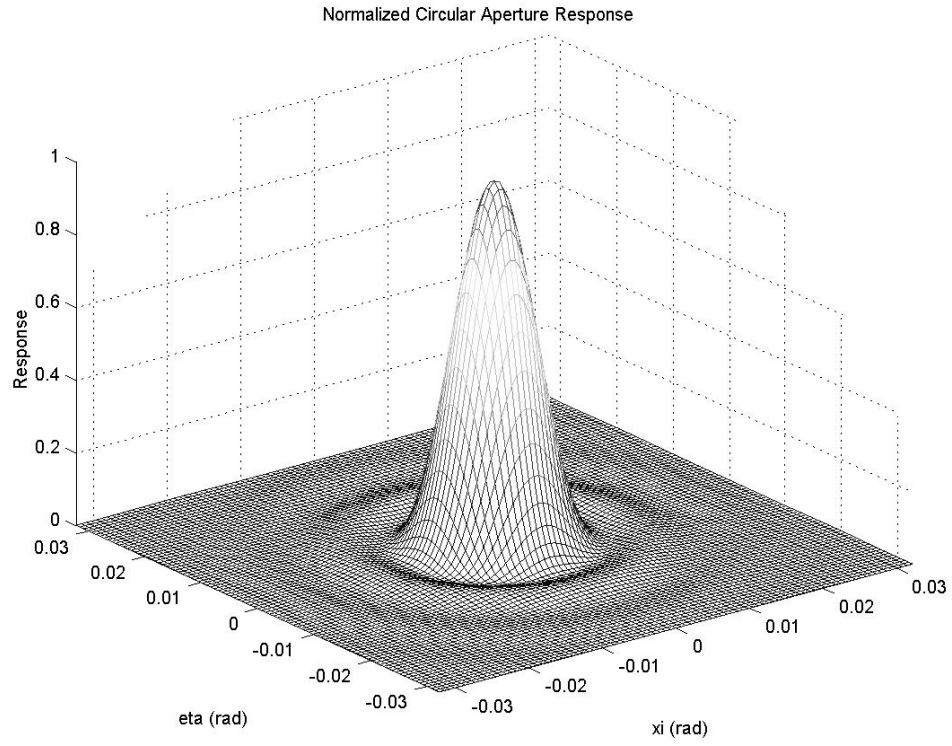

Figure 5.5 The Airy disk pattern resulting from a circular aperture of diameter $D_\lambda = 100$ is shown here over a discretized set of viewing angles.

about the normal vector of the image plane (θ does not appear in equation 5.11b).

5.2.3 Elliptical Apertures. The intensity map generated by an elliptical aperture may be extrapolated from a circular aperture to yield the reference described in section 4.3.1 shaped to match the elliptical loci of formation elements. Begin with the non-normalized intensity map of equation 5.3, and assume an elliptical aperture with its semi-minor axis, b, and semi-major axis, a, aligned with the $(\vec{u}\ \vec{v})$ axes respectively. The conversion to polar coordinates is essentially the same, figure 5.6. With an *asymmetric*

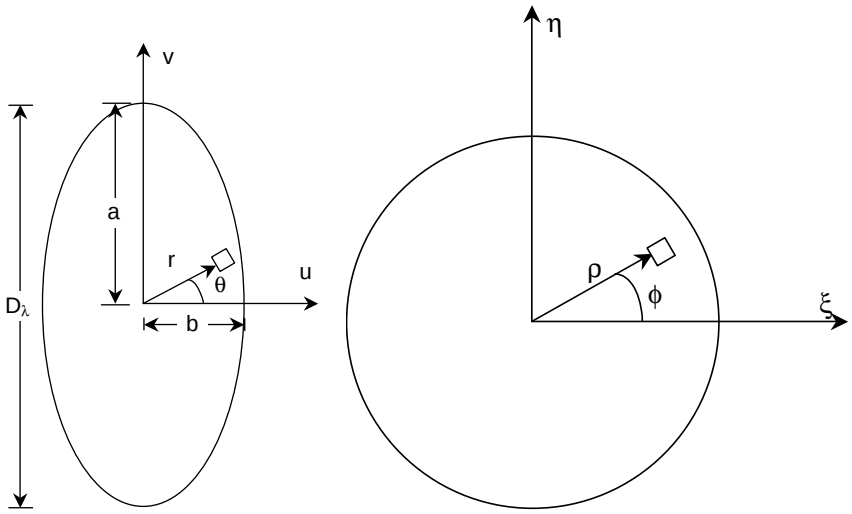

Figure 5.6 An elliptical aperture's intensity can use the same conversions to polar coordinates in both domains as used for a circular aperture.

aperture, however, the spatial domain contributions to the intensity map are no longer symmetric about the aperture normal. This alters the limits of the inner integration to a function of the angle, θ, though the Jacobian for the conversion is still just r.

$$f(\xi,\eta) = \frac{1}{2\pi}\iint_A e^{2i\pi(u\xi+v\eta)}du\ dv \tag{5.12a}$$

$$f_{\text{ellipse}}(\rho,\phi) = \frac{1}{2\pi}\int_0^{2\pi}\int_0^{R(\theta)} e^{2i\pi(\rho\cos\phi)(r\cos\theta)}r\ dr\ d\theta \tag{5.12b}$$

The outer radius of the aperture, $R(\theta)$, may be derived from the parametric representation [44] of an ellipse

$$u(\theta) = b\ \cos\theta$$
$$v(\theta) = a\ \sin\theta$$

The equation of the outer radius is found readily.

$$\begin{aligned} R^2(u,v) &= u^2(\theta) + v^2(\theta) \\ R^2(\theta) &= (b\ \cos\theta)^2 + (a\ \sin\theta)^2 \\ R(\theta) &= \sqrt{(b\ \cos\theta)^2 + (a\ \sin\theta)^2} \end{aligned}$$

Inserting this into equation 5.12b gives the basic polar representation of the intensity map.

$$f_{\text{ellipse}}(\rho,\phi) = \frac{1}{2\pi}\int_0^{2\pi}\int_0^{\sqrt{(b\cos\theta)^2+(a\sin\theta)^2}} e^{2i\pi(\rho\cos\phi)(r\cos\theta)}\ r\ dr\ d\theta \tag{5.15}$$

Since the limits of the inner radius integral are *not* a constant radius, but a function of the outer variable of integration, θ, the order of integration may *not* be interchanged to build a Bessel function of the first kind (as in the circular aperture). However, $f(\rho,\phi)$ is only needed to generate an intensity map over an arbitrary image plane. The image plane may just as well be square and mapped in cartesian coordinates, $f(\xi,\eta)$. Such an $f(\xi,\eta)$ may be derived two different ways.

The most direct and least efficient derivation of $f(\xi,\eta)$ is to numerically integrate equation 5.15 over a discretized aperture. A simple cartesian integrator may be employed across a circumscribed square in the $(\vec{u}\ \vec{v})$ plane if a logic statement is added which drives the integrand to zero outside the elliptical radius.

$$f_{\text{ellipse}}(\xi,\eta) = \frac{1}{2\pi}\int_{v_o}^{v_f}\int_{u_o}^{u_f} e^{2i\pi(u\xi+v\eta)}\left[\left(\frac{u^2}{a^2}+\frac{v^2}{b^2}\right)\le 1\right] du\ dv \tag{5.16}$$

This method is computationally taxing, since each point in the discretized image plane must be calculated via numerical integration across the entire aperture ellipse[4]. Nevertheless, it is certainly feasible and yields an intensity map with a familiar appearance, figure 5.7. Not surprisingly, the contraction of the elliptical aperture along the $\vec{u}$ axis causes an elongation of the intensity map peak and sidelobes along the $\vec{\xi}$ axis.

[4]Figure 5.7 required 25.5 hours of computation on a 1GHz PC, using MatLab's standard variable-stepsize double integration function `dblquad(...)`.

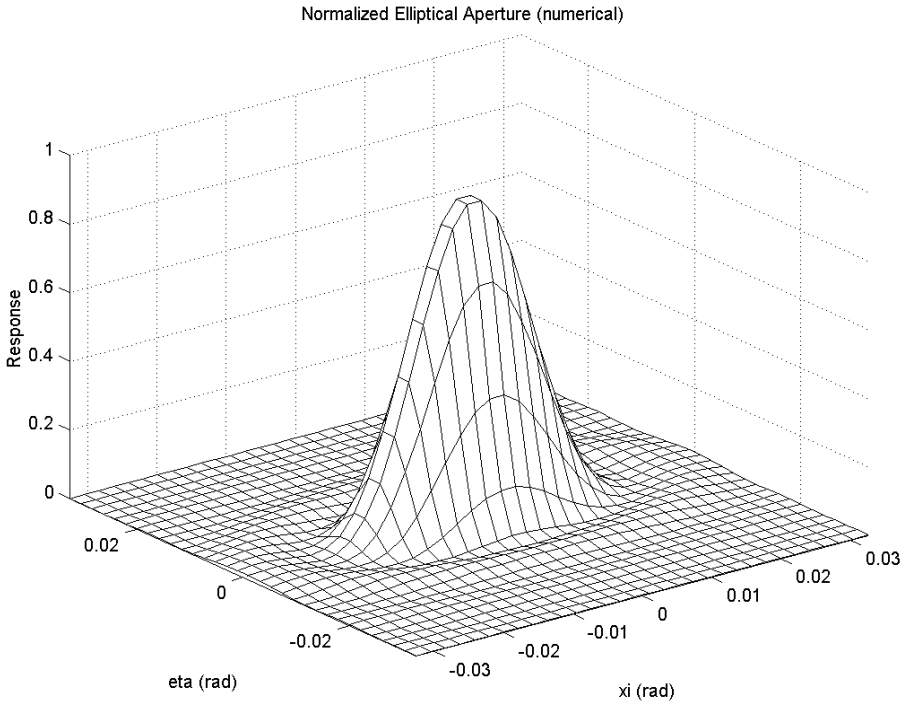

Figure 5.7 An elliptical aperture may be laboriously integrated numerically for each set of look angles to yield an intensity map $\mathbf{I_o}(\xi, \eta)_{\text{ellipse}}$.

Equation 5.15 may be solved in a more elegant fashion by readdressing the problem of directly determining $f(\xi, \eta)$ through an approach resembling one used by Johannes Kepler. Kepler solved the difficult problem of elliptic satellite motion by mapping the known solution for circular motion about a circumscribed circle onto the ellipse [49].

By circumscribing a circle of diameter D_λ about the elliptical aperture, it is apparent that the ellipse is simply a circular aperture contracted by the ratio of $\frac{b}{a}$ in the $\vec{u}$ direction, figure 5.8. This suggests defining an eccentric radius, r'. The coordinate transformation in the spatial frequency domain is modified to

$$u' = \tfrac{b}{a}u = \tfrac{b}{a}r\cos\theta$$
$$v' = v = r\sin\theta$$

or

$$\tfrac{a}{b}u' = r\cos\theta$$
$$v' = r\sin\theta$$

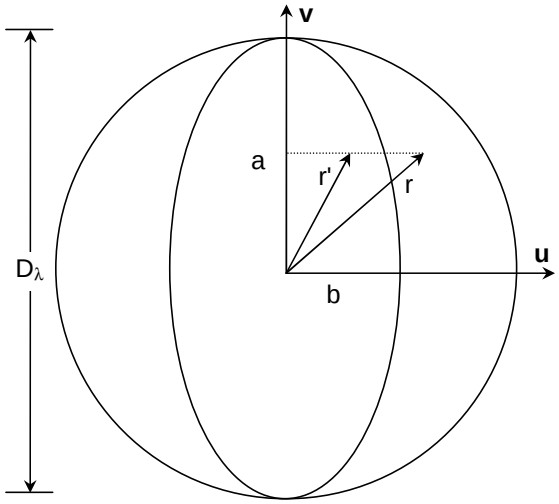

Figure 5.8 Circumscribing a circle about the elliptical aperture highlights mapping the circular aperture response at r to the eccentric radius $r' = \sqrt{\left(\frac{b}{a}u\right)^2 + v^2}$. The major axis of the ellipse is D_λ.

This is just the original polar coordinate system used to solve the circular aperture, modified by the eccentricity of the ellipse. Since the coordinate transformation from (u, v) to (r, θ) is the same as from $(\frac{a}{b}u', v')$ to (r, θ), the polar point spread function may be written

$$\mathbf{PSF}_{\text{ellipse}}(r, \theta, \rho') = e^{2i\pi\rho'(r\cos(\theta))} \tag{5.18}$$

in terms of an image plane eccentric radius, ρ', where

$$\rho'^2 = \left(\frac{b}{a}\xi\right)^2 + (\eta)^2 \tag{5.19a}$$

$$\rho' = \sqrt{\left(\frac{b}{a}\xi\right)^2 + (\eta)^2}. \tag{5.19b}$$

The **PSF** may be transformed back to its Cartesian form, carrying along the $\frac{b}{a}$ contraction along the $\vec{u}$ direction.

$$\mathbf{PSF}_{\text{ellipse}}(u', v', \xi, \eta) = e^{2i\pi(u'\xi + v'\eta)} \tag{5.20a}$$

$$\mathbf{PSF}_{\text{ellipse}}(u, v, \xi, \eta) = e^{2i\pi(\frac{b}{a}u\xi + v\eta)} \tag{5.20b}$$

$$\mathbf{PSF}_{\text{ellipse}}(u, v, \xi, \eta) = e^{2i\pi(u(\frac{b}{a}\xi) + v\eta)}. \tag{5.20c}$$

The last bit of algebra highlights the similarity to the circular aperture, with the eccentric effects transferred to the *spatial* domain. This allows the double integration of equation 5.20c to be accomplished across u and v in the same manner as the circular aperture, yielding $f(\rho')$.

$$f(\xi,\eta)_{\text{ellipse}} = \frac{1}{2\pi}\int_{v_o}^{v_{max}}\int_{u_o}^{u_{max}} e^{2i\pi(u\frac{b}{a}\xi+v\eta)}dudv \tag{5.21a}$$

$$f(\rho')_{\text{ellipse}} = \frac{1}{2\pi}\int_{0}^{\frac{D_\lambda}{2}}\int_{0}^{2\pi} e^{2i\pi\rho'(r\cos\theta)}\ r\ d\theta dr \tag{5.21b}$$

$$f(\rho')_{\text{ellipse}} = \int_{0}^{\frac{D_\lambda}{2}} J_o(2\pi\rho' r)\ r\ dr \tag{5.21c}$$

The normalized intensity map may be constructed by noting the maximum value of J_o is still 1. Performing the normalization and squaring yields

$$\mathbf{I_o}(\rho')_{\text{ellipse}} = \left[\frac{\int_0^{\frac{D_\lambda}{2}} J_o(2\pi\rho' r)rdr}{\int_0^{\frac{D_\lambda}{2}} rdr}\right]^2 \tag{5.22a}$$

$$\mathbf{I_o}(\rho')_{\text{ellipse}} = \left[\frac{2J_1(D_\lambda\pi\rho')}{D_\lambda\pi\rho'}\right]^2 \tag{5.22b}$$

By direct substitution of equation 5.19b the intensity map for an elliptic aperture becomes

$$\mathbf{I_o}(\xi,\eta)_{\text{ellipse}} = \left[\frac{2J_1\left(D_\lambda\pi\sqrt{\left(\frac{b}{a}\xi\right)^2+(\eta)^2}\right)}{D_\lambda\pi\sqrt{\left(\frac{b}{a}\xi\right)^2+(\eta)^2}}\right]^2 \tag{5.23}$$

This is a far more efficient solution to implement[5], figure 5.9.

[5]Figure 5.9 took less than 2 seconds to generate with the same workstation over the same discretized plane as figure 5.7.

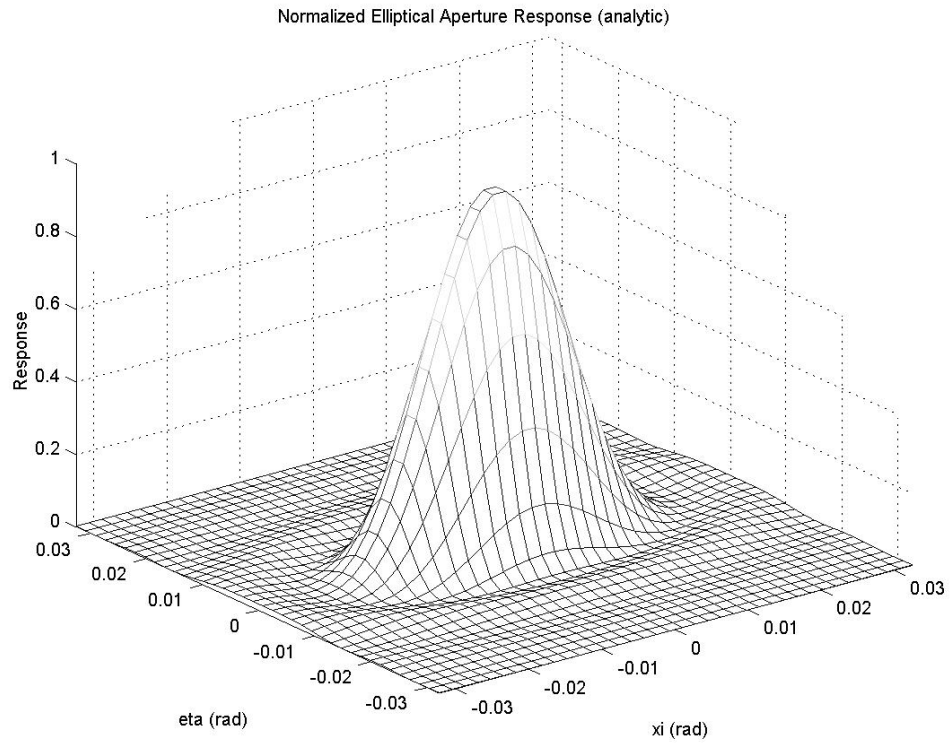

Figure 5.9 The analytic solution to the elliptical aperture may easily be implemented over a discretized image plane.

Note that equation 5.23 yields the circular aperture intensity map if $a = b$, or along the $\xi = 0$ axis. Setting $\eta = 0$ shows that the aperture is essentially contracted by the ratio of $\frac{b}{a}$ in the $\vec{u}$ direction, causing an expansion of the Bessel function along the $\vec{\xi}$ axis.

5.3 Summary

Analytic expressions are derived here for the intensity maps generated by filled apertures of regular shapes. Integrating the **PSF** over an area yields the well-known solutions for square and circular apertures, but neither of these known shapes conform to the elliptical loci of receivers in a satellite formation, and is therefore not quite suitable for use as the reference aperture in an interferometry metric. A filled elliptical aperture has an analytic $\mathbf{I_o}(\xi, \eta)$, and is derived over a square image plane by a conversion to eccentric polar coordinates in the aperture (an approach generalized in chapter VII).

VI. Optimization of Formation Geometries

With the metrics of chapter IV in hand, it is possible to begin the task of actually searching for optimal geometries for conceptual systems. It is immediately apparent that such searches are complex, even for simple systems. This chapter begins by exploring the non-convex nature of the comparison metrics, even for the simplest formations. A one-dimensional formation is solved explicitly, and demonstrates the need for a global search routine. A genetic algorithm is introduced as a powerful means to find an acceptably close approximation of the optimum receiver geometry for more complex formations. The algorithm is verified with a simple idealized array set up on the North Pole, then for both a constrained collinear planar array and a general planar array, both with ideal viewing geometries.

6.1 Non-Convexity

The receiver placement problem as posed is non-convex. This may be seen in the simplest of all systems, a one-dimensional linear array[1].

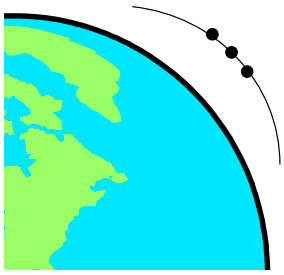

Figure 6.1 A line of co-orbiting satellites is the simplest possible formation, with $\rho = 0$ for each element and $b \neq 0$ for all but the first receiver.

For a one-dimensional array the intensity map, $\overline{\mathbf{I}}(\xi)$, simplifies equation 4.9 to

$$\mathbf{J} = \frac{\sum_{i=1}^{m} \left[\overline{\mathbf{I}}(\xi_i) - \mathbf{I_o}(\xi_i)\right]^2}{m}. \tag{6.1}$$

[1]This one-dimensional problem actually describes a satellite formation system, one in which all receivers have identical orbital parameters except for a slight variance in mean anomaly (an unsophisticated, yet valid satellite formation).

From figure 4.2, the distance chosen between each pair of receivers determines the frequency of the $(\cos)^2$ function they generate. Adjusting this distance varies the cumulative difference between the filled aperture response and the discrete receiver response. This cumulative error is easily plotted for a single pair of receivers over a gap varying from $[0.0 \ldots 1.0] \times D_\lambda$, figure 6.2. Minimizing this error obviously requires finding the global

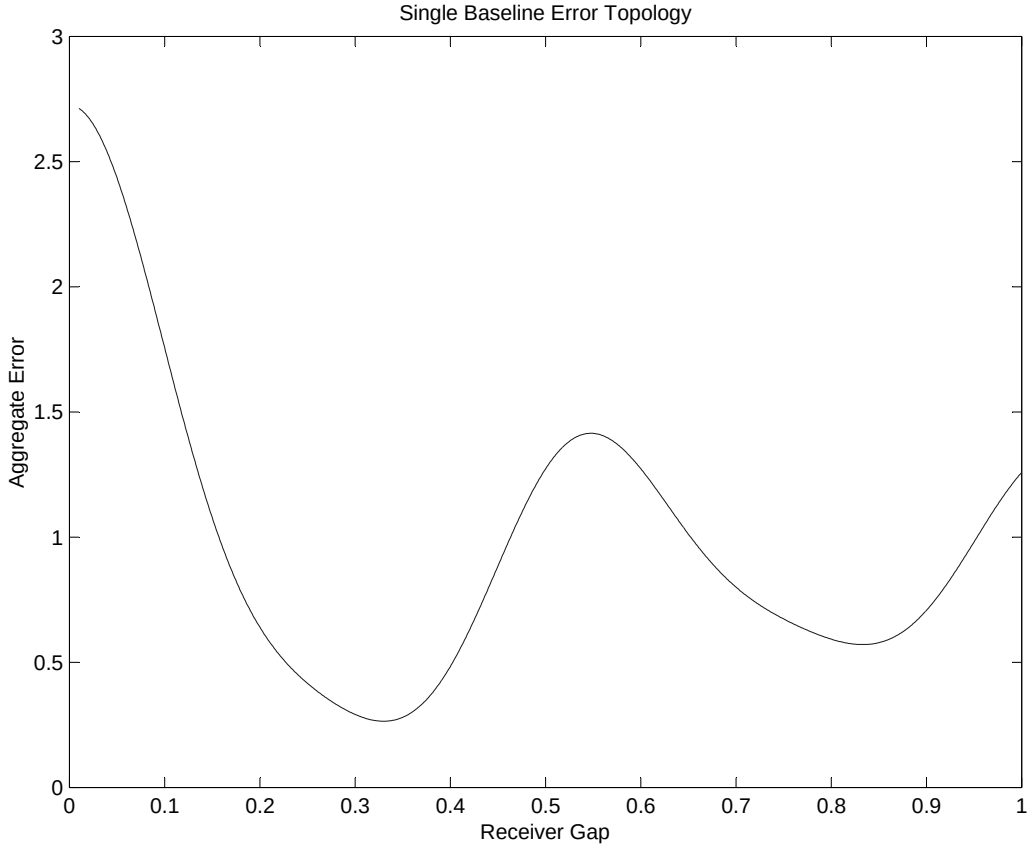

Figure 6.2 Varying the gap between discrete receivers up to a maximum of D_λ shows two local minima, one is obviously the global.

minimum at $0.33 \times D_\lambda$ and avoiding the local minimum at $0.83 \times D_\lambda$.

Placing a third receiver in the aperture immediately complicates the problem. By locking one at the origin[2], the problem has one degree of freedom for each of the two

[2]Fixing the position of one receiver is actually an important point. Since the discrete aperture response is a function only of the difference between receiver locations [35], allowing the full degrees of freedom for all receivers creates a solution space that resembles a Dirichlet [43] function. The true minimum *relative* geometry exists in an infinite number of positions within the aperture. This distinction, though discernable in his results, was not specifically cited in Kong's work [21].

remaining receivers.

$$\begin{aligned} \text{Error}^2 &= \left(\overline{\mathbf{I}} - \mathbf{I_o}\right)^2 \\ &= \left(\left[\frac{1}{3} \sum_{k=1}^{3} \mathbf{Re}\left(e^{-2i\pi(\Delta u_k \xi)} \right) \right]^2 - D_\lambda^2 \left[\frac{\sin(\pi D_\lambda \xi)}{\pi D_\lambda \xi} \right]^2 \right)^2 \end{aligned}$$

Sliding the two receivers around from $[0.0 \ldots 1.0] \times D_\lambda$, summing the contributions of the three baselines, and differencing them from a filled one-dimensional aperture results in a two-dimensional surface of error flux, with four minima, figure 6.3. By symmetry, two of them are copies of the global at $D_\lambda \times (0.28, 0.73)$ and $D_\lambda \times (0.73, 0.28)$. (This illustration

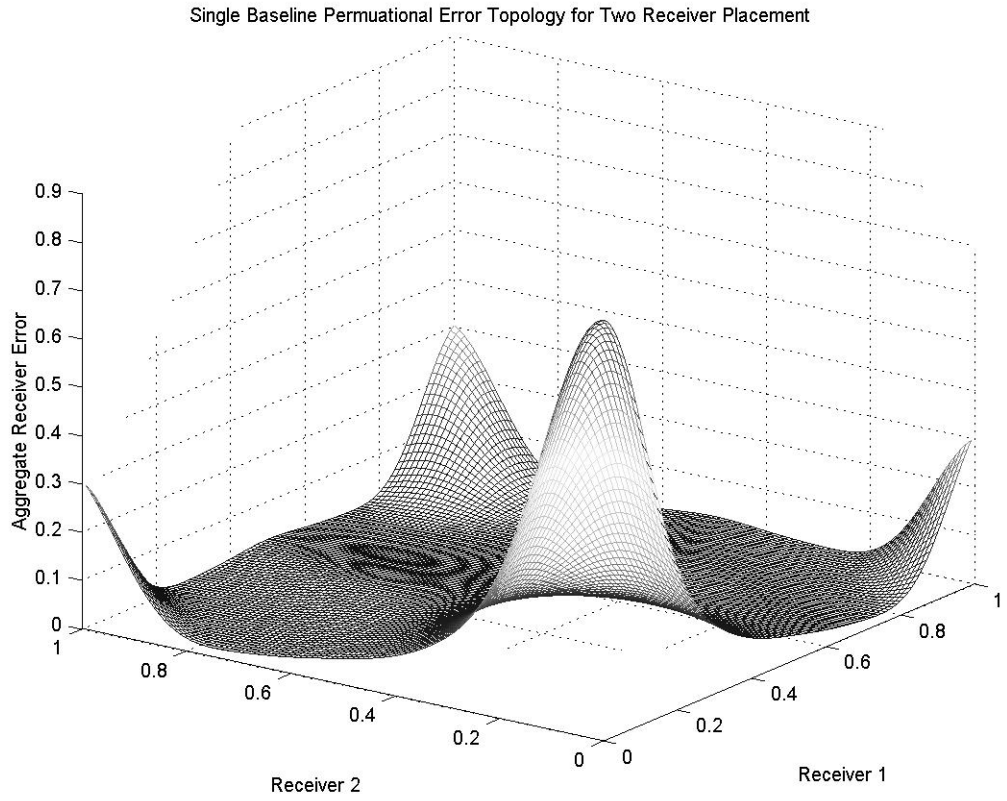

Figure 6.3 Varying the placement of two discrete receivers in a one-dimensional aperture from the origin out to a maximum of D_λ adjusts three baselines. The aggregate aperture's error shows four local minima, two are symmetric copies of the global.

also highlights the limitations of graphically depicting error surfaces. Two receivers moving in one-dimension use up all available plotting dimensions.)

6.2 A Genetic Algorithm

Navigating around such multi-dimensional surfaces to approximate a global minimum immediately suggests a numeric approach. Due to its non-convex nature, simple hill-climbing (descending) searches may be immediately discounted since these approaches are susceptible to getting caught in local minima. Kong, Miller, and Sedwick employed a Simulated Annealing technique [21] that used a global search, slowly reduced in scope by lowering a theoretical "temperature" of the system. Another popular technique (and the one selected here) is the use of *genetic algorithms*. With fine enough gene definition, the standard genetic process builds chromosome structures that represent the defining parameters for each receiver's paths. Finite-sized populations of such structures accumulate the configurations yielding minimal errors. Successive generations of crossovers and mutations vary these parameters within the solution space and reevaluate the fitness of offspring members.

A conservatively constructed set of genes yields complete numerical freedom for each parameter to desired precision. This research employed a simple real valued numeric and scaling set.

Gene	Value	Gene	Value
gene1	1	gene8	8
gene2	2	gene9	9
gene3	3	gene10	0.1
gene4	4	gene11	0.01
gene5	5	gene12	0.001
gene6	6	gene13	0.0001
gene7	7	gene14	0.00001

Table 6.1 This simple set of genes certainly spans the solution space, and provides for multiple means of defining each normalized chromosome.

By constructing chromosomes as sums and differences of genes 1 through 9, each scaled by genes 10 through 14, a population of coefficients densely populating the range $[-1.0 \ldots 1.0]$ may be generated to an accuracy of five decimal places[3]. Such a population of generic

[3]The range $[-1.0 \ldots 1.0]$ offers more flexibility than $[0.0 \ldots 1.0]$ in numerically selecting parameters. The selection routine set up to use this range suffers less infant mortality from chromosomes violating constraints.

chromosomes may be used to scale each degree of freedom in a formation, regardless of its dimensionality. This set is actually quite flexible, since the use of addition and subtraction allows a numeric value to be built several redundant ways, i.e. $0.98 = \text{gene9} \times \text{gene10} + \text{gene8} \times \text{gene11}$ or $0.98 = \text{gene1} - \text{gene2} \times \text{gene11}$. This flexibility allows a desirable set of chromosomes to be constructed in many ways by the searching algorithm. Just as the simulated annealing technique of Kong, Miller, and Sedwick used a heuristically chosen cooling rate for the system "temperature" to eventually halt the search, genetic searches may be performed for an empirically chosen large number of generations to arrive at an acceptably close approximation of the optimal set of parameters. The definition of "large

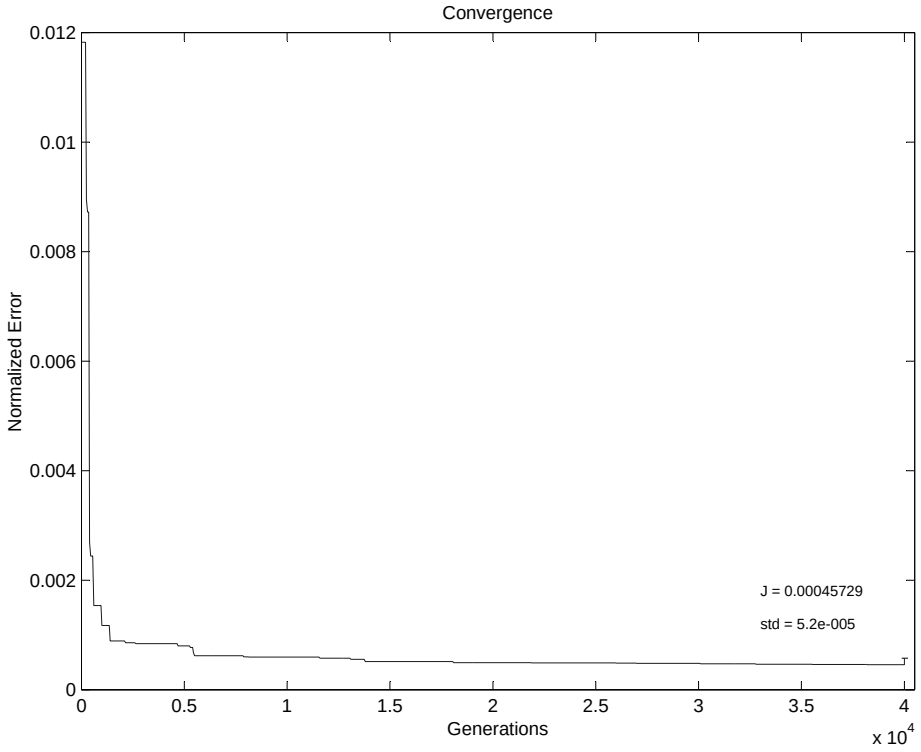

Figure 6.4 An appropriate number of generations for performing the genetic algorithm may be determined empirically by monitoring the best objective value of the populations. By construction, each search exhibits a monotonically decreasing objective, asymptotically approaching that of the true solution.

number of generations" grows with the degrees of freedom in the formation, but may be determined by monitoring the best fitness value for the populations during the course of the search, figure 6.4. As the search progresses, by construction the best fitness value

exhibits a monotonically decreasing behavior. With each generation of the search, the algorithm refines the geometry of the formation based on this optimization process. Since this algorithm is by nature a stochastic search, a truly exhaustive search would require performing the search multiple times and performing statistical validation of the results. However, this research only seeks validation of the problem formulation and the practicality of approximated solutions. Note that the solution surface of $\mathbf{J}_{\text{image}}$ remains analytic for any size formation, figure 6.5. Though "ugly," the summation formulation for $\overline{\mathbf{I_P}}(\xi, \eta, t)$ has no discontinuities. Likewise, derivatives for the Bessel function formulation of $\mathbf{I_o}(\xi, \eta)$ all exist[4]. Therefore a single search of each *smooth* error surface is performed to find an

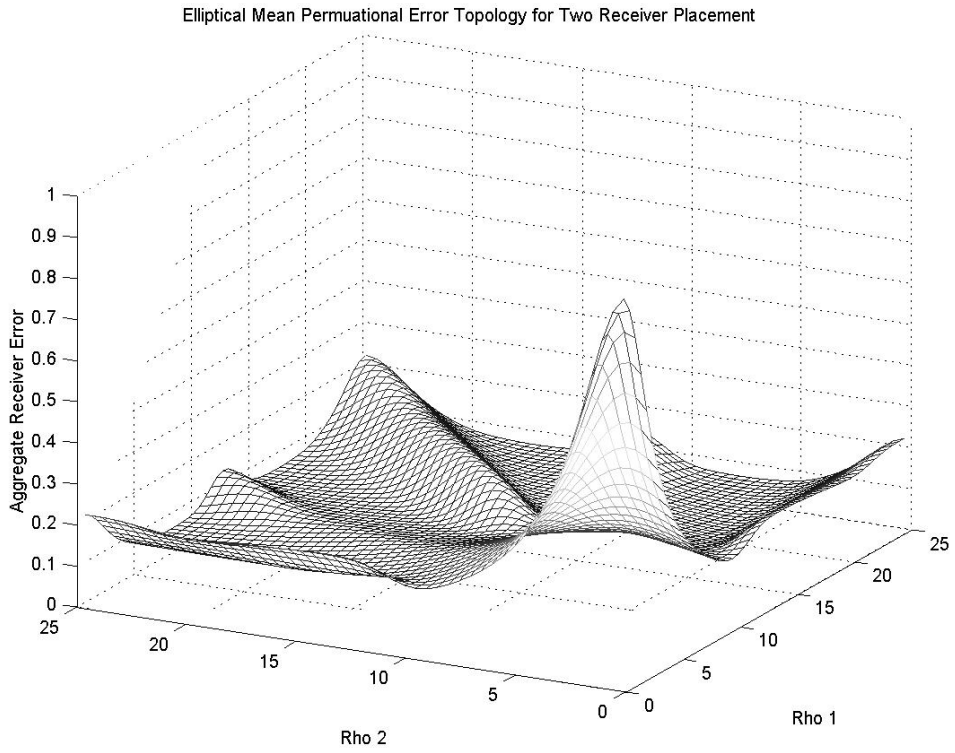

Figure 6.5 A similar technique to that used in figure 6.3 may be used to generate a surface plot of $\mathbf{J}_{\text{image}}$ for a two degree of freedom formation. The loci and performance of a planar collinear formation (section 6.4) with three receivers is determined by the selection of ρ_H for the two movable vehicles.

acceptable approximate solution among the many non-unique possible solutions.

[4]Any standard mathematics handbook [10] gives the expanded approximation of the Bessel function in a form like $J(x)_n = \sum_{k=0}^{\infty} \frac{(-1)^k \left(\frac{x}{2}\right)^{n+2k}}{k!\Gamma(n+k+1)}$, which is another exercise in differentiation, but the derivatives exist.

The overall process for this genetic algorithm is summarized in the logic flow of table 6.2. (A more extensive description is included as Appendix E.)

Step	Operation
1	Define gene pool.
2	Define initial chromosomes.
3	Generate population of coefficient chromosomes for each degree of freedom.
4	Evaluate fitness (normalized error) of initial populations, equation 4.18.
5	If population is too large trim chromosomes with highest fitness.
6	Select chromosomes for genetic operation, random, weighted for chromosomes with lower fitness values.
7	Perform crossover/mutation operations on chromosomes.
8	Convert new chromosomes to numerical values.
9	If constraints satisfied, calculate fitness of new chromosomes, otherwise delete.
10	If less than maximum number of generations, go to 5.
11	Manual check for convergence. (yes, continue; no, increase maximum generations, go to 5)
12	Generate array performance outputs.

Table 6.2 This algorithm summarizes the standard programming logic [34] used to perform the genetic searches in this investigation.

The validity of this single search process is supported by an example stochastic search. Figure 6.4 is actually one of ten repeat searches performed for a five-receiver general planar formation (introduced in section 6.5), each with different sets of initial conditions. The results of the searches showed very little dispersion about the mean (standard deviation of $\sigma = 0.0000520$). This small dispersion is illustrated by the tiny 2σ error bar drawn above

Search	$\mathbf{J}_{\text{image}}$	Search	$\mathbf{J}_{\text{image}}$
1	0.00046534	6	0.00049152
2	0.00057438	7	0.00054121
3	0.00052650	8	0.00059671
4	0.00058134	9	0.00051591
5	0.00045729	10	0.00059498
		σ	0.00005200

Table 6.3 Actually performing multiple searches for the smallest formation in section 6.5 shows a very narrow distribution about the mean.

the final generation in figure 6.4. This interval statistically encompasses 95.449% of the numerically approximated least upper bounds [48] on the true minimum $\mathbf{J}_{\text{image}}$.

Since the error surface of $\mathbf{J}_{\text{image}}$ is analytic for any size formation and the example stochastic search for a small formation demonstrates a very narrow dispersion of solutions, performing single searches for larger formations should not risk drastic deviations away from the true minimum aggregate error, and is deemed adequate for valid solution approximations.

This research used a modified form of the program architecture set forth by the Genetic Search Toolbox® by Optimal Synthesis Inc.® [26]. The toolbox provides functions for generating genes, chromosomes, and populations as character string representations. Genetic operations (crossovers, mutations) are performed on the character strings, which must then be evaluated to yield numerical values for the fitness (aggregate error). The basic search structure recommended by the toolbox authors was expanded to provide progress updates, a graphical convergence display, and user-controllable extension of the search generations seeking the behavior described by Rahmat-Samii and Michielssen [34]. Each search is performed until successive reductions in the objective function appear to be less than 10% of the latest $\mathbf{J}_{\text{image}}$.

6.3 A Simplified Polar Array Example

The basic problem definition and solution technique may be illustrated through analysis of an interferometric array with a simple geometry. A terrestrial array distributed

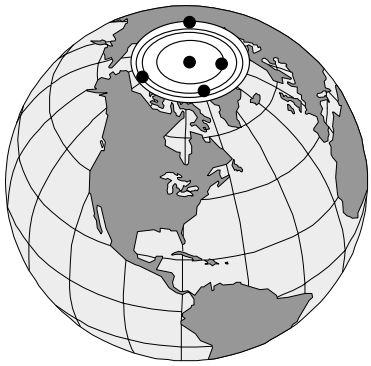

Figure 6.6 An array of receivers distributed about a pole offers very simple propagation and path loci.

about the North Pole offers perfectly circular receiver paths and elementary propagation, figure 6.6. For imaging high declination targets, a dwell time of half a sidereal day may

be assumed, which further reduces the dimensionality of the problem. Since a rotation of 180° swings each baseline through all possible orientations, a linear array, determined only by radial distance, eventually offers all the performance of more complex geometries (though instantaneous or "snapshot" performance will be poor). The circular paths also suggest the simplification of comparing the array to a filled circular aperture, with the known solution from section 5.2.2.

Consider setting up such an array of five receivers, one at the pole and the others arrayed about it. This system has four degrees of freedom, requiring four generic populations, each selecting a radial distance, $[-1.0 \ldots 1.0] \times \frac{D_\lambda}{2}$. For purposes of non-dimensionality, select the maximum array diameter[5] as $D_\lambda = 100$ wavelengths. Monitoring the best ap-

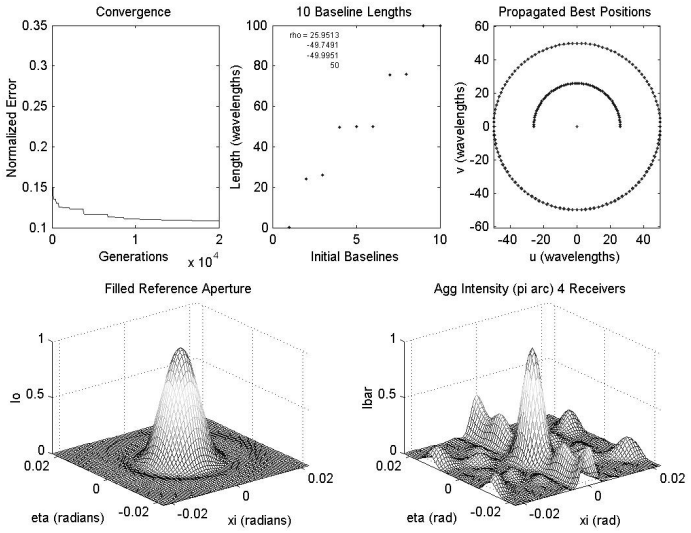

Figure 6.7 After 20,000 generations, a solution for five receivers tracing out paths about the North Pole minimizes its aggregate error as compared to a circular apertures. The baseline distribution demonstrates the natural inclusion of near-maximum length baselines, with enough short baselines to reduce sidelobe development of the high spatial frequencies.

proximation in the populations at the end of each generation shows that a single search of 20,000 generations appears sufficient to achieve a near-optimal solution for receiver spacings whose performance closely mimic the circular aperture. The lower right graphic in

[5]For purposes of consistency, the convention of setting the largest dimension of an aperture to $D_\lambda = 100$ wavelengths is followed throughout this work whenever an arbitrary aperture size must be selected.

figure 6.7 shows the performance of such an array over a 180° arc. Inspection of the chosen radii for the array show an almost perfect distribution of baseline lengths, including near-maximum length (for high spatial frequencies) and one of minimal length (necessary to minimize the sidelobes in the composite intensity map). Even for this simplified problem, this solution exists in several locations on the $\mathbf{J}_{\text{image}}$ surface. Simply trading the assignment of ρ for pairs of receivers gives several equivalent solutions.

Four receivers is not quite sufficient to demonstrate receiver placement trends, so the array was expanded to nine receivers, figure 6.8. This creates an eight degree of freedom problem, and the solution technique is the same, it just requires 50,000 generations for con-

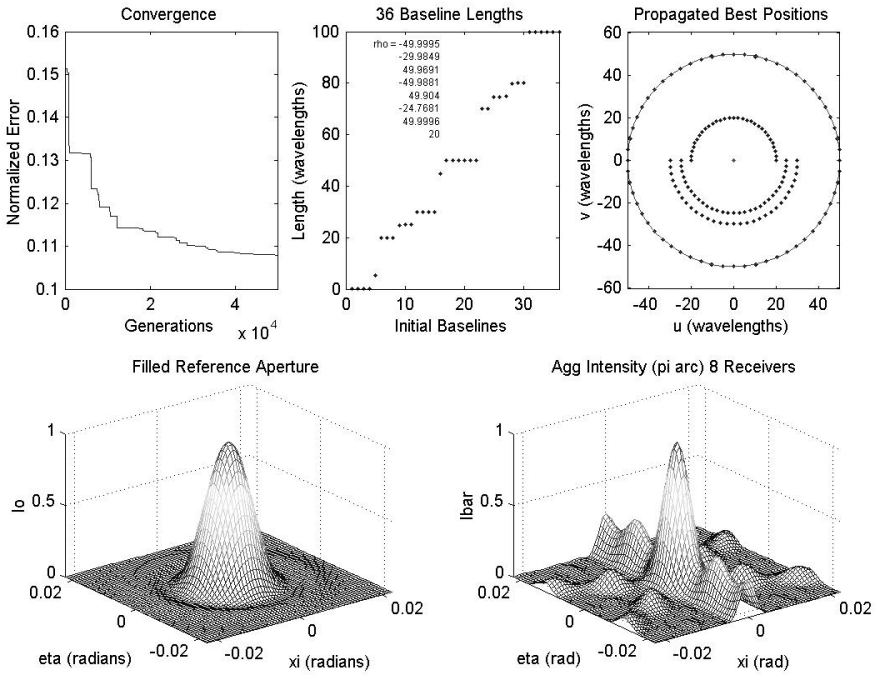

Figure 6.8 After 50,000 generations, an optimized array of nine receivers about the North Pole takes advantage of its ability to more densely fill the ($\vec{u}$ $\vec{v}$) plane.

vergence. (Recall that at this complexity, doubling the degrees of freedom creates nearly four times the number of baselines of the smaller array. This not only increases the run time for the simulation to propagate the receivers over 180°, but vastly increases the number of possible relative receiver locations. Only judicious selection of the correct members of each population for crossover/mutation or removal keeps the search to a practical dura-

tion[6]. The optimized distribution shows the necessary inclusion of many maximum-length baselines, but over half of the permutation baselines are still chosen to yield the shorter lengths, giving the low spatial frequencies needed to generate a complete image (review figure 3.9).

6.4 Optimizing a Planar Collinear Formation

The notion from section 4.4 of optimizing receiver motion over time necessitates including path shape information into the selection of a reference aperture. The simple circular paths of the previous section rarely happen for actual systems. From the descriptions of Wiesel [54], and inspection of equations 2.2, receivers in a formation of satellites trace out ellipses in the $(\hat{e}_x, \hat{e}_y)$ plane of their local coordinate system. For high relative declination targets, this defines the $(\vec{u}\ \vec{v})$ plane for all practical purposes (an assumption that is relaxed in the next chapter). Therefore for any choice of m_H and n_H defining the plane for the formation and for any choice of the two remaining Hill's parameters ρ_H and θ_H, the receivers' paths trace out ellipses with a 2:1 ratio of major to minor axes (eccentricity of $\frac{\sqrt{3}}{2}$).

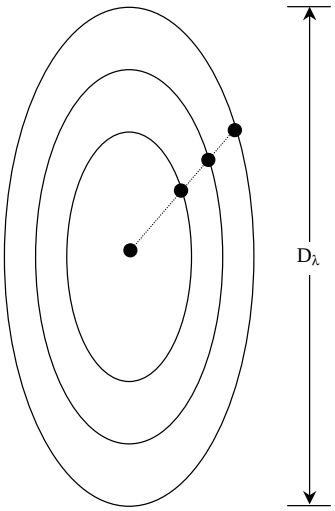

Figure 6.9 A planar formation may be further simplified by assuming a common θ_H for each receiver. A 180° loci rotates these baselines through every possible orientation.

[6]The optimization depicted in figure 6.8 took nearly five days to converge on a 1.7 GHz workstation.

Choosing a reference aperture that mimics these loci avoids the inconsistencies described in section 4.3.1. An initial problem may be simplified by choosing a comparison time of half an orbit [32], figure 6.9. This removes a degree of freedom from each receiver (just as the half-day period did for the polar array) since each baseline rotates through all possible orientations. Such a linear array's receiver paths may be specified by a selection of ρ_H only. Again, this simplification would never be used in a practical system, since the snapshot performance is unreasonably poor, figure 6.10. (Though the baselines' *lengths*

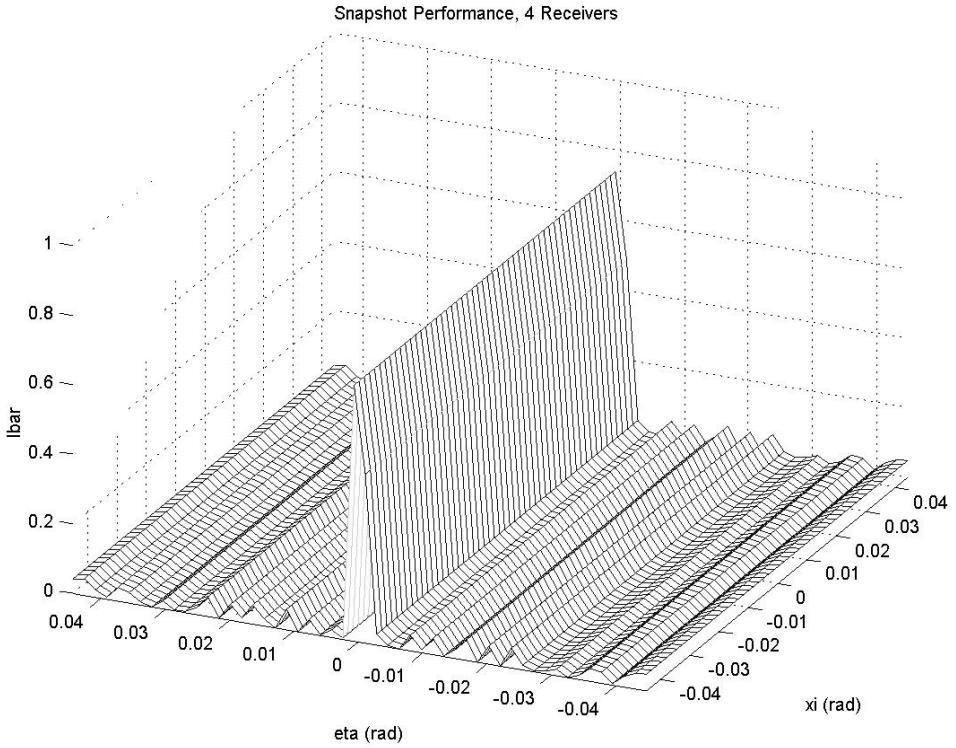

Figure 6.10 Simplifying a planar array to stay in a line within the $(\hat{e}_x, \hat{e}_y)$ plane may yield adequate performance over some dwell time, but the instantaneous or "snapshot" performance is only a one-dimensional distribution.

also change over the course of the dwell time, each length/orientation will eventually be sampled in a 180° arc.)

Beginning with a modest formation of nine receivers, the problem has eight degrees of freedom, eight values of ρ_H chosen from the range[7] $[-1.0 \ldots 1.0] \times \frac{D_\lambda}{4}$. Figure 6.11

[7] Recall the definition of ρ_H from Hills equations.

shows just such an optimized formation. Note the distribution of baseline lengths in this

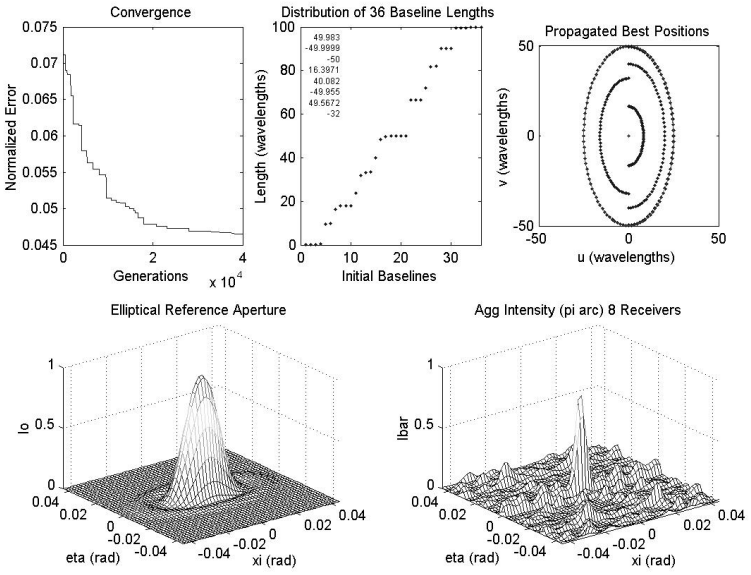

Figure 6.11 Optimizing a nine receiver formation for half an orbit puts the dimensionality of the problem to just eight, and 40,000 generations provide convergence.

figure. This is perhaps the most informative formation description, since it determines the sampled spatial frequencies at each discrete time. As expected, the solution locations include provisions for several maximum length baselines, and a nearly uniform sampling of the other lengths over the $(\vec{u}\ \vec{v})$ plane.

To see the utility of comparing the formation's performance to a filled *elliptical* reference, temporarily ignore the shape of the receiver paths, and attempt to drive the formation to mimic a simple circular aperture. The choice for such an aperture falls to either a smaller, inscribed circular aperture, or a larger, circumscribed aperture (see figure 4.3). Figure 6.12 shows the same nine-receiver formation just created, but optimized as compared to a small circular aperture. (Note the smaller reference aperture generates a *wider* peak in the image plane.) Hampered by a poor reference standard, the optimization accepts suboptimal geometries that generate the wider peak of its reference, apparent in the reduced number of near-maximum length permutational baselines generated.

Comparing the distributed formation to a larger, circumscribed circular aperture fares better in the optimization as compared to the inscribed circular reference. Parts

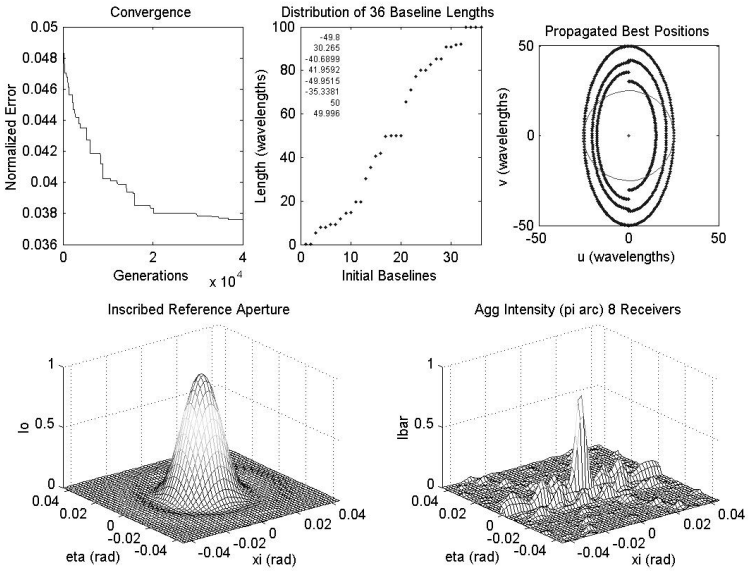

Figure 6.12 Optimizing the nine receiver formation compared to a smaller inscribed circular aperture sized to match the minor axis yields a formation that fails to optimally construct baselines filling the $(\vec{u}\ \vec{v})$ plane.

of the optimal paths in the reference are not reachable by the formation members but a similar solution as the smaller reference is eventually found, figure 6.13.

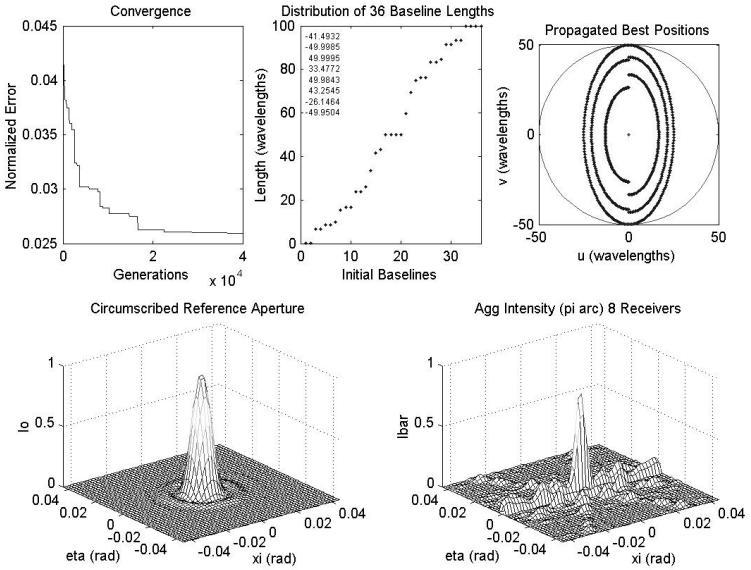

Figure 6.13 Optimizing the same nine receiver formation compared to a larger circular aperture sized to match the major axis eventually yields a comparable result to the elliptical reference.

This comparison suggests reduction to a lower ordered problem to gain some insight into what the optimization is generating. Keeping the relative linear geometry at each time step, but halving the number of non-fixed receivers decreases the degrees of freedom to four (for a five-receiver formation), figure 6.14. With the reduced number of baselines,

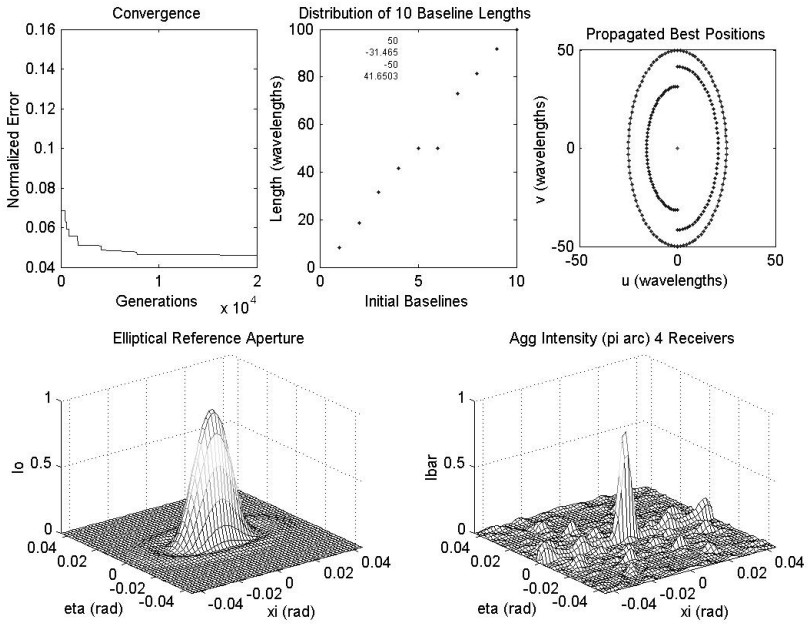

Figure 6.14 Optimizing a five receiver formation offers a lower-dimensionality comparison of comparison metrics. This optimization required 20,000 generations for convergence, and displays the same, though sparser distribution as figure 6.11.

the overall distribution of lengths include provisions for a maximum-length sample and a nearly uniform sampling of the rest over the $(\vec{u}\ \vec{v})$ plane.

Driving the smaller formation to mimic a small circular aperture's performance yields a similar distribution. Figure 6.15 shows the same five-receiver formation just created but optimized as compared to an inscribed circular aperture. The wider central peak generated by a smaller aperture again allows the optimization search to more readily accept suboptimal geometries, apparent in the lack of a maximum-length permutational baseline.

Performing the same optimization with a large circular aperture has similar results to the elliptical reference, figure 6.16. In fact, at the lower dimensionality it is possible to see

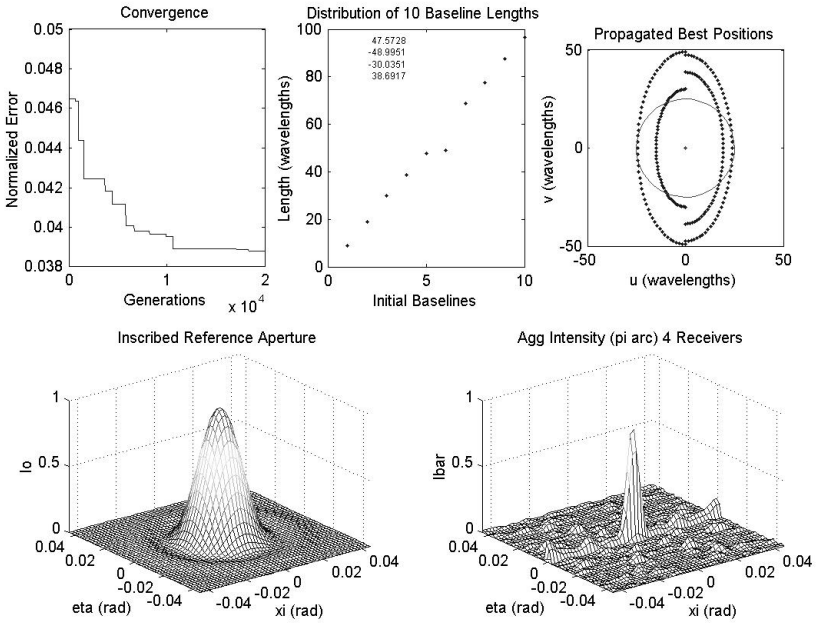

Figure 6.15 Optimizing the five receiver formation referenced to a smaller circular aperture still allows it to accept suboptimal performance due to the wider central peak of a small aperture.

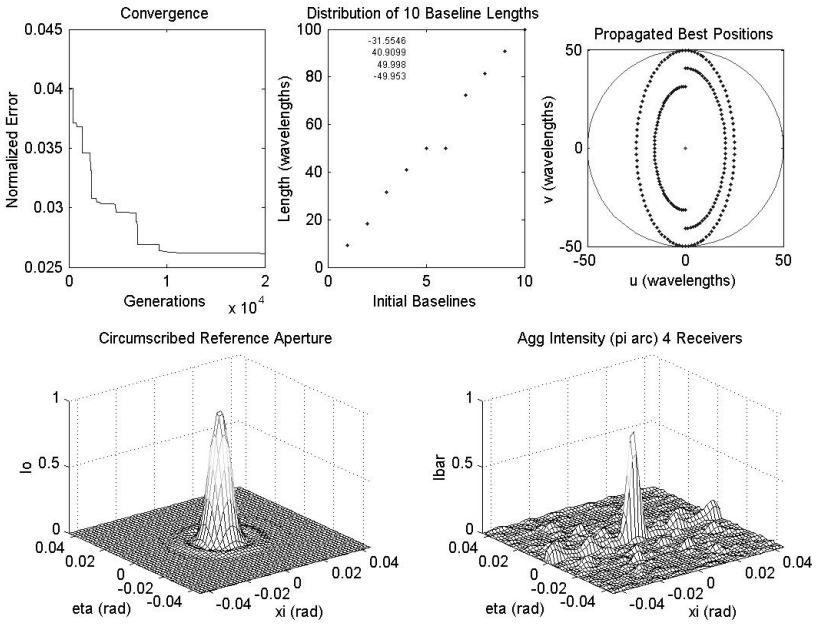

Figure 6.16 Optimizing the same five receiver formation compared to a larger circular aperture sized to match the major axis eventually yields a comparable result to the elliptical reference.

the nearly perfect one-to-one correspondence with the solution offered by the elliptically referenced solution. The optimization based on the larger circular reference eventually drives the receiver placement out to the constraints of the dynamics. Note, however, that both figures 6.15 and 6.16 show a much more sluggish convergence performance than the optimization based on the more appropriate elliptical reference.

6.5 Optimizing a General Planar Formation

Though the linear formations of section 6.4 were instructive for simple solutions and comparisons, they suffer from poor "snapshot" performance. Since each would require very long dwell times to yield acceptable images, it is unlikely such a geometry would ever be selected. A more realistic formation allows complete freedom of receiver placement within the formation plane[30], figure 6.17.

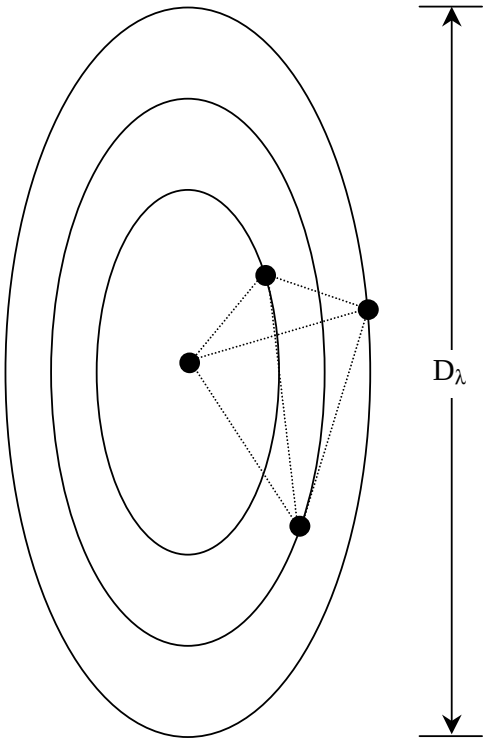

Figure 6.17 A planar formation provides a natural definition of the $(\vec{u}\ \vec{v})$ plane. Receivers in the formation trace out simple 2:1 ellipses, but the permutational baselines may have fairly varied orientations, depending on the *relative* locations of the receivers.

Consider another five receiver formation, figure 6.18, with one receiver locked at the origin. Each receiver may be placed by selecting both its ρ_H and θ_H at the expense of

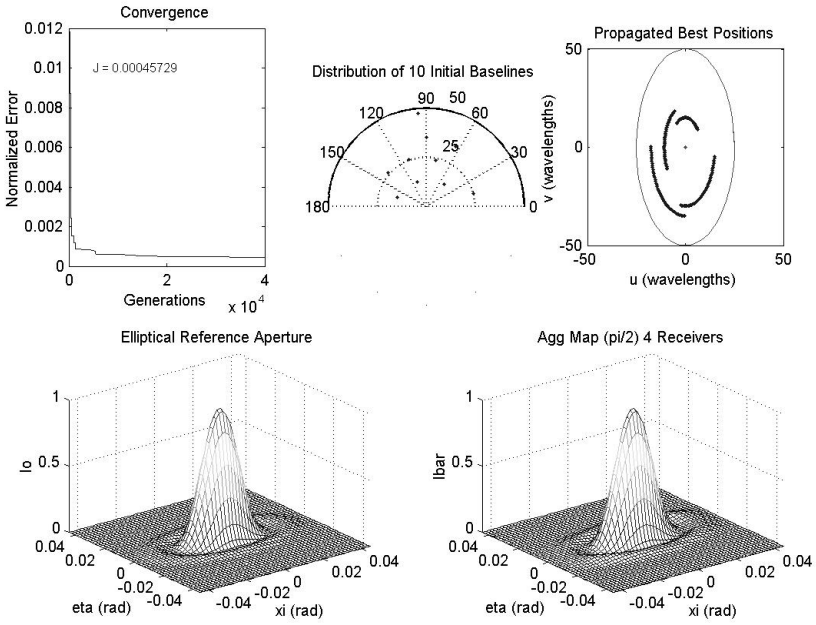

Figure 6.18 Optimizing the five receiver formation of section 6.4 may be readily enhanced to allow two degrees of freedom per receiver. Placing one receiver at the origin leaves eight degrees of freedom in the formation. The enhanced performance over summing the linear arrays is immediately apparent.

doubling the degrees of freedom. The formation's instantaneous performance is now quite reasonable. The simulation time is also reasonable. Though eight populations must be generated, there are still only four receivers to propagate and ten baselines to be generated for the aggregate performance at each time step. Since an initial θ_H may be chosen for each receiver, the dwell time may be halved to investigate which baseline orientations are the most beneficial.

If the genetic algorithm is allowed to select $\rho_H = [-1.0 \ldots 1.0] \times \frac{D_\lambda}{4}$ and $\theta_H = [-1.0 \ldots 1.0] \times 90°$, a dwell time of one quarter orbit offers all possible orientations, but *not* all possible baseline lengths (a more realistic limitation). Figure 6.18 depicts such an optimized formation. Since simple initial baseline length is no longer sufficient to illustrate the sampled spatial frequencies, figure 6.18's distribution diagram has been modified to a polar depiction to show the length and *orientation* of all initial permutational baselines.

The inclusion of near-maximum length baselines is apparent, but the shorter comparison time drives them to be repeated at several orientations.

Figures 6.19 through 6.22 show the successive improvements in formation performance by simply adding receivers. As the formation grows, the aggregate aperture ap-

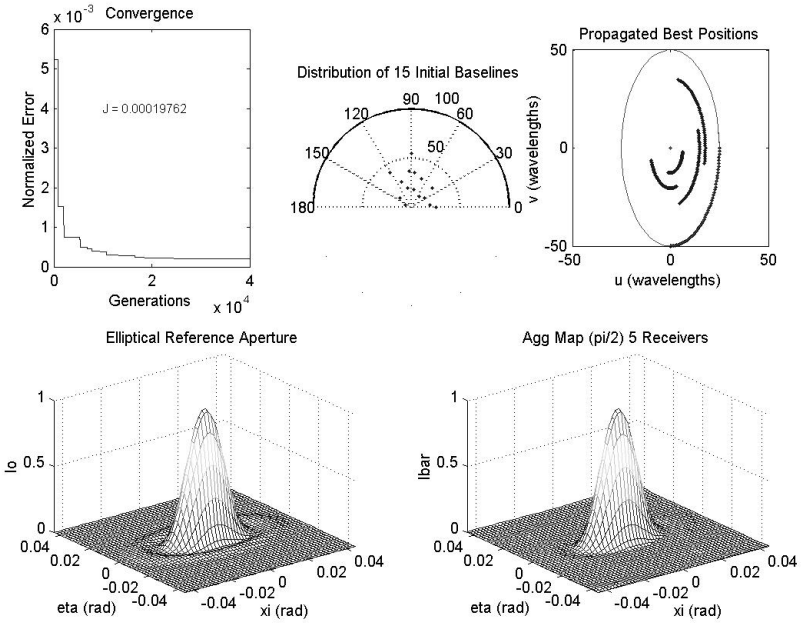

Figure 6.19 A six-receiver formation has ten degrees of freedom. After 40,000 generations, the optimized formation has essentially perfect performance.

proximates the filled reference aperture very closely and this behavior is quantified in the tiny values of the objective function. Expanding the formation out to 7, 9, and 11 receivers yields only marginal improvements in the near-perfect performance, but does require extended numbers of generations for convergence. This outstanding performance will of course be degraded by reducing the target dwell time to less than the idealized 90° of orbit arc.

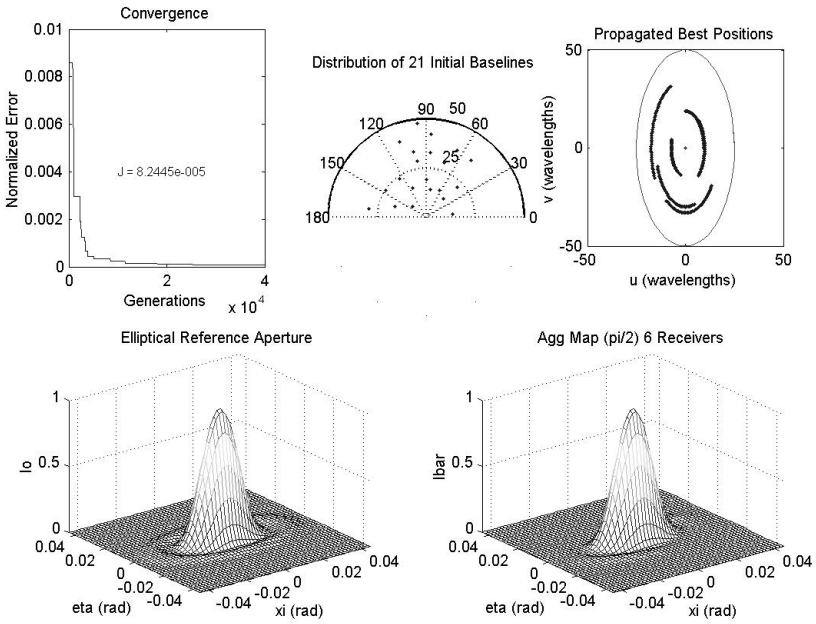

Figure 6.20 A seven-receiver formation has twelve degrees of freedom.

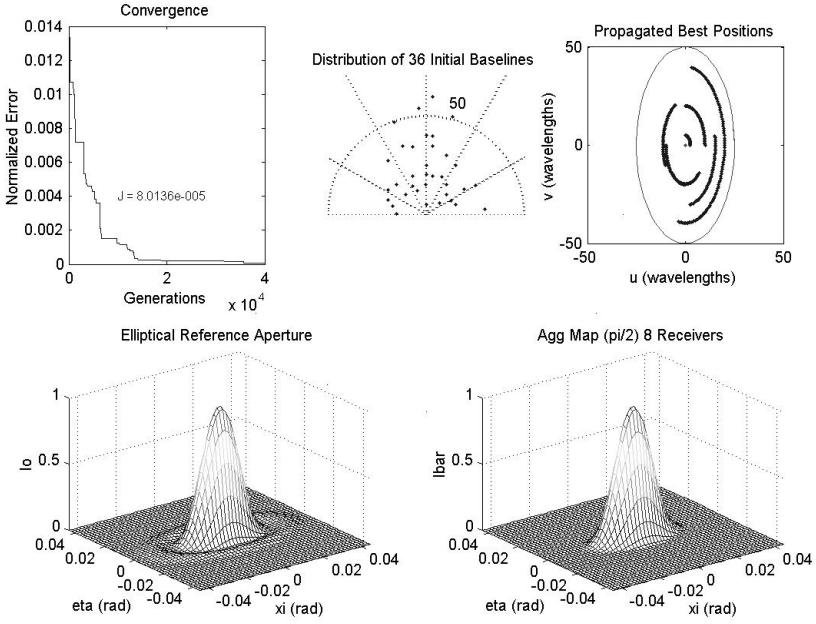

Figure 6.21 A nine-receiver formation has sixteen degrees of freedom.

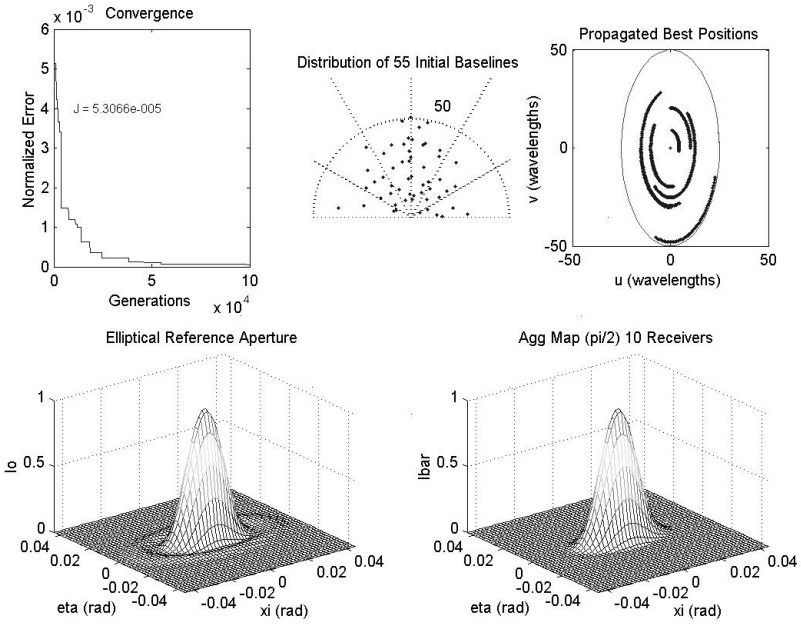

Figure 6.22 An eleven-receiver formation has twenty degrees of freedom (and requires 100,000 generations for adequate convergence). Its overall performance over a 90° sweep is comparable to smaller formations.

Actual computing time for these larger numbers of generations is actually only slightly longer over smaller formations due to the increased infant mortality in new generations. With larger numbers of populations, the early generations have an increased probability that one of its chromosomes will violate the size constraint and be eliminated. This skips initiating a simulation for that prospective member.

Overall the benefits of increasing the formation size results in a diminishing error compared to the filled aperture, figure 6.23. Appendix F has the complete results of optimized formations of three and four receivers.

6.6 Summary

Refining a formation based on an optimization process using the metrics of chapter IV is a non-convex problem. The solutions available are non-unique, and may be determined by employing the global search techniques of genetic algorithms. The numerically derived solutions offer performances that show improvement with both increased reference aperture fidelity and increased formation density. These initial problems were posed with reduced

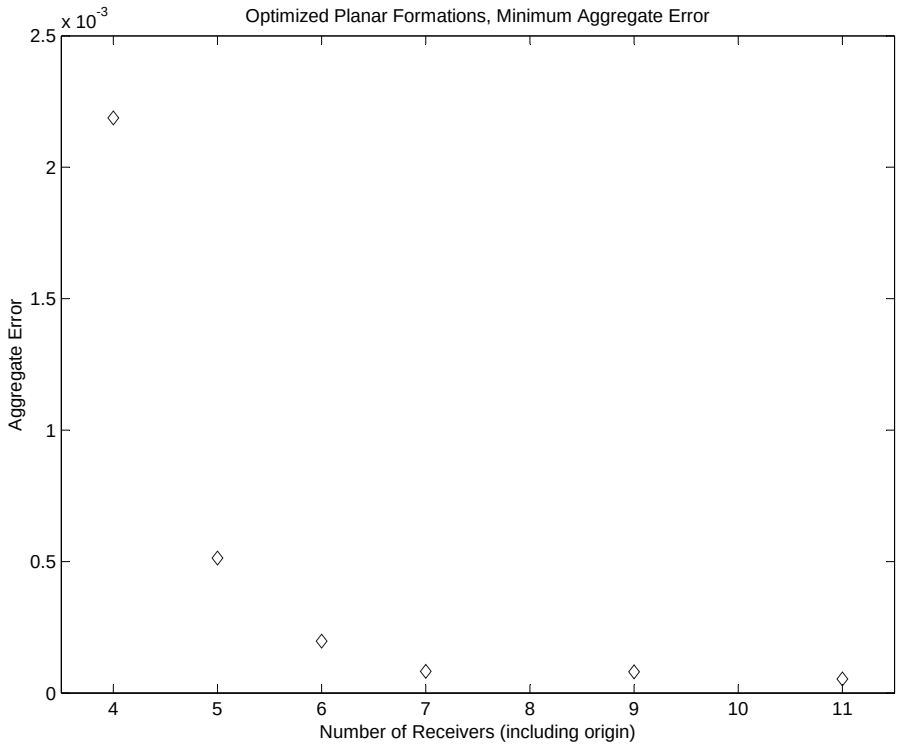

Figure 6.23 Increasing the number of receivers in the formation drives the performance closer to that of the filled aperture, with predictably diminishing improvements with each new receiver.

complexity and dimensionality by assuming ideal viewing geometries (the targets were assumed to be directly normal to the formation planes). This assumption is finally relaxed in the next chapter.

VII. Optimizing for Inertial Targets

With the idealized viewing geometry constructions of the previous chapters in hand, it is possible to extend the solution search to more realistic premises: practical formations and real targets[31]. This chapter defines a notional reference orbit for a formation and locates four example stellar targets. Both the aggregate aperture loci and reference aperture shapes are then warped to model the distortions caused by the non-ideal viewing geometry from each target. A growing series of formations is then re-solved for each target using the genetic algorithm of chapter VI.

7.1 Inertial Targets

Consider a low-flying, high inclination formation, one that offers cheap launch costs and excellent viewing geometries for objects in the vicinity of the celestial equator (and the orbit normal vector)[1].

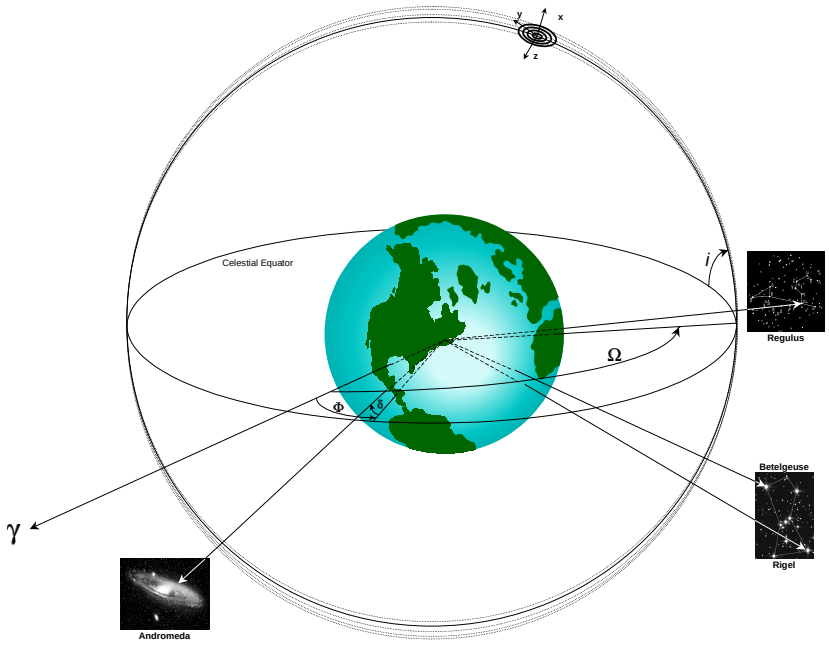

Figure 7.1 A low altitude, high inclination formation offers excellent viewing geometries about the equatorial regions.

[1] Using using short enough wavelengths, such a formation might also be used for viewing high altitude, low inclination Earth-orbiting objects.

For consistency, select a simple low altitude circular orbit inclined at 1 radian, and an ascending node at $\Omega = 150°$. Such an orbit offers relatively simple propagation and good viewing geometry for objects within 90° of the Celestial Origin. Choose to start the imaging arc at an arbitrary true (mean) anomaly of $\nu = 40°$. The main complication in optimizing a formation about such a reference orbit for an actual inertial target is that the assumption of near 90° relative declination is no longer valid. The $(\vec{u}\ \vec{v}\ \vec{w})$ coordinate frame is determined by the target with the $\vec{w}$ axis exactly aligned with the target look vector. The local $(\vec{x}\ \vec{y}\ \vec{z})$ frame is determined by the formation dynamics. Note that the two frames are not aligned. To illustrate the technique required to align the reference frames, it is helpful to have a few example targets.

Celestial objects are located by coordinates of declination δ, and either hour angle, H, or right ascension, Φ. Since Φ is measured eastward from the same reference as the right ascension of the ascending node, Ω, it is the logical choice here over H. Four celestial targets [47], chosen for proximity to the Celestial Equator and brightness are given in table 7.1. The chosen orbit offers good viewing geometry for the "nearby" Andromeda galaxy and the stars Betelgeuse and Rigel, both in the constellation of Orion. Regulus, in the constellation Leo, is deliberately included in this evaluation for its poor viewing geometry.

Object	Right Ascension	Declination
M31 (Andromeda)	10.675°	41.267°
HR2061 (Betelgeuse)	88.793°	7.407°
HR1713 (Rigel)	78.634°	-8.202°
HR3982 (Regulus)	152.093°	11.967°

Table 7.1 Each of these bright celestial objects is located by the coordinates of right ascension, Φ, and declination, δ.

7.2 Orienting the Aggregate Aperture

To map out the effective intensity map generated by the aggregate aperture of a formation, the $\vec{w}$ axis of the spatial frequency coordinate system must be aligned with the direction of the intended target. This carries the minor assumption from chapter IV that the system uses sufficiently long wavelengths that phase may be measured and all

receivers' signals mapped to the same $(\vec{u}\ \vec{v})$ plane. This alignment requires two rotations through the angles δ and Φ, but these angles are in the inertial frame, *not* the non-inertial Clohessy-Wiltshire frame. Therefore the receiver locations in the non-inertial coordinate system must first be mapped out to the inertial system.

$$\begin{bmatrix} \tilde{u} \\ \tilde{v} \\ \tilde{w} \end{bmatrix}_{\star} = \begin{bmatrix} (\vec{x}\ \vec{y}\ \vec{z}) \\ \text{to} \\ (\vec{u}\ \vec{v}\ \vec{w}) \end{bmatrix} \begin{bmatrix} \frac{x}{\lambda} \\ \frac{y}{\lambda} \\ \frac{z}{\lambda} \end{bmatrix} \tag{7.1}$$

This transformation is the reverse of that used by Wiesel [54], summarized in Appendix C, to map an inertial Hamiltonian out to the non-inertial frame. For a distant source, it is *not* necessary to perform the origin translation by $\mathcal{N}_o = (X'_o, Y'_o, Z'_o, P'_{Xo}, P'_{Yo}, P'_{Zo})$.

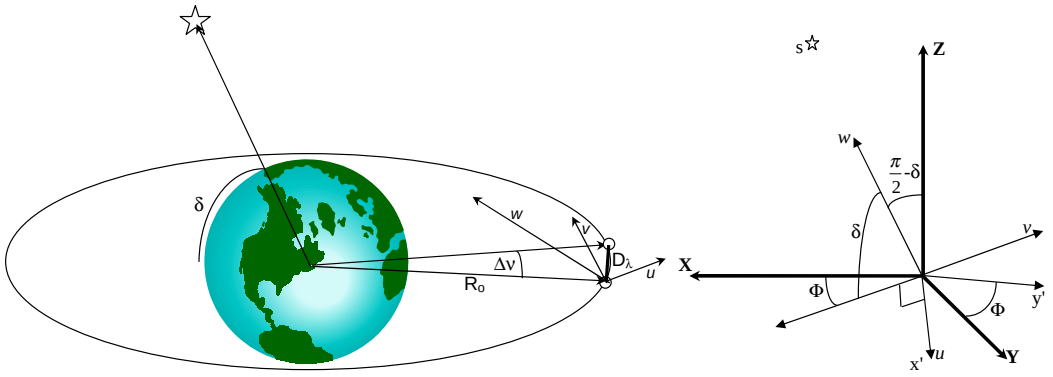

Figure 7.2 A stellar source located at (Φ, δ) determines the orientation of the interferometer coordinate system $(\tilde{\vec{u}}\ \tilde{\vec{v}}\ \tilde{\vec{w}})$. The baselines between each pair of receivers in inertial coordinates can be resolved into this system by two rotations of $\frac{\pi}{2} + \Phi$ and $\frac{\pi}{2} - \delta$.

From figure 7.2, this leaves the rotations of

$$\begin{bmatrix} \tilde{u} \\ \tilde{v} \\ \tilde{w} \end{bmatrix}_{\star} = \begin{bmatrix} \text{rotation of } \frac{\pi}{2} - \delta \\ \text{about } \hat{X}' \end{bmatrix} \begin{bmatrix} \text{rotation of } \frac{\pi}{2} + \Phi \\ \text{about } \hat{Z} \end{bmatrix} \mathcal{R}_Z^T \mathcal{R}^T \begin{bmatrix} \frac{x}{\lambda} \\ \frac{y}{\lambda} \\ \frac{z}{\lambda} \end{bmatrix}. \tag{7.2}$$

See Appendix C for general definitions of the inertial to nodal frame rotation matrix, $\mathcal{R}_Z$ (ignoring $\dot{\Omega}$ for the short duration dwell time), and the nodal to local C-W frame rotation matrix, $\mathcal{R}$. Setting up the inertial rotations[2] and inserting the rotations from the Clohessy-Wiltshire frame gives

$$\begin{bmatrix} \tilde{u} \\ \tilde{v} \\ \tilde{w} \end{bmatrix}_\star = \begin{bmatrix} 1 & 0 & 0 \\ 0 & \cos(\frac{\pi}{2}-\delta) & \sin(\frac{\pi}{2}-\delta) \\ 0 & -\sin(\frac{\pi}{2}-\delta) & \cos(\frac{\pi}{2}-\delta) \end{bmatrix} \begin{bmatrix} \cos(\frac{\pi}{2}+\Phi) & \sin(\frac{\pi}{2}+\Phi) & 0 \\ -\sin(\frac{\pi}{2}+\Phi) & \cos(\frac{\pi}{2}+\Phi) & 0 \\ 0 & 0 & 1 \end{bmatrix} \mathcal{R}_Z^T \mathcal{R}^T \begin{bmatrix} \frac{x}{\lambda} \\ \frac{y}{\lambda} \\ \frac{z}{\lambda} \end{bmatrix}. \tag{7.3}$$

Simplifying,

$$\begin{bmatrix} \tilde{u} \\ \tilde{v} \\ \tilde{w} \end{bmatrix}_\star = \begin{bmatrix} 1 & 0 & 0 \\ 0 & \sin\delta & \cos\delta \\ 0 & -\cos\delta & \sin\delta \end{bmatrix} \begin{bmatrix} -\sin\Phi & \cos\Phi & 0 \\ -\cos\Phi & -\sin\Phi & 0 \\ 0 & 0 & 1 \end{bmatrix} \mathcal{R}_Z^T \mathcal{R}^T \begin{bmatrix} \frac{x}{\lambda} \\ \frac{y}{\lambda} \\ \frac{z}{\lambda} \end{bmatrix}. \tag{7.4}$$

This adjusts vectors in the local $(\vec{x}\ \vec{y}\ \vec{z})$ system to be remapped to the $(\tilde{\vec{u}}\ \tilde{\vec{v}}\ \tilde{\vec{w}})$ axes, an inertial frame for an inertial target. Using the simple geometry of figure 7.1, $\mathcal{R}_Z$ and $\mathcal{R}$ may be constructed explicitly in terms of the Keplerian elements of the reference orbit.

$$\begin{aligned} \begin{bmatrix} \tilde{u} \\ \tilde{v} \\ \tilde{w} \end{bmatrix}_\star = \begin{bmatrix} 1 & 0 & 0 \\ 0 & \sin\delta & \cos\delta \\ 0 & -\cos\delta & \sin\delta \end{bmatrix} \begin{bmatrix} -\sin\Phi & \cos\Phi & 0 \\ -\cos\Phi & -\sin\Phi & 0 \\ 0 & 0 & 1 \end{bmatrix} \begin{bmatrix} \cos\Omega & \sin\Omega & 0 \\ -\sin\Omega & \cos\Omega & 0 \\ 0 & 0 & 1 \end{bmatrix}^T \cdots \\ \cdots \begin{bmatrix} 1 & 0 & 0 \\ 0 & \cos i & \sin i \\ 0 & -\sin i & \cos i \end{bmatrix}^T \begin{bmatrix} \cos\nu & \sin\nu & 0 \\ -\sin\nu & \cos\nu & 0 \\ 0 & 0 & 1 \end{bmatrix}^T \begin{bmatrix} \frac{x}{\lambda} \\ \frac{y}{\lambda} \\ \frac{z}{\lambda} \end{bmatrix} \end{aligned} \tag{7.5}$$

Simplifying,

[2] Thompson [46] gives a related formulation of these rotations to translate stellar coordinates to a *terrestrial* interferometer frame. These may be applied to the relative coordinates of a formation provided they are preceded by the $\mathcal{R}_Z^T \mathcal{R}^T$ rotations.

$$\begin{bmatrix} \tilde{u} \\ \tilde{v} \\ \tilde{w} \end{bmatrix}_\star = \begin{bmatrix} 1 & 0 & 0 \\ 0 & \sin\delta & \cos\delta \\ 0 & -\cos\delta & \sin\delta \end{bmatrix} \begin{bmatrix} \cos(\frac{\pi}{2}+\Phi-\Omega) & \sin(\frac{\pi}{2}+\Phi-\Omega) & 0 \\ -\sin(\frac{\pi}{2}+\Phi-\Omega) & \cos(\frac{\pi}{2}+\Phi-\Omega) & 0 \\ 0 & 0 & 1 \end{bmatrix} \cdots \\ \cdots \begin{bmatrix} 1 & 0 & 0 \\ 0 & \cos i & \sin i \\ 0 & -\sin i & \cos i \end{bmatrix}^T \begin{bmatrix} \cos\nu & \sin\nu & 0 \\ -\sin\nu & \cos\nu & 0 \\ 0 & 0 & 1 \end{bmatrix}^T \begin{bmatrix} \frac{x}{\lambda} \\ \frac{y}{\lambda} \\ \frac{z}{\lambda} \end{bmatrix} \tag{7.6}$$

Aligning the local coordinate system with the look vector to a stellar target has the effect of projecting the elliptical formation onto the plane orthogonal to the look vector. This skews the perfect elliptical loci of the formation paths, figure 7.3. With the propagated

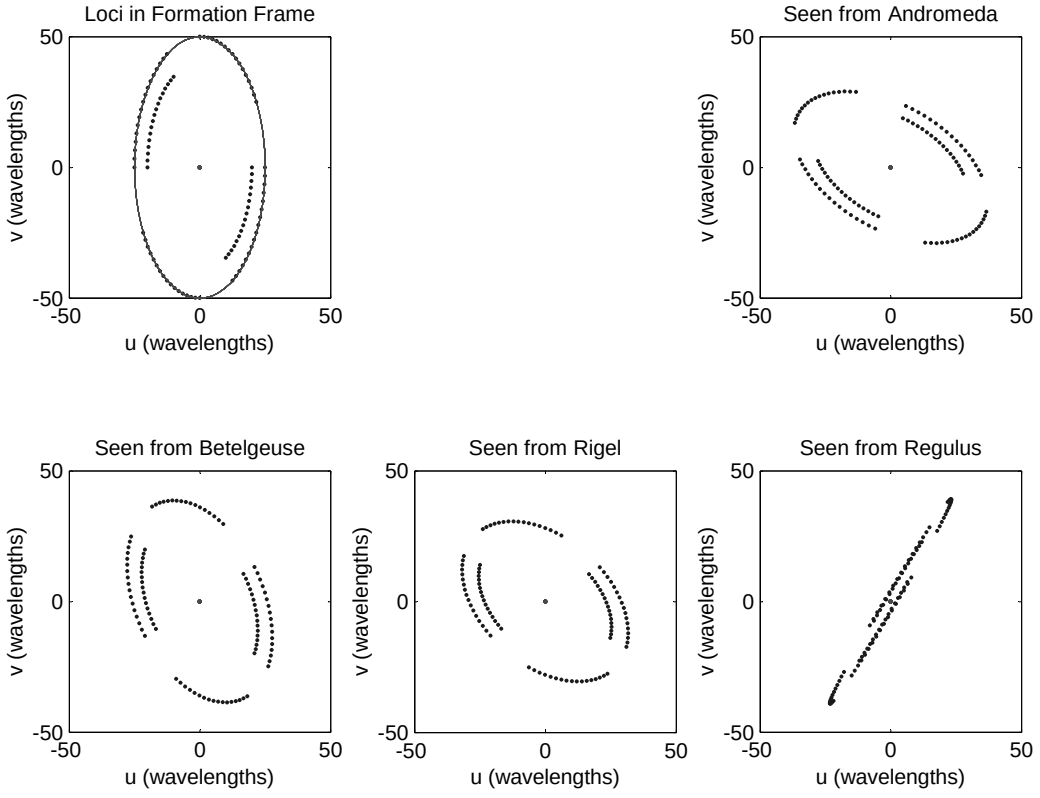

Figure 7.3 Moving the viewer's vantage point over to the look vector from each of the four stellar targets demonstrates how the formation loci appear skewed when viewed from a source not directly above the formation.

receiver locations mapped to the inertial $(\tilde{\vec{u}}\ \tilde{\vec{v}})$ frame, the aggregate aperture may be

synthesized using the same permutations developed in equation 4.12 and intensity map of equation 4.13.

7.3 Orienting the Reference Aperture

The mapping of equation 7.6 gives the appropriate length and orientation for each individual baseline used to build the aggregate aperture intensity, $\overline{\mathbf{I_P}}(\xi, \eta, t)$, but the reference intensity map, $\mathbf{I_o}(\xi, \eta)$, must also be altered to reflect the true relative geometry. Otherwise the optimization is hampered by seeking loci where the formation dynamics do not allow them. This alteration may be accomplished by generalizing the derivation of equation 5.23.

Consider the basic polar and rectangular representations of the **PSF** from equations 5.18,

$$\mathbf{PSF}_{\text{ellipse}}(r, \theta, \rho') = e^{2i\pi\rho'(r\cos(\theta))} \tag{7.7a}$$

$$\mathbf{PSF}_{\text{ellipse}}(u, v, \xi, \eta) = e^{2i\pi(\frac{b}{a}u\xi + v\eta)} \tag{7.7b}$$

which allowed the intensity map symmetric in θ to be skewed in the spatial domain image plane by defining the eccentric radius, ρ', generated by adjusting its components' rectangular coordinates

$$\rho' = \sqrt{\left(\frac{b}{a}\xi\right)^2 + (\eta)^2}. \tag{7.8}$$

An elliptical aperture, viewed from a direction off-normal to the relative orbit plane will have some further distortion of its apparent shape. Generalizing the technique used in section 5.2.3, this shape may be determined in the spatial frequency domain and transferred through the **PSF** to define a *warped* eccentric radius, ρ'', in the spatial domain. Each of the rectangular components of the spatial frequency radius may be stretched or contracted individually by some coefficient to give the warped eccentric radius, r''. Initially assume they are independent and define them generically as ϕ in the $\vec{u}$ direction, and ψ in the $\vec{v}$ direction. Obviously each will be some function of the rotations from the reference orbit

to the target location.

$$\begin{aligned} \phi &= f_1(i, \Omega, \nu, \ \Phi, \delta) \\ \psi &= f_2(i, \Omega, \nu, \ \Phi, \delta) \end{aligned}$$

These may be incorporated into the definition of the warped eccentric radius as shown in figure 7.4. This warped ellipse may be modelled as the *projection* of each transformed

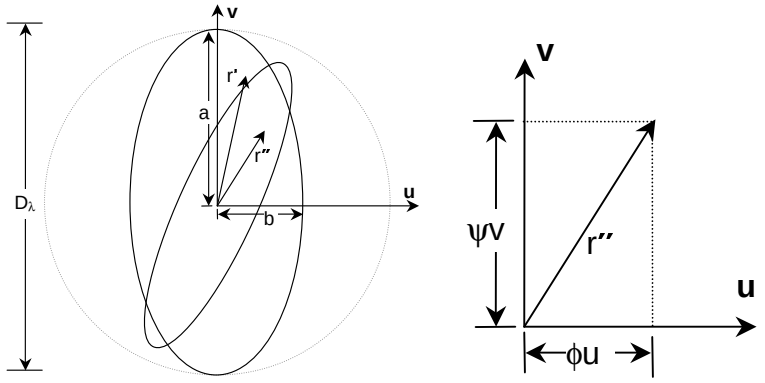

Figure 7.4 The elliptical aperture's relative coordinate system representation is distorted when viewed from the look angles (Φ, δ) to the target. The distorted ellipse may be generated by rotations through Φ, δ, and the reference orbit orientation angles ν, i, and Ω.

radius onto the inertial $(\tilde{\vec{u}}\ \tilde{\vec{v}})$ plane. Using the rotations of equation 7.6 the generalized $\mathbf{PSF}_{\text{ellipse}\star}$ for the image plane coordinates may be built.

$$\mathbf{PSF}_{\text{ellipse}\star}(\tilde{u}, \tilde{v}, \xi, \eta) = e^{2i\pi(\tilde{u}\xi + \tilde{v}\eta)} \tag{7.10a}$$

$$\mathbf{PSF}_{\text{ellipse}\star}(\tilde{u}, \tilde{v}, \xi, \eta) = e^{2i\pi \left(\begin{bmatrix} \xi & \eta & 0 \end{bmatrix} \begin{bmatrix} \tilde{u} \\ \tilde{v} \\ \tilde{w} \end{bmatrix} \right)} \tag{7.10b}$$

For shorthand, abbreviate the rotation matrices from equation 7.6 as $\begin{bmatrix} \delta_x \end{bmatrix}$, $\begin{bmatrix} \left(\frac{\pi}{2} + \Phi - \Omega\right)_z \end{bmatrix}$, $\begin{bmatrix} i_x \end{bmatrix}^T$, and $\begin{bmatrix} \nu_z \end{bmatrix}^T$. Inserting these and the contraction of $\frac{b}{a}$ into the **PSF** for $[\tilde{u}\ \ \tilde{v}\ \ \tilde{w}]^T$ yields

$$\mathbf{PSF}_{\text{ellipse}\star}(\tilde{u},\tilde{v},\xi,\eta) = e^{2i\pi\left(\begin{bmatrix} \xi & \eta & 0 \end{bmatrix}\begin{bmatrix} \delta_x \end{bmatrix}\begin{bmatrix} \left(\frac{\pi}{2}+\Phi-\Omega\right)_z \end{bmatrix}\begin{bmatrix} i_x \end{bmatrix}^T\begin{bmatrix} \nu_z \end{bmatrix}^T\begin{bmatrix} \frac{b}{a} & 0 & 0 \\ 0 & 1 & 0 \\ 0 & 0 & 1 \end{bmatrix}\begin{bmatrix} \frac{x}{\lambda} \\ \frac{y}{\lambda} \\ \frac{z}{\lambda} \end{bmatrix}\right)}$$

$$\mathbf{PSF}_{\text{ellipse}\star}(u,v,\tilde{\xi},\tilde{\eta}) = e^{2i\pi\left(\begin{bmatrix} \tilde{\xi} & \tilde{\eta} & 0 \end{bmatrix}_\star\begin{bmatrix} \frac{x}{\lambda} \\ \frac{y}{\lambda} \\ \frac{z}{\lambda} \end{bmatrix}\right)} \tag{7.11}$$

where the warped spatial coordinates $(\tilde{\xi},\tilde{\eta})_\star$ are defined by transferring the rotations from the spatial frequency domain to the spatial domain.

$$\begin{bmatrix} \tilde{\xi} & \tilde{\eta} & 0 \end{bmatrix}_\star = \begin{bmatrix} \xi & \eta & 0 \end{bmatrix}\begin{bmatrix} \delta_x \end{bmatrix}\begin{bmatrix} \left(\frac{\pi}{2}+\Phi-\Omega\right)_z \end{bmatrix}\begin{bmatrix} i_x \end{bmatrix}^T\begin{bmatrix} \nu_z \end{bmatrix}^T\begin{bmatrix} \frac{b}{a} & 0 & 0 \\ 0 & 1 & 0 \\ 0 & 0 & 1 \end{bmatrix} \tag{7.12}$$

The **PSF** may now be expressed in its polar form in terms of the warped eccentric radius, ρ'' as

$$\mathbf{PSF}_{\text{ellipse}\star}(r,\theta,\rho'') = e^{2i\pi\rho''(r\cos\theta)}. \tag{7.13}$$

This is the same form of the **PSF** as equation 5.18, with the additional distortions all contained in the formulation of ρ'', warping the symmetric (in θ) output. Therefore ρ'' may be formally defined

$$\rho'' = \sqrt{\begin{bmatrix} \tilde{\xi} & \tilde{\eta} & 0 \end{bmatrix}_\star\begin{bmatrix} \tilde{\xi} \\ \tilde{\eta} \\ 0 \end{bmatrix}_\star}. \tag{7.14}$$

By setting the third element of $\begin{bmatrix} \tilde{\xi} & \tilde{\eta} & 0 \end{bmatrix}_\star$ to zero, ρ'' warps the known output of a filled planar circular spatial frequency aperture, and generates its *projection* onto the spatial $(\tilde{\xi},\tilde{\eta})_\star$ image plane. Expanding the terms in ρ'' and using $\|\cdot\|_2$ for the vector magnitude allows

$$\rho'' = \left\| \begin{bmatrix} \xi & \eta \end{bmatrix} \left(\begin{bmatrix} \delta_x \end{bmatrix} \begin{bmatrix} \left(\frac{\pi}{2} + \Phi - \Omega\right)_z \end{bmatrix} \begin{bmatrix} i_x \end{bmatrix}^T \begin{bmatrix} \nu_z \end{bmatrix}^T \begin{bmatrix} \frac{b}{a} & 0 & 0 \\ 0 & 1 & 0 \\ 0 & 0 & 1 \end{bmatrix} \right)_{2\times 2} \right\|_2 , \quad (7.15)$$

where the subscript 2×2 indicates just the upper left four elements of the rotation matrix[3]. For compactness, define the series of rotations as the matrix $\mathcal{W}$

$$\mathcal{W} = \begin{bmatrix} 1 & 0 & 0 \\ 0 & \sin\delta & \cos\delta \\ 0 & -\cos\delta & \sin\delta \end{bmatrix} \begin{bmatrix} \cos(\frac{\pi}{2}+\Phi-\Omega) & \sin(\frac{\pi}{2}+\Phi-\Omega) & 0 \\ -\sin(\frac{\pi}{2}+\Phi-\Omega) & \cos(\frac{\pi}{2}+\Phi-\Omega) & 0 \\ 0 & 0 & 1 \end{bmatrix} \begin{bmatrix} 1 & 0 & 0 \\ 0 & \cos i & \sin i \\ 0 & -\sin i & \cos i \end{bmatrix}^T \begin{bmatrix} \cos\nu & \sin\nu & 0 \\ -\sin\nu & \cos\nu & 0 \\ 0 & 0 & 1 \end{bmatrix}^T \begin{bmatrix} \frac{b}{a} & 0 & 0 \\ 0 & 1 & 0 \\ 0 & 0 & 1 \end{bmatrix} . \quad (7.16)$$

Extract only the projection of the image intensity map onto the $(\tilde{\xi}, \tilde{\eta})_\star$ plane by pulling out the upper left 2×2 portion of $\mathcal{W}$ to define $\mathcal{W}_\star$.

$$\mathcal{W}_\star = \begin{bmatrix} 1 & 0 & 0 \\ 0 & 1 & 0 \end{bmatrix} \begin{bmatrix} & \mathcal{W} & \end{bmatrix} \begin{bmatrix} 1 & 0 \\ 0 & 1 \\ 0 & 0 \end{bmatrix}$$

$$\begin{aligned}
\mathcal{W}_\star(1,1) &= \left(\tfrac{b}{a}\right)\left\{\cos\left(\tfrac{\pi}{2}+\Phi-\Omega\right)\cos\nu + \sin\left(\tfrac{\pi}{2}+\Phi-\Omega\right)\cos i\sin\nu\right\} \\
\mathcal{W}_\star(1,2) &= -\cos\left(\tfrac{\pi}{2}+\Phi-\Omega\right)\sin\nu + \sin\left(\tfrac{\pi}{2}+\Phi-\Omega\right)\cos i\cos\nu \\
\mathcal{W}_\star(2,1) &= \left(\tfrac{b}{a}\right)\left\{-\sin\delta\sin\left(\tfrac{\pi}{2}+\Phi-\Omega\right)\cos\nu + \sin\nu\left(\sin\delta\cos\left(\tfrac{\pi}{2}+\Phi-\Omega\right)\cos i + \cos\delta\sin i\right)\right\} \\
\mathcal{W}_\star(2,2) &= \sin\delta\sin\left(\tfrac{\pi}{2}+\Phi-\Omega\right)\sin\nu + \cos\nu\left(\sin\delta\cos\left(\tfrac{\pi}{2}+\Phi-\Omega\right)\cos i + \cos\delta\sin i\right)
\end{aligned} \quad (7.17)$$

[3]Since the full 3×3 rotation matrix is full rank, using the full matrix multiplied by $\begin{bmatrix} \xi & \eta & 0 \end{bmatrix}$ keeps the $\vec{w}$ components. This does not *project* the radius onto the $(\tilde{\xi}, \tilde{\eta})_\star$ plane with the resulting contractions, but preserves the original magnitude. Using the 2×2 upper left portion generates this projection.

Now equation 5.23 may finally be brought forward and generalized by direct substitution of ρ'' for ρ', to give $\mathbf{I_o}(\xi,\eta)_\star$ as

$$\mathbf{I_o}(\xi,\eta)_\star = \left[\frac{2J_1\left(D_\lambda \pi \left\| \mathcal{W}_\star^T \begin{bmatrix} \xi \\ \eta \end{bmatrix} \right\|_2 \right)}{D_\lambda \pi \left\| \mathcal{W}_\star^T \begin{bmatrix} \xi \\ \eta \end{bmatrix} \right\|_2} \right]^2 \tag{7.18}$$

This describes the intensity map generated by an aperture of elliptical shape, following a reference orbit with initial true anomaly, inclination, and right ascension of the ascending node of (ν, i, Ω), as viewed from an inertial source at right ascension and declination (Φ, δ).

7.4 Viewing Geometry Effects on $\mathbf{I_o}(\xi,\eta)$

Inspection of the upper left 2×2 of each rotation in $\mathcal{W}$ reveals the effects of each on $(\tilde{\xi},\tilde{\eta})_\star$. Rotations through ν reorient the formation, but do nothing to change its size, since

$$\det\left(\begin{bmatrix} \cos\nu & \sin\nu \\ -\sin\nu & \cos\nu \end{bmatrix}^T \right) = 1. \tag{7.19}$$

The formation's apparent size *is* affected by rotating through the inclination and declination. The net effect of each is influenced by the difference in right ascension, $(\frac{\pi}{2} + \Phi - \Omega)$, "sandwiched" between them, since

$$\det\left\{ \left(\begin{bmatrix} 1 & 0 & 0 \\ 0 & \sin\delta & \cos\delta \\ 0 & -\cos\delta & \sin\delta \end{bmatrix} \begin{bmatrix} \cos(\frac{\pi}{2}+\Phi-\Omega) & \sin(\frac{\pi}{2}+\Phi-\Omega) & 0 \\ -\sin(\frac{\pi}{2}+\Phi-\Omega) & \cos(\frac{\pi}{2}+\Phi-\Omega) & 0 \\ 0 & 0 & 1 \end{bmatrix} \begin{bmatrix} 1 & 0 & 0 \\ 0 & \cos i & \sin i \\ 0 & -\cos i & \sin i \end{bmatrix}^T \right)_{2\times 2} \right\} \leq 1. \tag{7.20}$$

The effects of each rotation in the sequence of equation 7.6 on the apparent size and shape of a formation are graphically depicted in figure 7.5. The effect of each rotation on the intensity map is predictable. Simple rotations in the aperture rotate the reference intensity map. A decrease in aperture size along any axis causes an expansion of the reference intensity map along the axis perpendicular to the change, figure 7.6.

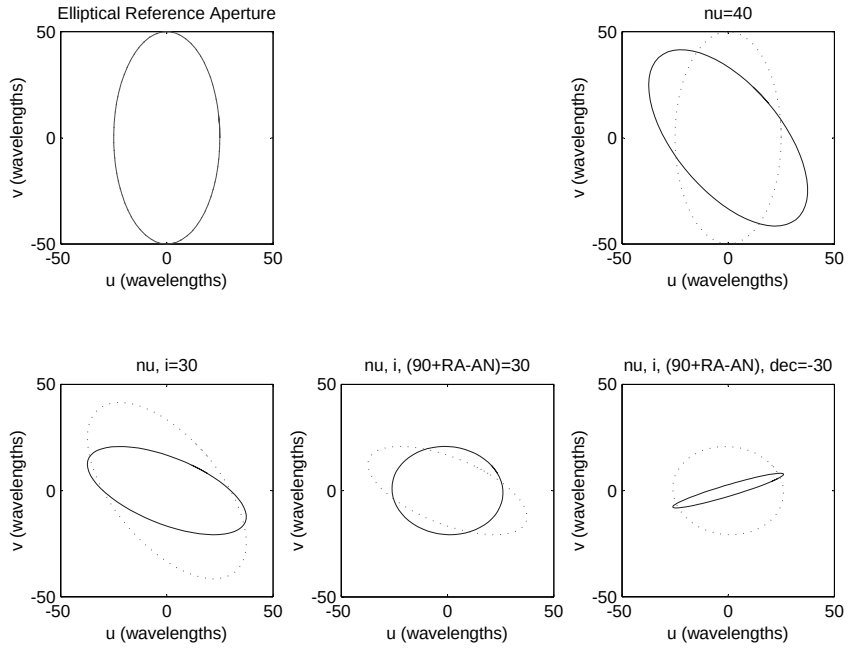

Figure 7.5 To exaggerate the effects of each rotation, consider a formation at $\nu = 40°$, $i = 30°$, and $\Omega = 90°$ rotated to view a notional star at $\Phi = 30°$ and $\delta = -30°$.

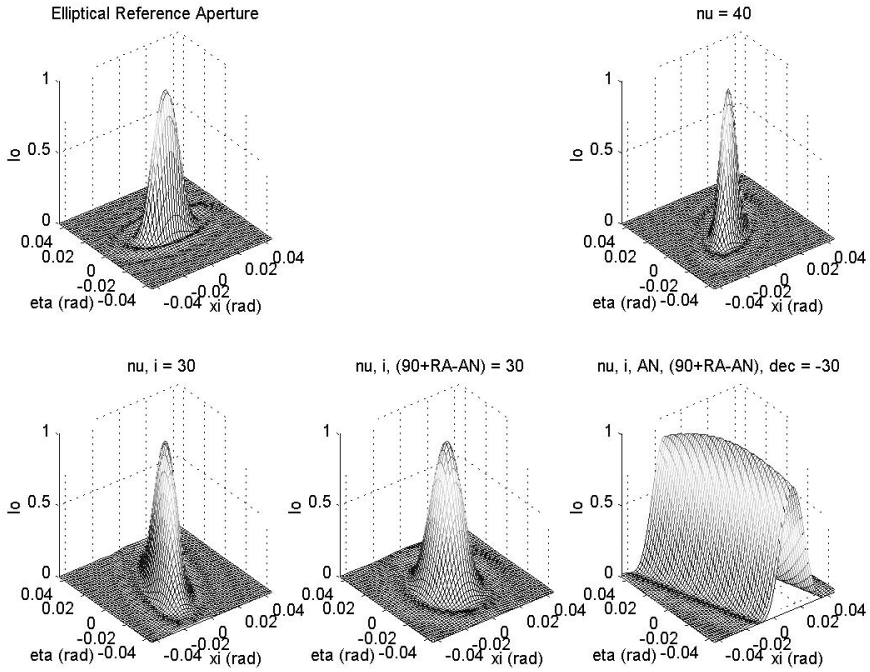

Figure 7.6 As the elliptical aperture is rotated and contracted, the effective intensity map is directly affected.

Performing the actual $\mathcal{W}_\star$ rotations for Andromeda and Regulus, figure 7.7,

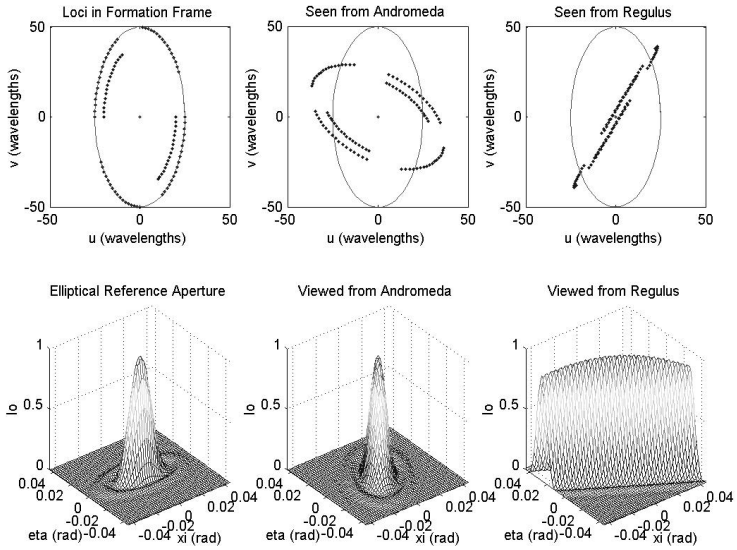

Figure 7.7 Aligning the $\vec{w}$ axis of the filled reference aperture with the look angle to the inertial target necessarily warps the regular filled elliptical aperture map. Andromeda is less than 50° off of the centerline of the formation, and with $\nu = 40°$ the contraction is actually seen mostly in the formation's major axis. Regulus is actually 92° away from the centerline (truly awful geometry).

and the two stars in Orion, figure 7.8, show the practical applications of equation 7.18.

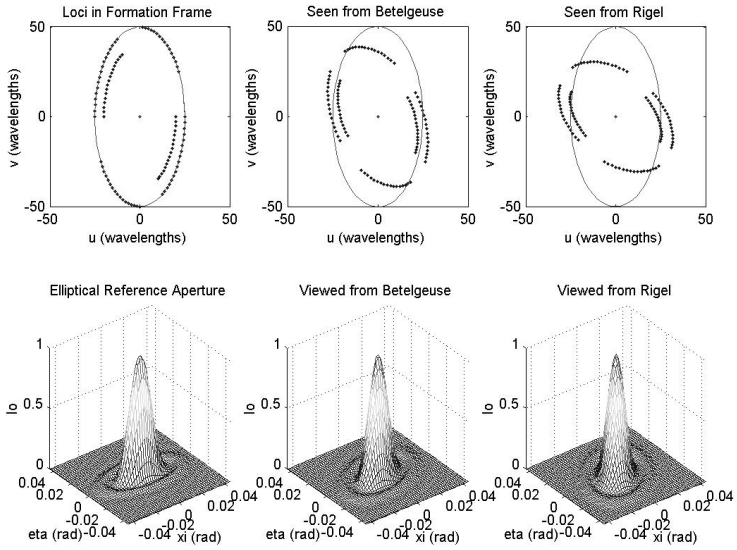

Figure 7.8 Both Betelgeuse and Rigel are less than 30° off of the center axis of the formation. Rigel lies below the Celestial Equator, and shows a greater contraction of the effective aperture size (wider peak in $\mathbf{I_o}(\xi, \eta)_{\text{Rigel}}$).

7.5 Optimized Formations for Inertial Targets

A simple planar formation allows the optimization to select a set of formation slopes, m_H and n_H used for all receivers, and both a ρ_H and θ_H for each receiver except for the one at the origin. This results in a problem with $(\text{Receivers}-1)\times 2+2$ degrees of freedom. Starting with a five receiver formation, four receivers must be placed to provide a set of ten baselines. Optimizing such a formation to view Andromeda is shown in figure 7.9.

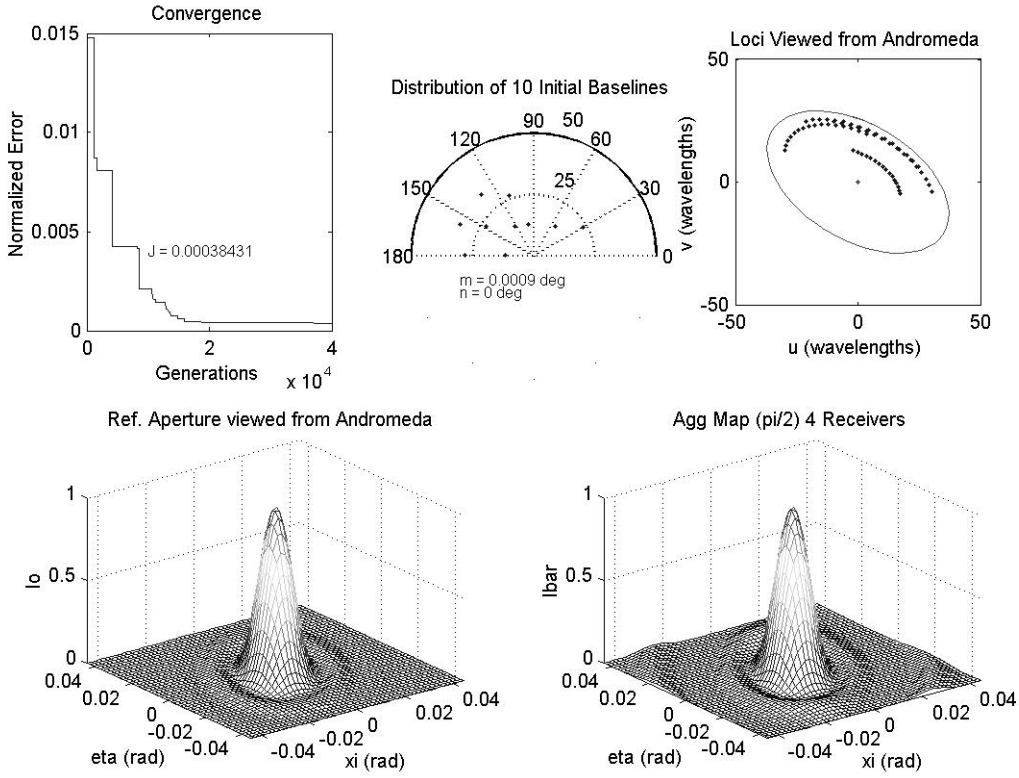

Figure 7.9 Andromeda is only slightly off of the formation centerline, so the reference aperture's size is only slightly contracted. The initial ν of the formation has the greatest effect on the reference aperture by rotating it.

Keeping the same formation, but optimizing for Betelgeuse, Rigel, and Regulus uses the same solution technique, with reference apertures adjusted for each target, figures 7.10, 7.11, and 7.12.

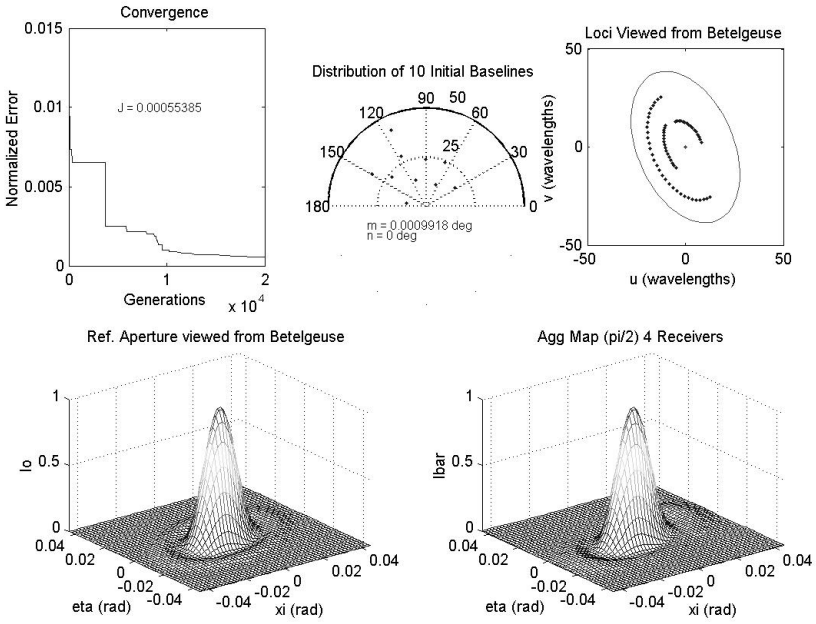

Figure 7.10 Betelgeuse also has excellent viewing geometry from the example formation, showing only a slight rotation and contraction in the reference aperture.

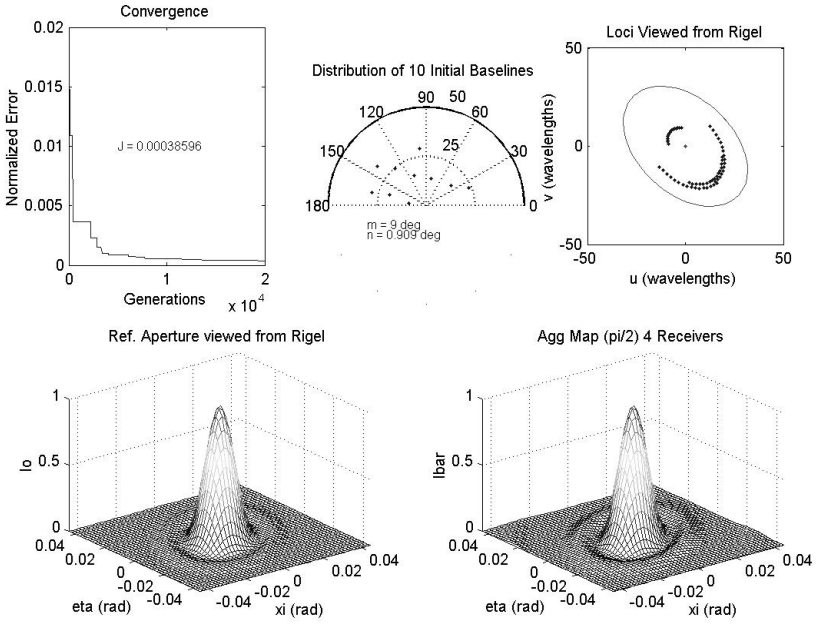

Figure 7.11 Rigel has fairly good viewing geometry from the formation. Note how the optimized formation has been tilted with an $m_H = 9°$.

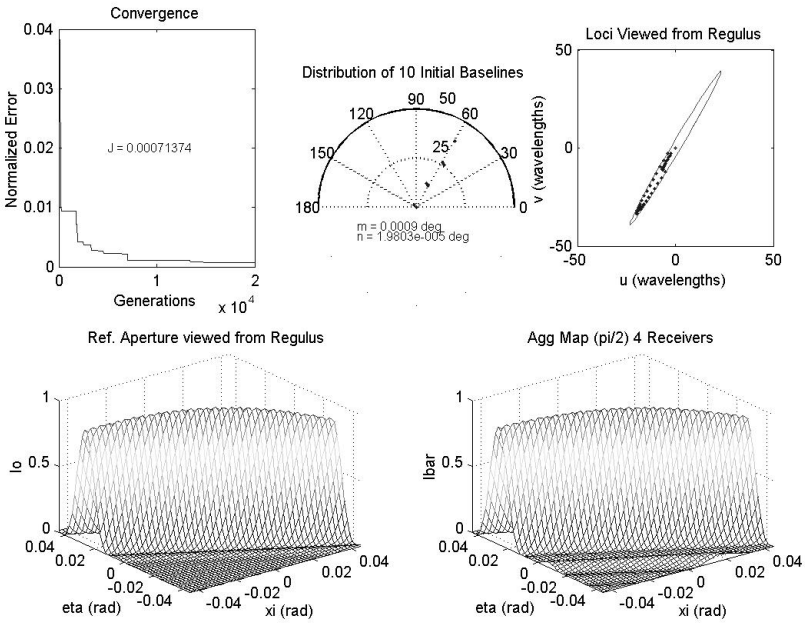

Figure 7.12 The poor viewing geometry for Regulus is apparent both in its reference aperture and the selection of initial baseline orientations. Note that $\mathbf{J}_{\text{image}}$ is still quite small, indicating the formation is being compared to an appropriate reference aperture.

Adding another receiver simply adds two more degrees of freedom to the problem. Predictably, the formations not only mimic the filled apertures better with more receivers, but the $\mathbf{J}_{\text{image}}$ function is decidedly smaller for each final formation (again suggesting the optimization is comparing appropriate maps), figures 7.13 through 7.16.

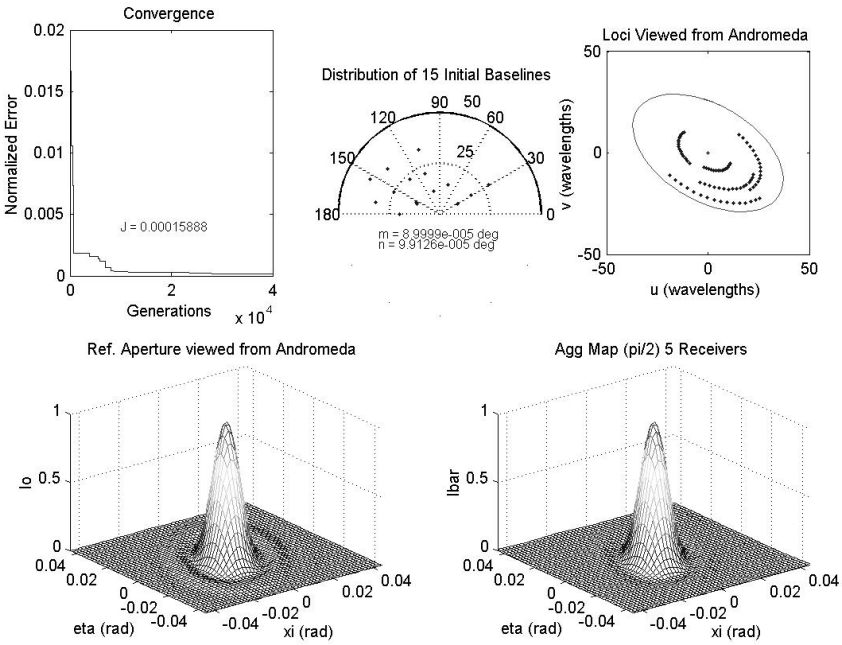

Figure 7.13 Optimizing about the same reference orbit with six receivers for Andromeda is a 12 degree of freedom problem.

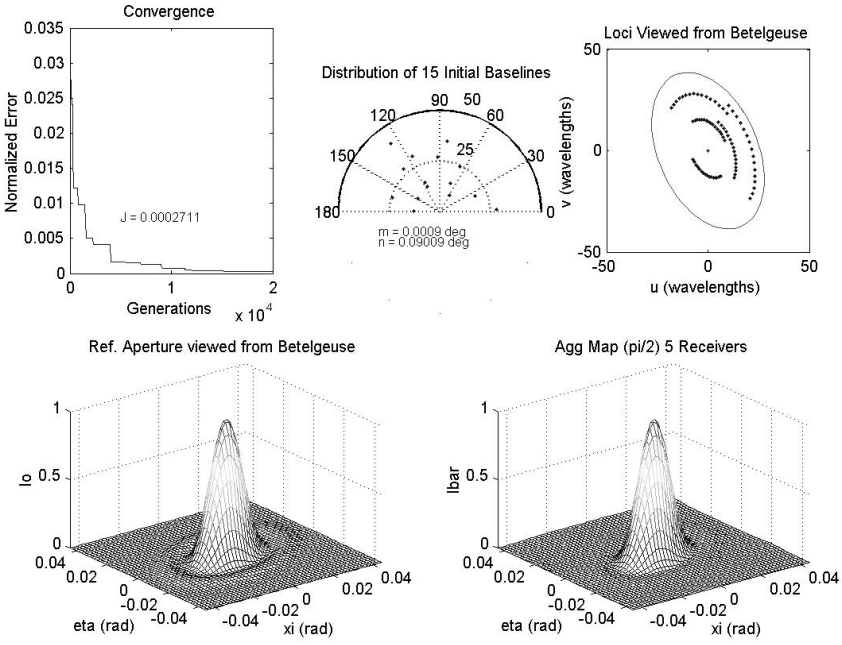

Figure 7.14 This is the same six-receiver (five movable) formation optimized for Betelgeuse.

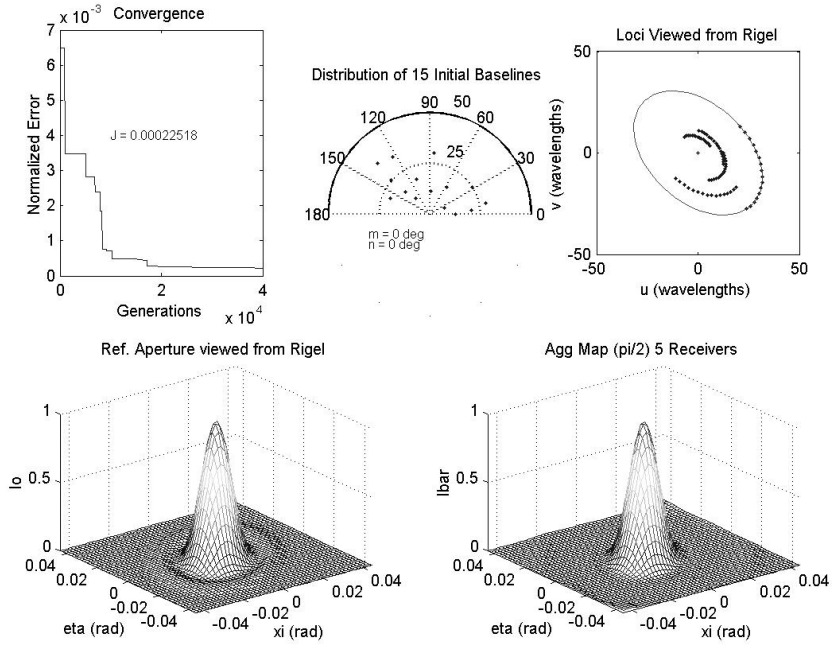

Figure 7.15 This is the same six-receiver (five movable) formation optimized for Rigel.

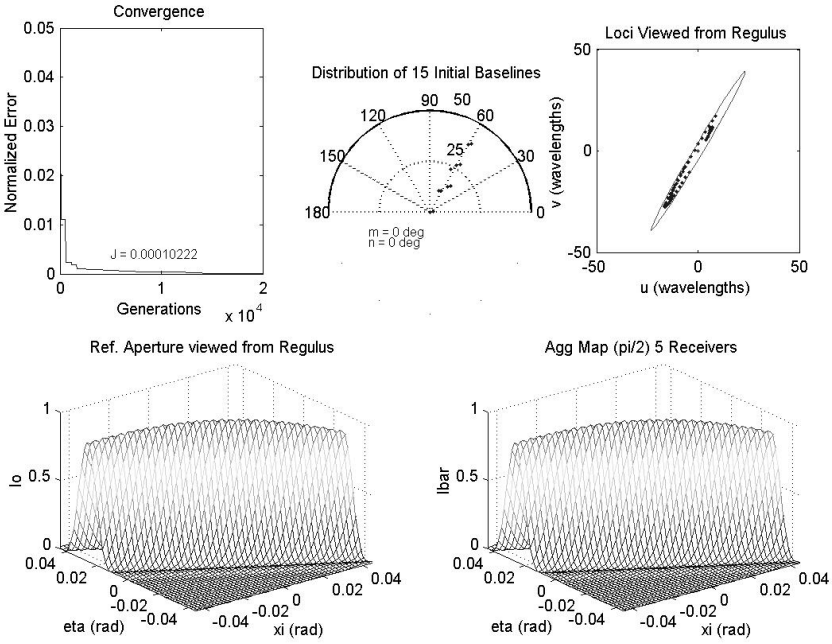

Figure 7.16 This is the same six-receiver formation optimized for Regulus. Even with its atrocious geometry, the optimization works well to yield low values of $\mathbf{J}_{\text{image}}$.

Further optimization problems for larger formations of 7, 9, and 11 receivers are included in appendix F. All show the same trend as the idealized planar formation built at the end of chapter VI. Increasing the number of elements, N, in the formations yields higher fidelity synthesis of the filled aperture performance, but with diminishing returns as N is increased.

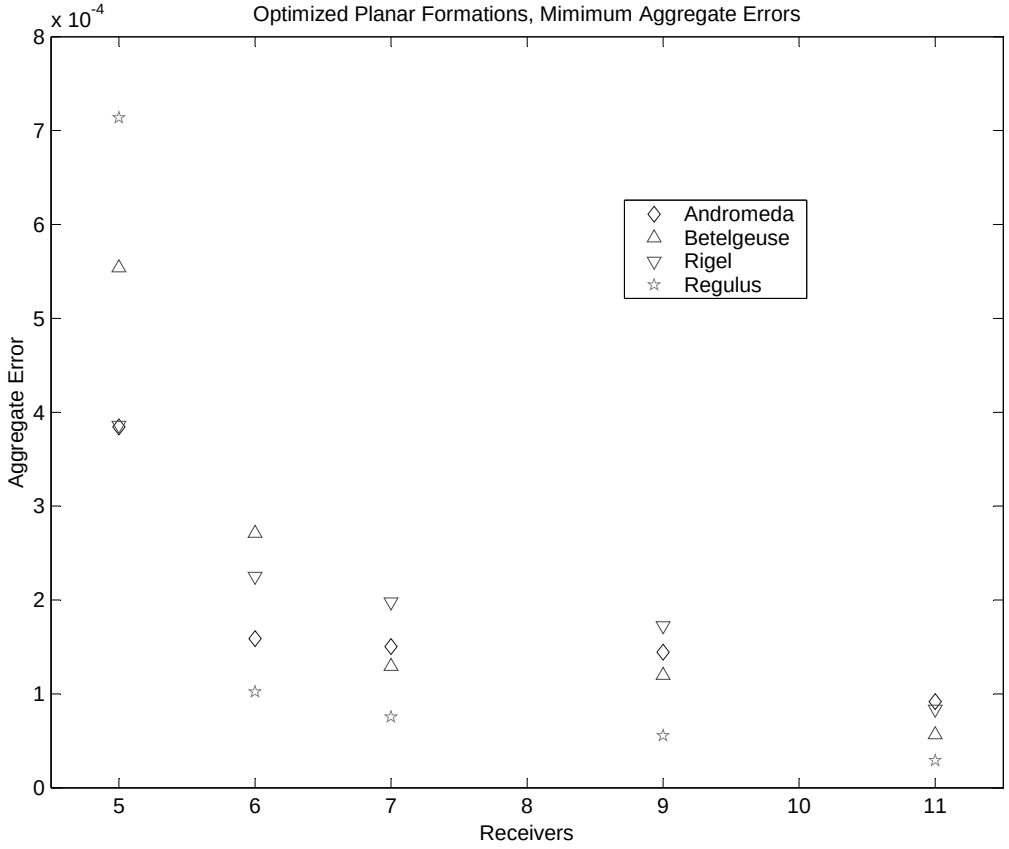

Figure 7.17 As the formation is enlarged, its ability to synthesize the output of a filled aperture increases. The aggregate error as compared to each's filled aperture decreases.

7.6 Summary

This chapter expanded the models embedded in the metrics of chapter VI to include the distortions in both the apparent receiver loci and the reference aperture when each is viewing a target that is not directly above or below the formation or aperture. This distor-

tion in loci was shown to be applicable to the filled reference aperture yielding an analytic solution for its intensity map. The technique yielded not only the generalized intensity map for warped apertures but a solution technique that may be applied to most other navigation or mapping conventions used to model such systems. The distorted receiver loci and reference apertures in the example problems continued to show the expected improvement in performance (decrease in mean aggregate error) as the number of formation elements increased.

VIII. Conclusions and Recommendations

8.1 Summary

This investigation creates metrics based on models of orbiting distributed apertures performing interferometry missions. The metrics allow the geometry of formations to be refined based on an optimization process. (Finding the true global optimum is a more extensive stochastic process.) The metrics perform a comparison between the image (intensity map) generated by the distributed formation elements at any time and the image theoretically generated by a filled aperture of size comparable to the formation.

Analysis of the nature of satellite formations reveals that for any accepted model, a non-dispersing formation limits design degrees of freedom to a maximum of four per receiver. One of the simplest (and therefore the lowest fidelity) models, Hill's equations, is selected as the primary model for analysis. The relatively short duration dwell times for image generation allow for this simplification, and the choice of imaging model is independent of the model (certainly of higher order) to be used for long-term control and station-keeping. From Hill's equations, the relative paths for each receiver element can be completely specified in terms of the parameters ρ_H, θ_H, m_H, and n_H.

Analysis of the nature of interferometers reveals that the relative length and orientation of the line between each pair of receivers is all important. Each baseline produced by a receiver pair constitutes a measurement of a single spatial frequency. (Filled apertures sample *all* spatial frequency orientations and magnitudes out to the limit of their diameters.) Sampling higher spatial frequency responses yields high image resolution, but at the cost of large blurring sidelobes. Lower spatial frequency samples reduce the blurring sidelobes at the cost of reducing the clarity of fine detail. Selection of an optimal set of spatial frequency magnitudes and orientations is shown to be a tradeoff between these two effects. The actual generation of an image requires sampling these selected spatial frequencies and performing their inverse Fourier transform to isolate the image intensity map, $\mathbf{I}(\xi, \eta)$, in terms of the spatial variables (ξ, η) across the image plane.

Incorporating time averaged errors into the metric offers the promise of generating solutions for which aggregate errors are near minimum for any imaging start time at the

cost of requiring consideration of the loci shapes. Since the formation elements do *not* trace out simple circular paths, the circular aperture references of previous works are discarded in favor of aperture shapes that more precisely encompass all receiver loci. A new solution for the output of an *elliptical* aperture is derived as the shape correctly matching these loci.

Incorporating the distorting effects of viewing formation paths from off-center directions is further investigated. The receiver paths are mapped to the inertial reference frame to mimic their apparent motion as viewed from inertial targets. This mapping depends on the choice of reference orbit for the formation and on the inertial location of the target. In all, five angular variables, ν, i, and Ω from the orbit, and Φ and δ from the inertial target are incorporated into mapping the loci. Beyond the individual loci, the filled reference aperture also requires remapping to the inertial frame. This is accomplished through a generalization of the derived elliptical aperture to yield a solution to a *warped* elliptical aperture that encompasses all possible receiver loci and no additional unreachable aperture areas.

The problem as posed, even for the simplest one-dimensional formation, is non-convex. For reliable solution approximations this necessitated the use of global search techniques that do not get trapped by local minima. Genetic algorithms are selected over simulated annealing or random walk techniques for their robustness and degree of user control. A genetic algorithm is constructed to generate generic populations of chromosomes, each yielding a dimensionless coefficient in the range $[-1.0 \ldots 1.0]$. These coefficients are readily adapted to the dimensionality of any and all of the selectable Hill's parameters for each optimization problem. The search routines maintain a healthy "population" of the most promising solutions, performing crossovers and mutations between population members to generate new prospective members. The parameters defined by each new set of members is subjected to a discrete time simulation that propagated each receiver out in time, calculates the aggregate aperture performance at each time step, compares this performance to an appropriately shaped reference aperture, and yields a time averaged aggregate error. After an empirically determined sufficient number of generations, the best

approximation of the minimum error yields the set of initial conditions for the formation to give control-free performance with near-minimal error.

The validity of the constructed models is supported by the behavior of $\mathbf{J}_{\text{image}}$. The objective function approaches zero (not a fixed finite value) when the reference aperture is shaped to precisely cover the receiver loci and the number of receivers gets arbitrarily large. This indicates that the intensity maps used for $\mathbf{I_o}(\xi, \eta)$ or for the inertial targets $\mathbf{I_o}(\xi, \eta)_\star$ are indeed correctly shaped to encompass *all* possible baselines reachable by receivers and *none* that were not. Setting up the search to synthesize a reachable ideal has several benefits. The genetic algorithm has a set of initial conditions accessing all baselines from which to select those paths sampling the most critical spatial frequencies. It also avoids expending computation effort finding conditions to synthesize areas of an aperture whose spatial frequency components are unreachable by the formation.

Refining the formation geometry for a solution with near-minimum time-averaged error yields a set of defining formation parameters (Hill's parameters, here). These could just as easily have been four parameters from any of the models in chapter 2. When adjusted to these parameters, a formation's control-free dynamics drove receiver loci to yield the highest fidelity image for *any* start time, rather than a single critical point in time. The global search methods employed here could be replaced with a comparable global search technique, but the fidelity of the reference map and the utility of the minimum time-averaged error remain.

8.2 Research Contributions

This research advances the science of modelling the performance of satellite formations performing interferometry. These advanced models facilitate refining satellite formation geometries principally through their use in a performance metric. The search technique employing this metric is a simple genetic algorithm. The highlights of these advancements are as follows:

i. This research formalizes the model for building an intensity map generated by an asymmetric aggregate aperture of discrete receivers, $\overline{\mathbf{I_P}}(\xi, \eta, t)$, with the permutation operator, $\mathbb{P}_2^M$, of equation 4.12.

ii. The generalized second-order metric of equation 4.17 includes model variations over a finite dwell time. This generalized metric results in formations whose control-free motion yields reduced imaging errors for any arbitrary start time, but requires a more sophisticated reference aperture.

iii. Discarding the mathematically simple circular reference aperture in favor of more complex shapes includes *all* available receiver loci and *none* that are unreachable due to the formation dynamics. This requires a new solution for elliptical apertures, equation 5.23.

iv. The receiver loci, as viewed from an inertial target suffer some distortion that affects the formation's performance. This requires an enhancement to Hill's equations to propagate out the receiver paths as viewed from an inertial location, equation 7.6.

v. The analytic solution for an elliptical aperture is generalized to model the distorting effects of non-ideal viewing geometries in terms of the Keplerian elements of the reference orbit and the inertial locations of targets, equation 7.18. This warps the known elliptical aperture solution to encompass all possible receiver paths as viewed from each inertial target.

vi. The method used to generalize the filled aperture solution is a very generic technique for mapping aperture distortions through the **PSF** to the image plane. It may be adapted to model the distortions of viewing geometries described by essentially *any* mapping convention.

vii. The genetic algorithms used were are not advanced, but do illustrate the problem formulation for selecting the defining parameters of simplified formations. This formulation and algorithm application can be adapted to more advanced algorithms or to higher fidelity models, such as the four Delaunay elements of Schaub and Alfriend or the four modal variables of Wiesel, with minimal modification.

8.3 Recommendations for Future Research

As posed, the optimization problem is notoriously non-convex, necessitating the use of computationally intensive global search techniques. The architecture and tools provided by Optimal Synthesis® in their Genetic Search Toolbox® are user-friendly (after a fashion) but carry the heavy computation load of the MatLab environment (acceptable only on very fast workstations). Though larger formations should be expected to require longer computation times, the durations become impractical for formations with more than a dozen receivers. More efficient genetic algorithms exist and should be readily adaptable to the problem. With more efficient computation, further assumptions on the formation geometry may be relaxed, principally the planar assumption. By allowing the full four degree of freedom placement of each receiver's relative orbit, the true optimum may be more closely approximated.

The formation model used throughout this work, Hill's model, was the simplest and therefore the lowest fidelity model available. The Wiesel-Floquet solution (Appendix C) offers modelling accuracies several orders of magnitude better than Hill's. Including such sophistication into the optimization model is intriguing, but with the understanding that this level of fidelity would really only be necessary for systems with very long imaging times or systems using very short wavelengths and requiring the accompanying high-precision receiver positioning.

The non-convexity of the problem may well be removed through the application of new convex hull techniques. A significant amount of research effort was performed (but not included, though the preliminary modelling was promising) to formulate the optimization problem with different logic than that used here. Rather than optimize each formation in a growing series, the problem may be approached by weighting the contributions of a large number of receivers. Minimizing the sum of the weights (an L_1 metric) while constraining the aggregate aperture performance to an arbitrary tolerance holds the promise of zero or near-zero weights on many of the receivers. Thus the solution becomes a matter of reducing a formation size by eliminating the least productive receivers.

Appendix A. The Clohessy-Wiltshire Solution

The Clohessy-Wiltshire approach to describing the dynamics of clustered satellites in a local coordinate frame began with choosing a circular orbit of radius R_o as the local origin, with mean motion $\omega = \sqrt{\frac{\mu_\oplus}{R_o^3}}$. Though Clohessy and Wiltshire originally chose the $\hat{e}_y$ axis in the radial direction and the $\hat{e}_x$ axis in the negative velocity direction [5], the more conventional approach sets $\hat{e}_x$ in the radial, $\hat{e}_y$ in the velocity direction, and $\hat{e}_z$ normal to the orbit plane [49]. (Forgive the volume of algebra presented hereafter, but it is worthwhile to see the extensive approximations necessary to yield a linear system.)

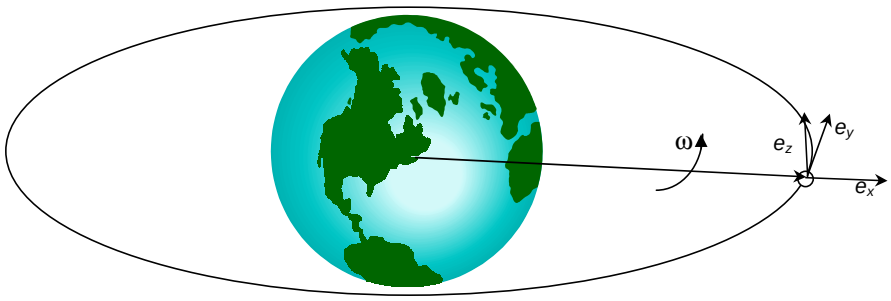

Figure A.1 The Clohessy and Wiltshire problem is more conventionally addressed with $\hat{e}_x$ in the radial direction and $\hat{e}_y$ in the velocity direction.

In this reference frame, the radius vector to a cluster satellite at some location (x, y, z) in the local frame is

$$\vec{r} = (x + R_o)\hat{e}_x + y\hat{e}_y + z\hat{e}_z. \tag{A.1}$$

Since the local reference frame rotates with ω, the velocity vector is

$$\begin{aligned} \dot{\vec{r}} &= \left[\tfrac{d}{dt}\vec{r}\right]_{xyz} + [\omega \times \vec{r}] \\ \dot{\vec{r}} &= [\dot{x}\hat{e}_x + \dot{y}\hat{e}_y + \dot{z}\hat{e}_z] + [\omega(x + R_o)\hat{e}_y - \omega y\hat{e}_x] \\ \dot{\vec{r}} &= (\dot{x} - \omega y)\hat{e}_x + (\dot{y} + \omega(x + R_o))\hat{e}_y + \dot{z}\hat{e}_z \end{aligned} \tag{A.2}$$

and the acceleration vector is

$$\begin{aligned}
\ddot{\vec{r}} &= \left[\tfrac{d}{dt}\dot{\vec{r}}\right]_{xyz} + \left[\omega \times \dot{\vec{r}}\right] \\
\ddot{\vec{r}} &= [(\ddot{x} - \omega\dot{y})\hat{e}_x + (\ddot{y} + \omega\dot{x})\hat{e}_y + \ddot{z}\hat{e}_z] + [\omega(\dot{x} - \omega y)\hat{e}_y - \omega(\dot{y} + \omega(x + R_o))\hat{e}_x] \\
\ddot{\vec{r}} &= (\ddot{x} - 2\omega\dot{y} - \omega^2(x + R_o))\hat{e}_x + (\ddot{y} + 2\omega\dot{x} - \omega^2 y)\hat{e}_y + \ddot{z}\hat{e}_z
\end{aligned} \tag{A.3}$$

In the absence of control forces, gravity is the only acceleration. Therefore

$$\begin{aligned}
\ddot{\vec{r}} &= \tfrac{-\mu\vec{r}}{|\vec{r}|^3} \\
\ddot{\vec{r}} &= \tfrac{-\mu((x+R_o)\hat{e}_x + y\hat{e}_y + z\hat{e}_z)}{((x+R_o)^2+y^2+z^2)^{\frac{3}{2}}}
\end{aligned} \tag{A.4}$$

The denominator here is heinously non-linear, but it may be expanded using the binomial theorem.

$$\begin{aligned}
((x + R_o)^2 + y^2 + z^2)^{\frac{3}{2}} &= (R_o^2 + 2R_o^2 x + x^2 + y^2 + z^2)^{\frac{3}{2}} \\
((x + R_o)^2 + y^2 + z^2)^{\frac{3}{2}} &= R_o^3 \left[1 + \left(\tfrac{2x}{R_o} + \tfrac{x^2}{R_o^2} + \tfrac{y^2}{R_o^2} + \tfrac{z^2}{R_o^2}\right)\right]^{\frac{3}{2}} \\
((x + R_o)^2 + y^2 + z^2)^{\frac{3}{2}} &= R_o^3 \left[1 + \tfrac{3}{2}\left(\tfrac{2x}{R_o} + \tfrac{x^2}{R_o^2} + \tfrac{y^2}{R_o^2} + \tfrac{z^2}{R_o^2}\right) + H.O.T.\right]
\end{aligned} \tag{A.5}$$

Assuming small components in the local coordinate system, $\frac{x^2}{R_o^2}$, $\frac{y^2}{R_o^2}$, and $\frac{z^2}{R_o^2}$ may be assumed ≈ 0, leaving

$$((x + R_o)^2 + y^2 + z^2)^{\frac{3}{2}} \approx R_o^3 \left[1 + \frac{3x}{R_o}\right] = R_o^3 + 3R_o^2 x \tag{A.6}$$

which is closer to linearity. Inserting this into the $\ddot{\vec{r}}$ expression,

$$\ddot{\vec{r}} \approx \frac{-\mu((x + R_o)\hat{e}_x + y\hat{e}_y + z\hat{e}_z)}{R_o^3 + 3R_o^2 x}. \tag{A.7}$$

This expression for the acceleration due to gravity can be equated component by component with equation A.3 to yield the equations of motion.

$$\begin{aligned}
\hat{e}_x &: \tfrac{-\mu(x+R_o)}{R_o^3+3R_o^2x} = \ddot{x} - 2\omega\dot{y} - \omega^2(x+R_o) \\
\hat{e}_y &: \tfrac{-\mu y}{R_o^3+3R_o^2x} = \ddot{y} + 2\omega\dot{x} - \omega^2 y \\
\hat{e}_z &: \tfrac{-\mu z}{R_o^3+3R_o^2x} = \ddot{z}
\end{aligned} \tag{A.8}$$

Noting that $\mu = \omega^2 R_o^3$, a quick bit of algebra yields

$$\begin{aligned}
\ddot{x} &= 2\omega\dot{y} + \omega^2(x+R_o) - \tfrac{\omega^2 R_o^3(x+R_o)}{R_o^3(\frac{R_o+3x}{R_o})} \\
\ddot{y} &= -2\omega\dot{x} + \omega^2 y - \tfrac{\omega^2 R_o^3 y}{R_o^3(\frac{R_o+3x}{R_o})} \\
\ddot{z} &= -\tfrac{\omega^2 R_o^3 z}{R_o^3(\frac{R_o+3x}{R_o})}
\end{aligned} \tag{A.9}$$

$$\begin{aligned}
\ddot{x} &= 2\omega\dot{y} + \omega^2(x+R_o) - \omega^2(x+R_o)\left(\tfrac{R_o}{R_o+3x}\right) \\
\ddot{y} &= -2\omega\dot{x} + \omega^2 y - \omega^2 y\left(\tfrac{R_o}{R_o+3x}\right) \\
\ddot{z} &= -\omega^2 z\left(\tfrac{R_o}{R_o+3x}\right)
\end{aligned} \tag{A.10}$$

$$\begin{aligned}
\ddot{x} &= 2\omega\dot{y} + \omega^2(x+R_o)\left(\tfrac{3x}{R_o+3x}\right) \\
\ddot{y} &= -2\omega\dot{x} + \omega^2 y\left(\tfrac{3x}{R_o+3x}\right) \\
\ddot{z} &= -\omega^2 z\left(\tfrac{R_o}{R_o+3x}\right)
\end{aligned} \quad . \tag{A.11}$$

For small displacements in the local coordinate frame, it is possible to linearize further. Assuming $x + R_o \approx R_o$, and $3x + R_o \approx R_o$,

$$\ddot{x} = 2\omega\dot{y} + 3\omega^2 x \tag{A.12a}$$

$$\ddot{y} = -2\omega\dot{x} \tag{A.12b}$$

$$\ddot{z} = -\omega^2 z \tag{A.12c}$$

which are the classical Clohessy-Wiltshire equations of motion.

By employing normalized, canonical units, ($\omega = 1$, $\mu_\oplus = 1$) it is possible to array the state vector to set up a linear system. Adding in thrusts along each axis as T_x, T_y, and T_z,

$$\begin{bmatrix} \dot{x} \\ \dot{y} \\ \dot{z} \\ \ddot{x} \\ \ddot{y} \\ \ddot{z} \end{bmatrix} = \begin{bmatrix} 0 & 0 & 0 & 1 & 0 & 0 \\ 0 & 0 & 0 & 0 & 1 & 0 \\ 0 & 0 & 0 & 0 & 0 & 1 \\ 3 & 0 & 0 & 0 & 2 & 0 \\ 0 & 0 & 0 & -2 & 0 & 0 \\ 0 & 0 & -1 & 0 & 0 & 0 \end{bmatrix} \begin{bmatrix} x \\ y \\ z \\ \dot{x} \\ \dot{y} \\ \dot{z} \end{bmatrix} + \begin{bmatrix} 0 & 0 & 0 \\ 0 & 0 & 0 \\ 0 & 0 & 0 \\ 1 & 0 & 0 \\ 0 & 1 & 0 \\ 0 & 0 & 1 \end{bmatrix} \begin{bmatrix} \frac{T_x}{m} \\ \frac{T_y}{m} \\ \frac{T_z}{m} \end{bmatrix}. \tag{A.13}$$

This has the familiar form of a linear, constant-coefficient dynamic system [24].

$$\dot{\mathbf{x}} = \mathbf{F}\mathbf{x} + \mathbf{B}\mathbf{u} \tag{A.14}$$

Appendix B. Hill's Equations

As derived in Appendix A, the linearized equations of motion for a satellite formation in a localized coordinate system are

$$\ddot{x} = 2\omega\dot{y} + 3\omega^2 x \tag{B.1a}$$

$$\ddot{y} = -2\omega\dot{x} \tag{B.1b}$$

$$\ddot{z} = -\omega^2 z. \tag{B.1c}$$

As presented by Yeh and Sparks [56], these equations can be parameterized in terms of six arbitrary constants: a, b, ρ, m, n, and θ. Summarizing the derivation by Irvin [15], these equations can be solved in terms of these constants by first performing the Laplace transformation

$$\begin{aligned} s^2X(s) - sx_o - \dot{x}_o &= 2\omega[sY(s) - y_o] + 3\omega^2 X(s) \\ s^2Y(s) - sy_o - \dot{y}_o &= -2\omega[sX(s) - x_o] \\ s^2Z(s) - sz_o - \dot{z}_o &= \omega^2 Z(s), \end{aligned} \tag{B.2}$$

where the subscripted "$_o$" values are the components of initial position and velocity. Collecting these initial conditions, these equations may be expressed in matrix form as

$$\begin{bmatrix} s^2 - 3\omega^2 & -2\omega s & 0 \\ 2\omega s & s^2 & 0 \\ 0 & 0 & s^2 + \omega^2 \end{bmatrix} \begin{bmatrix} X(s) \\ Y(s) \\ Z(s) \end{bmatrix} = \begin{bmatrix} sx_o + \dot{x}_o - 2\omega y_o \\ sy_o + \dot{y}_o - 2\omega x_o \\ sz_o + \dot{z}_o \end{bmatrix}. \tag{B.3}$$

Solving for $X(s)$, $Y(s)$, and $Z(s)$

$$\begin{bmatrix} X(s) \\ Y(s) \\ Z(s) \end{bmatrix} = \begin{bmatrix} \frac{1}{s^2+\omega^2} & \frac{2\omega}{s(s^2+\omega^2)} & 0 \\ \frac{-2\omega}{s(s^2+\omega^2)} & \frac{s^2-3\omega^2}{s^s(s^2+\omega^2)} & 0 \\ 0 & 0 & \frac{1}{s^2+\omega^2} \end{bmatrix} \begin{bmatrix} sx_o + \dot{x}_o - 2\omega y_o \\ sy_o + \dot{y}_o - 2\omega x_o \\ sz_o + \dot{z}_o \end{bmatrix} \tag{B.4}$$

$$\begin{bmatrix} X(s) \\ Y(s) \\ Z(s) \end{bmatrix} = \begin{bmatrix} \frac{sx_o+\dot{x}_o-2\omega y_o}{s^2+\omega^2} + \frac{2\omega(sy_o+\dot{y}_o)+2\omega x_o}{s(s^2+\omega^2)} \\ \frac{-2\omega(sx_o+\dot{x}_o-2\omega y_o)}{s(s^2+\omega^2)} + \frac{(s^2-3\omega^2)(sy_o+\dot{y}_o+2\omega x_o)}{s^2(s^2+\omega^2)} \\ \frac{sz_o+\dot{z}_o}{s^2+\omega^2} \end{bmatrix}. \tag{B.5}$$

Performing the partial fraction expansion,

$$\begin{bmatrix} X(s) \\ Y(s) \\ Z(s) \end{bmatrix} = \begin{bmatrix} \frac{sx_o+\dot{x}_o-2\omega y_o}{s^2+\omega^2} + \frac{2\omega^2 y_o-2s\dot{y}_o-4s\omega x_o}{\omega(s^2+\omega^2)} + \frac{2\dot{y}_o+4\omega x_o}{\omega}\frac{1}{s} \\ \frac{4sy_o+4\dot{y}_o+8\omega x_o}{s^2+\omega^2} + \frac{-2\omega^2 x_o+2s\dot{x}_o-4sy_o\omega}{\omega(s^2+\omega^2)} + \frac{-3\dot{y}_o-6\omega x_o}{s^2} + \frac{\omega y_o-2\dot{x}_o}{\omega}\frac{1}{s} \\ \frac{sz_o+\dot{z}_o}{s^2+\omega^2} \end{bmatrix}. \tag{B.6}$$

Set up for the inverse Laplace transform by collecting terms,

$$\begin{bmatrix} X(s) \\ Y(s) \\ Z(s) \end{bmatrix} = \begin{bmatrix} \frac{\left(x_o-\frac{2\dot{y}_o+4\omega x_o}{\omega}\right)s}{s^2+\omega^2} + \frac{\left(\frac{\dot{x}_o}{\omega}\right)\omega}{s^2+\omega^2} + \frac{2\dot{y}_o+4\omega x_o}{\omega}\frac{1}{s} \\ \frac{2\left(\frac{\dot{x}_o}{\omega}\right)s}{s^2+\omega^2} + \frac{2\left(\frac{2\dot{y}_o+4\omega x_o}{\omega}-x_o\right)\omega}{s^2+\omega^2} - \frac{3\omega}{2}\frac{2\dot{y}_o+4\omega x_o}{\omega}\frac{1}{s^2} + \frac{\omega y_o-2\dot{x}_o}{\omega}\frac{1}{s} \\ \frac{sz_o}{s^2+\omega^2} + \frac{\left(\frac{\dot{z}_o}{\omega}\right)\omega}{s^2+\omega^2} \end{bmatrix}, \tag{B.7}$$

and perform the inverse transform [36]

$$x(t) = \left(-3x_o - \frac{2\dot{y}_o}{\omega}\right)\cos(\omega t+\theta) + \frac{\dot{x}_o}{\omega}\sin(\omega t+\theta) + \frac{2\dot{y}_o}{\omega} + 4x_o \tag{B.8a}$$

$$y(t) = 2\left(\frac{\dot{x}_o}{\omega}\right)\cos(\omega t+\theta) + 2\left(\frac{2\dot{y}_o}{\omega}+3x_o\right)\sin(\omega t+\theta) - \frac{3\omega t}{2}\left(\frac{2\dot{y}_o}{\omega}+4x_o\right) + \frac{\omega y_o - 2\dot{x}_o}{\omega} \tag{B.8b}$$

$$z(t) = z_o\cos(\omega t+\theta) + \frac{\dot{z}_o}{\omega}\sin(\omega t+\theta). \tag{B.8c}$$

Note that θ is just an initial phase angle. Since the initial conditions are not time-dependent, and ω is a constant for the system, it is possible to define the following constants,

$$a_H = \frac{2\dot{y}_o + 4\omega x_o}{\omega} \tag{B.9a}$$

$$b_H = \frac{\omega y_o - 2\dot{x}_o}{\omega} \tag{B.9b}$$

$$\rho_H^2 = (x_o - a)^2 + \left(\frac{\dot{x}_o}{\omega}\right)^2 \tag{B.9c}$$

$$m_H = \frac{\dot{z}_o\dot{x}_o - z_o\omega^2(a - x_o)}{\dot{x}_o^2 + \omega^2(a - x_o)^2} \tag{B.9d}$$

$$n_H = \frac{z_o\dot{x}_o\omega + \dot{z}_o\omega(a - x_o)}{2(\dot{x}_o^2 + \omega^2(a - x_o)^2)} \tag{B.9e}$$

$$\tan\theta_H = \frac{\omega(x_o - a)}{\dot{x}_o}. \tag{B.9f}$$

These constants describe the size, shape, and phase of the formation elements' relative orbits in the local coordinate system. Their physical interpretation within the $x - y$ plane is shown in figure B. The parameter m_H is the tangent of the angle between the minor axis and $\hat{e}_x$, and n_H is the tangent of the angle between the major axis and $\hat{e}_y$.

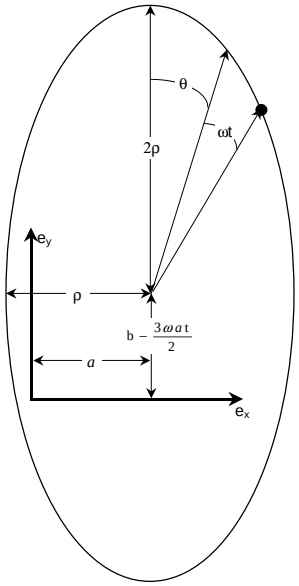

Figure B.1 The constants defined to parameterize the C-W solution define the relative orbit size (ρ_H), location (a_H and b_H), and phase (θ_H).

Using these parameters, Clohessy and Wiltshire's solutions may be written as

$$
\begin{aligned}
x(t) &= \rho_H \sin(\omega t + \theta_H) + a_H && \text{(B.10a)} \\
y(t) &= 2\rho_H \cos(\omega t + \theta_H) - \frac{3\omega}{2} a_H t + b_H && \text{(B.10b)} \\
z(t) &= m_H \rho_H \sin(\omega t + \theta_H) + n_H 2\rho_H \cos(\omega t + \theta_H). && \text{(B.10c)}
\end{aligned}
$$

Obviously, the secular term in $y(t)$ causes a problem for maintaining a closed path in the local coordinate system. Therefore, keeping a formation together requires $a_H = 0$, or setting the center of the orbit on the $\hat{e}_y$ axis. This yields the initial constraint of $\dot{y}_o = -2\omega x_o$. From Yeh and Sparks [56], the parameterization yields the identities

$$
\begin{aligned}
&\tfrac{(x-a_H)^2}{\rho_H^2} + \tfrac{\left(y+\frac{3\omega}{2}a_H t - b_H\right)^2}{(2\rho_H)^2} = 1 \\
&z(t) = m_H(x - a_H) + n_H(y + \tfrac{3\omega}{2}a_H t - b_H).
\end{aligned}
\qquad \text{(B.11)}
$$

For a non-dispersing formation, these become

$$
\begin{aligned}
&\tfrac{x^2}{\rho_H^2} + \tfrac{(y-b_H)^2}{(2\rho_H)^2} = 1 \\
&z(t) = m_H x + n_H(y - b_H),
\end{aligned}
\qquad \text{(B.12)}
$$

and b_H becomes simply an offset of the relative orbit along the velocity direction. Since Hill's equations have a limited range of validity, there is no immediate reason to offset the origin from the ellipse center, so formations also set $b_H = 0$. Thus the degrees of freedom for the orbit of each allowable element of a formation have been reduced from six to four, in agreement with the initial formulations of Schaub and Alfriend [37].

Appendix C. The Wiesel-Floquet Solution

As presented by Dr. William E. Wiesel [54], the linear, time-invariant solution of Clohessy-Wilshire can be replaced by a linear, *time-periodic* solution using the techniques of Floquet.

C.1 The Hamiltonian in the C-W Reference Frame

Begin by defining $\mathcal{I}$, the three inertial coordinates and three inertial momenta (per unit mass, essentially the velocity components) of a formation element, as $\mathcal{I}^T = [X, Y, Z, P_X, P_y, P_Z]$. Using normalized, canonical units (similar to the end of Appendix A, where $R_\oplus = 1$, $M_\oplus = 1$, and $G = 1$), all of the zonal harmonics may be included in the Hamiltonian, $\mathcal{H}$, to yield

$$\mathcal{H} = \frac{1}{2}\left\{P_X^2 + P_Y^2 + P_Z^2\right\} - \frac{1}{r} + \frac{J_2}{2r^3}\left\{3\frac{Z^2}{r^2} - 1\right\} + \frac{J_3}{2r^4}\left\{5\frac{Z^3}{r^3} - 3\frac{Z}{r}\right\} + \frac{J_4}{8r^5}\left\{35\frac{Z^4}{r^4} - 30\frac{Z^2}{r^2} + 3\right\} + \ldots \tag{C.1}$$

where $r = \sqrt{X^2 + Y^2 + Z^2}$. Additional conservative perturbations, besides the zonal harmonics shown, may be added to this Hamiltonian by simply adding in their potential functions. Non-conservative perturbations (drag, etc.) are slightly more difficult, but may be added by first expanding them about the periodic orbit and then adding them in terms of the momentum states.

In inertial space, this orbit will not close on itself, since it undergoes some nodal regression, $\dot{\Omega}$. Setting up a rotation matrix for a total rotation of $\Omega_o + \dot{\Omega}t$ about the inertial Z axis is simple.

$$\mathcal{R}_Z = \begin{bmatrix} \cos(\Omega_o + \dot{\Omega}t) & \sin(\Omega_o + \dot{\Omega}t) & 0 \\ -\sin(\Omega_o + \dot{\Omega}t) & \cos(\Omega_o + \dot{\Omega}t) & 0 \\ 0 & 0 & 1 \end{bmatrix} \tag{C.2}$$

This allows the components of $\mathcal{I}$ to be mapped into the rotating *nodal* reference frame, $\mathcal{N}$, via

$$\mathcal{N} = \begin{bmatrix} X' \\ Y' \\ Z' \\ P'_X \\ P'_Y \\ P'_Z \end{bmatrix} = \begin{bmatrix} & & & 0 & 0 & 0 \\ & \mathcal{R}_Z & & 0 & 0 & 0 \\ & & & 0 & 0 & 0 \\ 0 & 0 & 0 & & & \\ 0 & 0 & 0 & & \mathcal{R}_Z & \\ 0 & 0 & 0 & & & \end{bmatrix} \begin{bmatrix} X \\ Y \\ Z \\ P_X \\ P_Y \\ P_Z \end{bmatrix}. \tag{C.3}$$

With this rotation into the nodal frame, the Hamiltonian grows an extra term. Using $V(Z', r)$ to incorporate the zonal harmonic terms from equation C.1 rotated into the nodal frame, the new Hamiltonian, $\mathcal{H}'$, becomes

$$\mathcal{H}' = \frac{1}{2}\left\{P'^2_X + P'^2_Y + P'^2_Z\right\} + \dot{\Omega}\left\{P'_X Y' - P'_Y X'\right\} + V(Z', r). \tag{C.4}$$

In this frame, the orbit now closes on itself and is therefore periodic, and has a periodic solution. It is possible to shift the origin out to the local coordinate origin of the familiar C-W reference frame. This is done by subtracting off the reference orbit state vector $\mathcal{N}_o = (X'_o, Y'_o, Z'_o, P'_{Xo}, P'_{Yo}, P'_{Zo})$ in the nodal frame to define $\mathcal{Y}$ as [1]

$$\mathcal{Y}(t) = \begin{bmatrix} x_n \\ y_n \\ z_n \\ \dot{x}_n \\ \dot{y}_n \\ \dot{z}_n \end{bmatrix} = \begin{bmatrix} X' \\ Y' \\ Z' \\ P'_X \\ P'_Y \\ P'_Z \end{bmatrix} - \begin{bmatrix} X'_o \\ Y'_o \\ Z'_o \\ P'_{Xo} \\ P'_{Yo} \\ P'_{Zo} \end{bmatrix}. \tag{C.5}$$

This is a canonical transformation, and reduces the Hamiltonian, $\mathcal{H}''$, function to its quadratic and higher order terms evaluated on the periodic orbit (0 subscript)

[1] The notation for coordinates hereafter is a significant departure from that used by Dr. Wiesel [54], but is adopted for consistency with that used in the C-W solution and Hill's equations, where the notation $(x, y, z, \dot{x}, \dot{y}, \dot{z})$ is reserved for coordinates specifically in the C-W reference frame.

$$\begin{aligned}\mathcal{H}'' &= \tfrac{1}{2!}\left[\left.\frac{\partial^2\mathcal{H}'}{\partial\mathcal{N}_\alpha\partial\mathcal{N}_\beta}\right|_0\right]\mathcal{Y}_\alpha\mathcal{Y}_\beta + \tfrac{1}{3!}\left[\left.\frac{\partial^3\mathcal{H}'}{\partial\mathcal{N}_\alpha\partial\mathcal{N}_\beta\partial\mathcal{N}_\gamma}\right|_0\right]\mathcal{Y}_\alpha\mathcal{Y}_\beta\mathcal{Y}_\gamma + \dots \\ \mathcal{H}'' &= \tfrac{1}{2!}\left[\mathcal{H}''_{\alpha\beta}\right]\mathcal{Y}_\alpha\mathcal{Y}_\beta + \tfrac{1}{3!}\left[\mathcal{H}''_{\alpha\beta\gamma}\right]\mathcal{Y}_\alpha\mathcal{Y}_\beta\mathcal{Y}_\gamma + \dots\end{aligned}, \tag{C.6}$$

where the repeated Greek indices simplify the notation for tensor multiplication, and are summed from one to six. The $\mathcal{H}''_{\alpha\beta}$ and $\mathcal{H}''_{\alpha\beta\gamma}$ terms are from the fully symmetric second, third, and higher order tensors of partial derivatives with respect to the nodal vector, $\mathcal{N}$.

One final rotation is necessary to align these axes to the familiar radial, velocity, and orbit normal axes of C-W. Using $\vec{r}$ and $\vec{v}$ for the nodal frame position and velocity vectors, define the rotation matrix $\mathcal{R}$ by

$$\mathcal{R} = \begin{bmatrix} \hat{u}_1 \\ \hat{u}_2 \\ \hat{u}_3 \end{bmatrix} = \begin{bmatrix} \frac{\vec{r}}{|\vec{r}|} \\ \hat{u}_3 \times \hat{u}_1 \\ \frac{\vec{r}\times\vec{v}}{|\vec{r}\times\vec{v}|} \end{bmatrix}, \tag{C.7}$$

and finally write the new position and velocity coordinates in the standard C-W frame, $\mathcal{X}$(t), with

$$\mathcal{X} = \begin{bmatrix} x \\ y \\ z \\ \dot{x} \\ \dot{y} \\ \dot{z} \end{bmatrix} = \begin{bmatrix} & & & 0 & 0 & 0 \\ & \mathcal{R} & & 0 & 0 & 0 \\ & & & 0 & 0 & 0 \\ 0 & 0 & 0 & & & \\ 0 & 0 & 0 & & \mathcal{R} & \\ 0 & 0 & 0 & & & \end{bmatrix} \begin{bmatrix} x_n \\ y_n \\ z_n \\ \dot{x}_n \\ \dot{y}_n \\ \dot{z}_n \end{bmatrix}. \tag{C.8}$$

This is also a canonical transformation, with a generating function

$$\mathbf{F}_2 = \begin{bmatrix} \dot{x} \\ \dot{y} \\ \dot{z} \end{bmatrix} \cdot \mathcal{R} \begin{bmatrix} x_n \\ y_n \\ z_n \end{bmatrix} = \begin{bmatrix} \dot{x} \\ \dot{y} \\ \dot{z} \end{bmatrix} \cdot \begin{bmatrix} x \\ y \\ z \end{bmatrix}, \tag{C.9}$$

with which the Hamiltonian can be transformed term by term into the $\mathcal{X}$ variables to yield $\mathcal{K}$. The quadratic term, $\mathcal{K}_2$, looks like this

$$\mathcal{K}_2 = \tfrac{1}{2!}\mathcal{H}''_{\alpha\beta}\mathcal{Y}_\alpha\mathcal{Y}_\beta + \tfrac{\partial \mathbf{F}_2}{\partial t}$$

$$\mathcal{K}_2 = \tfrac{1}{2!}\mathcal{H}''_{\alpha\beta}\mathcal{R}^{(2)}_{\alpha\gamma}\mathcal{R}^{(2)}_{\beta\delta}\mathcal{X}_\gamma\mathcal{X}_\delta + \begin{bmatrix} \dot{x} \\ \dot{y} \\ \dot{z} \end{bmatrix} \cdot \dot{\mathcal{R}}\mathcal{R}^T \begin{bmatrix} x \\ y \\ z \end{bmatrix}, \tag{C.10}$$

where $\mathcal{R}^{(2)}$ is the block diagonal rotation matrix from equation C.8. Higher order terms are even simpler; the third order term is

$$\mathcal{K}_3 = \frac{1}{3!}\mathcal{H}''_{\lambda\sigma\tau}\mathcal{R}^{(2)}_{\lambda\alpha}\mathcal{R}^{(2)}_{\sigma\beta}\mathcal{R}^{(2)}_{\tau\gamma}\mathcal{X}_\alpha\mathcal{X}_\beta\mathcal{X}_\gamma. \tag{C.11}$$

C.2 The Floquet Solution

Though the Hamiltonian derived for the C-W reference frame is truly an infinite sum, approximating it by only the second order term, $\mathcal{K}_2$, not only preserves inclusion of all the zonal harmonics, but yields a matrix linear system. Using Hamilton's equations of motion [11] on $\mathcal{K}(x, y, z, \dot{x}, \dot{y}, \dot{z})$, it is possible to generate the plant matrix from

$$\ddot{x} = -\tfrac{\partial \mathcal{K}}{\partial x}, \quad \ddot{y} = -\tfrac{\partial \mathcal{K}}{\partial y}, \quad \ddot{z} = -\tfrac{\partial \mathcal{K}}{\partial z} \tag{C.12}$$

such that the equations of variation may be written

$$\partial\dot{\mathcal{X}} = \mathbf{A}(t)\partial\mathcal{X}$$

$$\partial\dot{\mathcal{X}} = \begin{bmatrix} 0 & 0 & 0 & 1 & 0 & 0 \\ 0 & 0 & 0 & 0 & 1 & 0 \\ 0 & 0 & 0 & 0 & 0 & 1 \\ & & & 0 & 0 & 0 \\ & -\frac{\partial \mathcal{K}}{\partial x,y,z} & & 0 & 0 & 0 \\ & & & 0 & 0 & 0 \end{bmatrix} \partial\mathcal{X}. \tag{C.13}$$

Their solution [8], the state transition matrix $\Phi(t, 0)$, may also be propagated via the equations of variation

$$\mathcal{X}(t) = \Phi(t, 0)\mathcal{X}(0) \tag{C.14}$$

$$\dot{\Phi}(t,0) = \mathbf{A}(t)\Phi(t,0). \tag{C.15}$$

Since the $\mathbf{A}$(t) matrix is periodic, $\mathbf{A}(t+\tau) = \mathbf{A}(t)$, the state transition matrix for the reference orbit (whether there is a satellite at the origin or not) may be integrated over one orbit period, τ, which yields the monodromy matrix, $\Phi(\tau, 0)$. This state transition matrix may be factored using the techniques of Floquet [25] as

$$\Phi(t,0) = \mathbf{F}(t)e^{\mathbf{J}t}\mathbf{F}(0)^{-1}, \tag{C.16}$$

where $\mathbf{F}(t)$is a periodic modal matrix, and $\mathbf{J}$is a Jordan normal form matrix of system frequencies described by Poincaré exponents, of the form

$$\mathbf{J} = \begin{bmatrix} 0 & \omega_1 & 0 & 0 & 0 & 0 \\ -\omega_1 & 0 & 0 & 0 & 0 & 0 \\ 0 & 0 & 0 & 1 & 0 & 0 \\ 0 & 0 & 0 & 0 & 0 & 0 \\ 0 & 0 & 0 & 0 & 0 & 1 \\ 0 & 0 & 0 & 0 & 0 & 0 \end{bmatrix}, \tag{C.17}$$

where the one non-degenerate frequency ω_1 is the frequency of the advance of perigee. The frequencies may theoretically be determined from the eigenvalues of the monodromy matrix, λ_i via

$$\lambda_i = e^{\omega_i \tau} \tag{C.18a}$$

$$\omega_i = \frac{\ln \lambda_i}{\tau}. \tag{C.18b}$$

Using this relation, and substituting equation C.16 into equation C.13 yields

$$\dot{\mathbf{F}}(t) = \mathbf{A}(t)\mathbf{F}(t) - \mathbf{F}(t)\mathbf{J}, \tag{C.19}$$

from which $\mathbf{F}(t)$ may be found. However, this is a difficult integration, since there are two integrals of the motion, two pairs of the Poincaré exponents are zeros. Therefore all but two

of the eigenvectors of $\mathbf{F}(t)$ are generalized eigenvectors. Wiesel devised a mildly convoluted method for directly determining these eigenvectors (which most software packages utterly fail to accomplish).

Label the first two eigenvectors $\mathbf{f}_1$ and $\mathbf{f}_2$, corresponding to the non-zero eigenvalues. Two more eigenvectors may be directly calculated. Use $\hat{k}$ as the unit vector in the inertial $\vec{Z}$ direction, and

$$\begin{aligned} \mathbf{f}_3 &= \mathcal{R}\tfrac{d\mathcal{N}_o}{dt} \\ \mathbf{f}_5 &= \begin{bmatrix} \mathcal{R}\hat{k} \times \begin{bmatrix} X' \\ Y' \\ Z' \end{bmatrix} \\ \mathcal{R}\hat{k} \times \begin{bmatrix} P'_x \\ P'_y \\ P'_z \end{bmatrix} \end{bmatrix}. \end{aligned} \tag{C.20}$$

The remaining eigenvectors, $\mathbf{f}_4$ and $\mathbf{f}_6$, must satisfy

$$\begin{aligned} (\Phi - \mathbf{I})\,\mathbf{f}_4 &= \tau \mathbf{f}_3 \\ (\Phi - \mathbf{I})\,\mathbf{f}_6 &= \tau \mathbf{f}_5, \end{aligned} \tag{C.21}$$

but it is not possible to directly calculate $\mathbf{f}_4$ and $\mathbf{f}_6$ with $(\Phi - \mathbf{I})^{-1}$ since $(\Phi - \mathbf{I})$ has four zero eigenvalues. Noting that the generalized eigenvectors are undetermined to within the addition of a multiple (γ) of one of the normal eigenvectors, the remaining eigenvectors must satisfy

$$\begin{aligned} \mathbf{f}'_4 &= \mathbf{f}_4 + \gamma \mathbf{f}_3 \\ \mathbf{f}'_6 &= \mathbf{f}_6 + \gamma \mathbf{f}_5. \end{aligned} \tag{C.22}$$

Finally the orthogonality of the eigenvectors may be used to resolve the ambiguity since

$$\begin{aligned} \mathbf{f}_4 \cdot \mathbf{f}_3 &= \mathbf{f}_6 \cdot \mathbf{f}_3 = 0 \\ \mathbf{f}_4 \cdot \mathbf{f}_5 &= \mathbf{f}_6 \cdot \mathbf{f}_5 = 0. \end{aligned} \tag{C.23}$$

With the $\mathbf{F}(t)$ matrix calculated, the position vector of a satellite may be determined in the C-W reference frame by inserting equation C.16 back into C.14

$$\mathcal{X}(t) = \mathbf{F}(t)e^{\mathbf{J}t}\mathbf{F}(0)^{-1}\mathcal{X}(0). \tag{C.24}$$

The position vector in inertial coordinates may be determined by rotating the C-W reference frame vector to the nodal coordinate frame using $\mathcal{R}^{(2)T}$, adding in the reference orbit, $\mathcal{N}_o$, and rotating the sum into the inertial frame with $\mathcal{R}_Z^{(2)T}$.

$$\mathcal{I}(t) = \mathcal{R}_Z^{(2)T}\left(\mathcal{N}_o(t) + \mathcal{R}^{(2)T}\mathbf{F}(t)e^{\mathbf{J}t}\mathbf{F}(0)^{-1}\mathcal{X}(0)\right) \tag{C.25}$$

C.3 The Modal Variables Solution

The raw Floquet solution of the last section makes physical interpretation difficult. Therefore, Dr. Wiesel proposed the further change of variables from the variational equations of equation C.13 to the modal variables $\mathcal{Z}$. Define

$$\mathcal{Y}(t) = \mathcal{R}^{(2)}(t)\mathbf{F}(t)\mathcal{Z} = \mathbf{E}(t)\mathcal{Z}, \tag{C.26}$$

where $\mathcal{Z}$ is a six-vector of the Floquet modal amplitudes, $\mathcal{Z}^T = (z_1, z_2, z_3, z_4, z_5, z_6)$, and $\mathbf{E}$(t) is the Floquet modal matrix rotated to the nodal frame. Substituting this into Hamilton's equations of motion, written for $\mathcal{H}'$, yields

$$\begin{aligned} \tfrac{d}{dt}\mathcal{Z} &= \left(\mathbf{E}^{-1}\mathbf{A}\mathbf{E} - \mathbf{E}^{-1}\dot{\mathbf{E}}\right)\mathcal{Z} \\ \tfrac{d}{dt}\mathcal{Z} &= \mathbf{J}\mathcal{Z} \end{aligned} \tag{C.27}$$

where $\mathbf{J}$ is the Jordan normal form matrix from equation C.17. Dr. Wiesel showed [52] [53] that with $\mathbf{J}$ arranged in this manner, z_4 and z_6 must be set to 0 to prevent formation dispersion, again in agreement with the four degree of freedom conclusion of Schaub and Alfriend [37].

Appendix D. Spatial Frequency Measurements in Interferometery

This derivation summarizes Thompson's [46] description of how coordinates in the $(\vec{u}\ \vec{v}\ \vec{w})$ reference frame are both unitless physical lengths *and* spatial frequency variables (as could be inferred from their appearance in $\mathcal{V}(u,v)$).

The basic operation of an interferometer analyzes an incoming wavefront from a distant source as received by two receivers with separation D. Take the geometry from figure 3.4, and assume for the moment that the antennas have perfect beam patterns, so $\Gamma(\mathbf{D}) = \mathbf{R}(\mathbf{D})$.

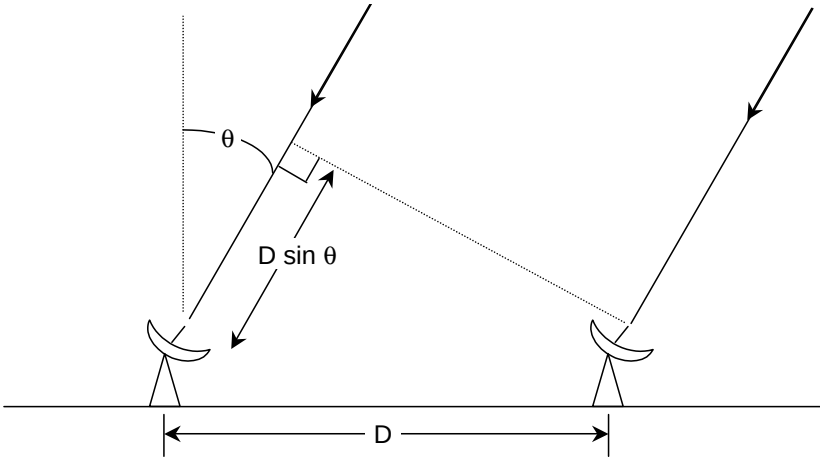

Figure D.1 Incident wavefronts from a target source at θ arrive at the two receivers at times that differ by $\tau = \frac{D\sin\theta}{c}$.

The output of the correlator at any time, t, should be a simple function of the center frequency ν_o, the baseline, and the angle to the source.

$$\begin{aligned}\mathbf{R}(\mathbf{D},\theta,t) &= 2\sin[2\pi\nu_o t]\sin\left[2\pi\nu_o\left(t-\frac{D\sin\theta}{c}\right)\right] \\ &= \cos 2\pi\nu_o\left(\frac{D\sin\theta}{c}\right) - \cos(4\pi\nu_o t)\cos\left(2\pi\nu_o\left(\frac{D\sin\theta}{c}\right)\right) - \sin(4\pi\nu_o t)\sin\left(2\pi\nu_o\left(\frac{D\sin\theta}{c}\right)\right)\end{aligned}$$

A correlator also serves to filter out noise. Since the ν_o is far greater than the frequency of θ (the angular rate of physically moving the receivers), the high frequency portions of

$\mathbf{R}(\mathbf{D}, \theta, t)$ are easily filtered out, leaving[1]

$$\mathbf{R}(\mathbf{D}, \theta) \approx \cos\left(\frac{2\pi\nu_o D}{c}\sin\theta\right) = \cos\left(\frac{2\pi D}{\lambda_o}\sin\theta\right) \tag{D.2}$$

where λ_o is the wavelength of the center frequency. Since a correlator both multiplies and time-averages the received signals (voltages, $V(t)$), the response over a finite time T is

$$\mathbf{R}(\mathbf{D}, \theta) = \mathbf{R}(\tau) = \frac{1}{2T}\int_{-T}^{T} V(t)V\left(t-\tau\right)dt. \tag{D.3}$$

In the limit,

$$\mathbf{R}(\tau) = \lim_{T\to\infty}\frac{1}{2T}\int_{-T}^{T} V(t)V\left(t-\tau\right)dt \tag{D.4}$$

which Thompson terms an autocorrelation function (or is directly proportional to Rohlfs [35] "mutual coherence" function, equation 3.6).

Rather than assume a constant field strength from the source, as in the derivation of section 3.2.1, allow it to vary by frequency. At any frequency, ν, the field strength, $U(\nu)$ is directly related to the response function by the Wiener-Khinchin relation (see Thompson [46] and Maybeck [24]). The power spectral density, $|U(\nu)|^2$, of a signal is the Fourier transform of its autocorrelation function

$$\begin{aligned} |U(\nu)|^2 &= \textstyle\int_{-\infty}^{\infty}\mathbf{R}(\tau)e^{-2i\pi\nu\tau}d\tau \\ \mathbf{R}(\tau) &= \textstyle\int_{-\infty}^{\infty}|U(\nu)|^2 e^{2i\pi\nu\tau}d\nu \end{aligned} \tag{D.5}$$

Therefore the interferometer's output as a function of θ (or τ) is the Fourier transform of the power spectral density of the signal. This yields the general result that the response function $\mathbf{R}(\tau)$ shows fringes whose spatial frequency period varies inversely with $\frac{D}{\lambda_o}$ at any signal frequency (just as in equation 3.15).

In practice, to use an interferometer to map a target, the delay time τ is calculated for a nominal direction θ_o at the source center. (This may also be tuned to a desired shorter delay by adding in an instrument delay.) For some small angular displacement θ'

[1] Rohlfs [35] shows that this approximation is valid for correlators designed to either multiply or add the signals.

from θ_o, the correlator output, equation D.2, for $\theta = \theta_o - \theta'$ becomes

$$\begin{aligned}
\mathbf{R}(\mathbf{D}, \theta) = \mathbf{R}(\tau) &= \cos\left(2\pi \frac{D \sin\theta}{\lambda_o}\right) && \text{(D.6a)} \\
&= \cos\left[2\pi \frac{D}{\lambda_o}\left(\sin\theta_o \cos\theta' - \cos\theta_o \sin\theta'\right)\right] && \text{(D.6b)} \\
&\approx \cos\left[2\pi \frac{D}{\lambda_o}(\sin\theta_o - \theta' \cos\theta_o)\right] && \text{(D.6c)}
\end{aligned}$$

It is therefore convenient to define a value $u = \frac{D\cos\theta_o}{\lambda_o}$ to be the component of antenna spacing orthogonal to the direction θ_o and $\xi = \sin\theta' \approx \theta'$. The (one dimensional) output fringe pattern for a coordinate system oriented so $\theta_o = 0$ with fixed $\mathbf{D}$ becomes

$$\mathbf{R}(\xi) = \cos(2\pi u \xi) \tag{D.7}$$

The quantity u is interpreted as a unitless length describing a component of antenna spacing, measured in number of wavelengths of λ_o. It is also a *spatial frequency* with dimensionless units of $\frac{\text{cycles}}{\text{radian}}$, since it describes the transformed response of a source at ξ radians away from θ_o. (See equation 3.18 to quickly see why u, ξ and their two dimensional counterparts v and η must be dimensionless.)

Appendix E. A Genetic Algorithm

The purpose of this research is *not* to advance the science of genetic algorithms. However, the heavy reliance on them to solve the inherently non-convex problems warrants a more extensive discussion of their implementation.

The numeric portions of this research were conducted in the MATLAB 5.0 and 6.0 environments. Genetic search routines are notoriously computationally intensive (solution time ranged for 24 hours for small formations to five or six days for the largest formations), but the speed of available workstations made the MATLAB computational overhead an acceptable tradeoff with user-friendliness and available genetic operation support. Most notably, the Genetic Search Toolbox 1.0.3 by Optimal Synthesis Inc provided a significant set of genetic operation functions and guidance for building stable search routines. Rather than include a complete listing of raw code, this appendix summarizes the coding logic and sequence of commands used to build and execute the genetic search "engine."

E.1 Defining the Initial Populations

The Genetic Search Toolbox® is designed to operate on genes and chromosomes as character strings. Its basic set of genes are defined as a set of alpha-numerics, each with a numeric equivalent. These may then be converted to numerical values by evaluating the numerical equivalent of each name with the associated arithmetic operations. As cited in chapter VI, the set of single precision genes used certainly span the solution space (but is none too clever). The actual coding looks more like this:

```
u1=1
u2=2
u3=3
u4=4
u5=5
u6=6
u7=7
u8=8
u9=9
u10=0.1
u11=0.01
u12=0.001
u13=0.0001
u14=0.00001
u15=0.000001
```

Using these character string genes, it is necessary to define an initial set of chromosomes for each population. For coding efficiency, the same set of chromosomes is built into

each population. These then build their own "diversity" in succeeding generations. The population building process uses the `gs new(...)` command, in a larger form of the following loop.

```
for rr = 1:NumPops
   mem id = gs new(['Pop',num2str(rr)], 'u6*u10+u15+u14+u13+u12+u11');
   mem id = gs new(['Pop',num2str(rr)], 'u15*u15+u5*u14+u6*u13+u7*u12+u8*u11');
   mem id = gs new(['Pop',num2str(rr)], 'u15*u13+u14/u12+u13*u11+u12/u10+u11*u1');
   mem id = gs new(['Pop',num2str(rr)], 'u15/u13+u14*u12+u13/u11+u12/u10+u11*u1');
   mem id = gs new(['Pop',num2str(rr)],'-u15*u2/u12-u14*u3/u7+u13*u4-u12*u5-u10*u4');
   mem id = gs new(['Pop',num2str(rr)], 'u15*u2-u14*u3+u13*u4-u12*u5+u10*u2');
   mem id = gs new(['Pop',num2str(rr)], 'u15*u3+u14*u4-u13*u5+u11*u6+u10*u4');
   mem id = gs new(['Pop',num2str(rr)],'-u15*u2-u14*u3+u13*u4-u12*u5-u10*u6');
   mem id = gs new(['Pop',num2str(rr)], 'u15*u2+u14*u3+u13*u4+u12*u5-u11*u6');
end
```

This coding technique builds an arbitrary number, `NumPops`, of populations, each "seeded" with a set of chromosomes that include all gene names and the arithmetic operations of addition, subtraction, multiplication, and division.

Each set of chromosomes (one from each population) must be assigned a fitness value. The following nest of loops accomplishes this for the arbitrary number of populations, over an arbitrary number of receivers, `numrec`.

```
mem count = gs popsize('Pop1');
for id = 1:mem count
   for rr = 1:NumPops
      chr=strvcat(chr, [gs get(['Pop' num2str(rr)], id)]);
   end
   for rr = 1:  numrec
      recloc(rr,:)=[eval(chr(rr,:))          eval(chr(rr+numrec,:))
                    eval(chr(2*numrec+1,:))  eval(chr(2*numrec+2,:))];
   end
   for z=1:numrec
      constraint(z,:)=[abs(recloc(z,1)) abs(recloc(z,2))];
   end
   if constraint<=[ones(numrec,1),ones(numrec,1)]
      fitness = Jfunc(recloc,xi,eta,Dlam,arc,steps,a,b,iorb,RAorb,nuorb,RAtarg,dectarg);
      for rr = 1:NumPops
         mem id = gs set fit(['Pop',num2str(rr)],id,fitness);
      end
   else
      for rr = 1:NumPops
         mem del = gs del(['Pop',num2str(rr)],id);
      end
   end


end
```

The `gs get(...)` function extracts individual chromosome strings from the population for each degree of freedom. Each is then converted by the `eval(...)` function into numerical values. Evaluation of the `Jfunc(...)` function is the main outside code path. It calls up the master function that calls the orbital propagation, calls the aperture synthesis, calls the comparison aperture generation, and performs the aperture comparison. All of these calls return a single numerical value as described in chapter IV.

E.2 Performing the Genetic Search

Each genetic search loop begins with a check on population size. To ensure a diverse chromosome population, the maximum population is maintained at 500. Once the population exceeds this, the `gs sel hifit(...)` function selects the character string of the chromosome with the largest fitness value for deletion . (There is a related function recommended by the generic code writer, `gs selr hifit(...)`, which selects chromosomes randomly but *weighted* toward those with higher fitness values. Unfortunately, the high initial "infant mortality" inherent in the searches made it nearly inevitable that just weighting the selection eventually allowed the deletion of the current *best* chromosome.)

```
mem count = gs popsize('Pop1');
if mem count > MaxPopulation
   mem ids = gs sel hifit('Pop1');
   for rr = 1:NumPops
      gs del(['Pop',num2str(rr)],mem ids(1));
   end
   if mem count-1 > 500
      for rr=1:NumPops
         gs del(['Pop',num2str(rr)],mem ids(2));
      end
   end
end
```

The function `gs del(...)` actually removes the chromosome strings from the populations.

With the population trimmed, chromosomes must be selected for the genetic operations. A call to the function `gs selr lofit(...)` selects chromosomes from each population randomly, but with the selection weighted towards those with *lower* fitness values. The functions `gs xover(...)` and `gs mut(...)` produce character strings by concatenating string portions from the selected chromosomes to produce new chromosomes. The parent chromosomes

```
parent1 = u15/u13+u14*u12 +u13/u11+u12/u10+u11*u1
parent2 = u6*u10+u15+u14 +u13+u12+u11
```

yield the crossover offspring chromosomes

```
offspring1 = u15/u13+u14*u12 +u13+u12+u11
offspring2 = u6*u10+u15+u14 +u13/u11+u12/u10+u11*u1
```

or the mutation offspring chromosomes

```
offspring1 = u15/u13+u14*u1+u13/u11+u12/u10+u11*u12
offspring2 = u6*u11+u15+u14+u13+u12+u10
```

.

This process corresponds to step 7, the new chromosome generation step, of table 6.2.

E.3 Evaluation of New Chromosomes

The crossover and mutation functions generate character strings, not numerical values. Therefore it is necessary to again extract the strings, convert them to numerical values, check them against the constraints, and assign fitness values to them.

```
for off = 1:length(off ids)
   chr=[];
   for rr = 1:NumPops
      chr=strvcat(chr,[gs get(['Pop',num2str(rr)],off ids(off))]);
   end
   for rr = 1:  numrec
      recloc(rr,:)=[eval(chr(rr,:))  eval(chr(rr+numrec,:))
                    eval(chr(2*numrec+1,:))  eval(chr(2*numrec+2,:))];
   end
   for z=1:numrec
      constraint(z,:)=[abs(recloc(z,1)) abs(recloc(z,2))];
   end
   if constraint<=[ones(numrec,1),ones(numrec,1)]
      fitness = Jfunc(recloc,xi,eta,Dlam,arc,steps,a,b,iorb,RAorb,nuorb,RAtarg,dectarg);
      for rr = 1:NumPops
         mem id = gs set fit(['Pop',num2str(rr)],off ids(off),fitness);
      end
   else
      for rr = 1:NumPops
         mem del = gs del(['Pop',num2str(rr)],off ids(off));
      end
   end
end
```

E.4 Search Termination

Most genetic searches execute for a proscribed number of generations. The extended computations necessary and high infant mortality in these searches suggest a large value for `NumGenerations`, but even that is insufficient to ensure convergence. Wrapping a `while` loop around the entire genetic search routine allows for user extension of the search and preserves the current populations.

```
UserContinue='Y';
ManLoop=0;
while UserContinue=='Y'

   Genetic Search Loop

   UserContinue=input(['Want another',num2str(NumGenerations),' generations?'],'s');
   ManLoop=ManLoop+1;
end
```

A screen output (only every 50 generations, to reduce system slow-down) of a history of the best current fitness value supports a user decision of whether or not to continue the search for another set of `NumGenerations` or allow the search to terminate.

Appendix F. Extended Results

This appendix contains the results of additional solutions beyond those directly cited in the main text.

F.1 Other General Planar Formations

To generate the monotonically decreasing plot of figure 6.23, additional optimizations were performed. Each assumed perfect viewing geometry to the source.

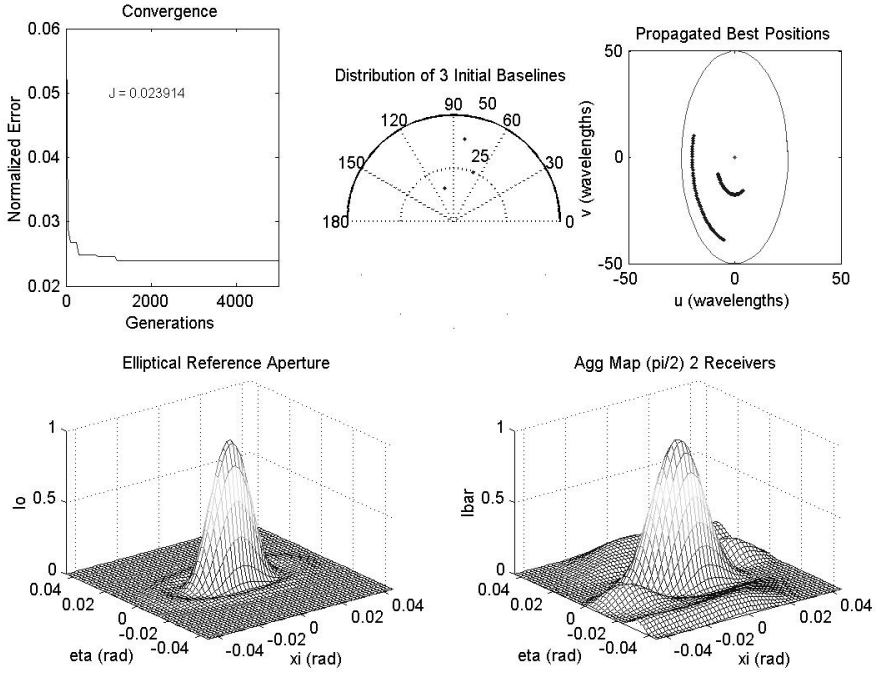

Figure F.1 A three-receiver formation has four degrees of freedom, and a yields a surprisingly close approximation to the reference aperture. This error was *not* included in figure 6.23 since it dominated the ordinate axis.

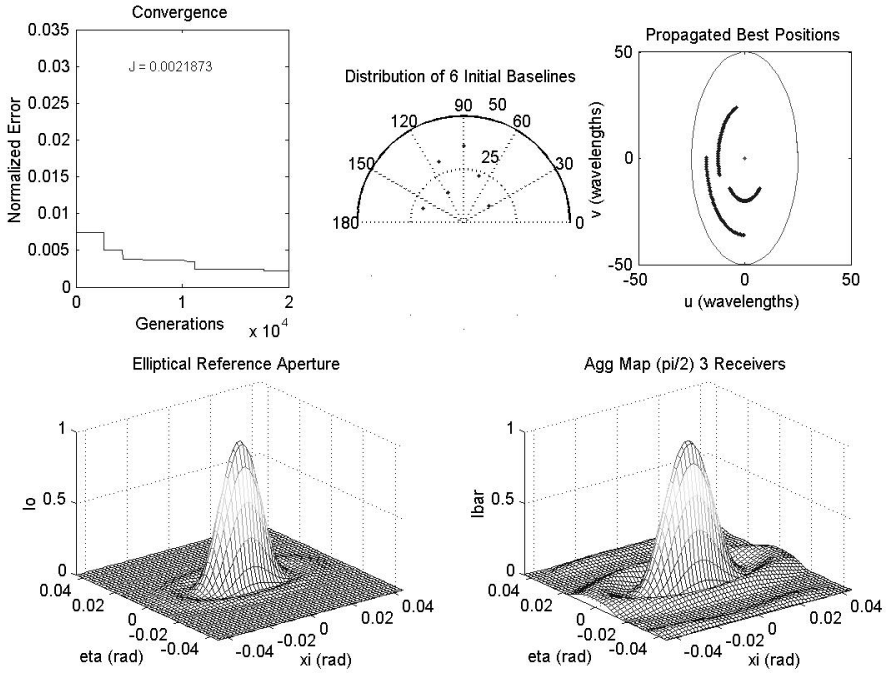

Figure F.2 With one receiver frozen at the center, a planar four-receiver formation has six degrees of freedom.

F.2 Other Planar Formations for Inertial Targets

The inertial targeting algorithms of chapter VII were further exercised for larger formations. Using the same four stellar targets as the five and six receiver formations described in section 7.5, the formations were expanded to 7, 9, and 11 receivers.

F.2.1 Seven Receiver Formations. Expanding the formation further to seven receivers (six movable) yields closer fidelity mimicry of the filled aperture.

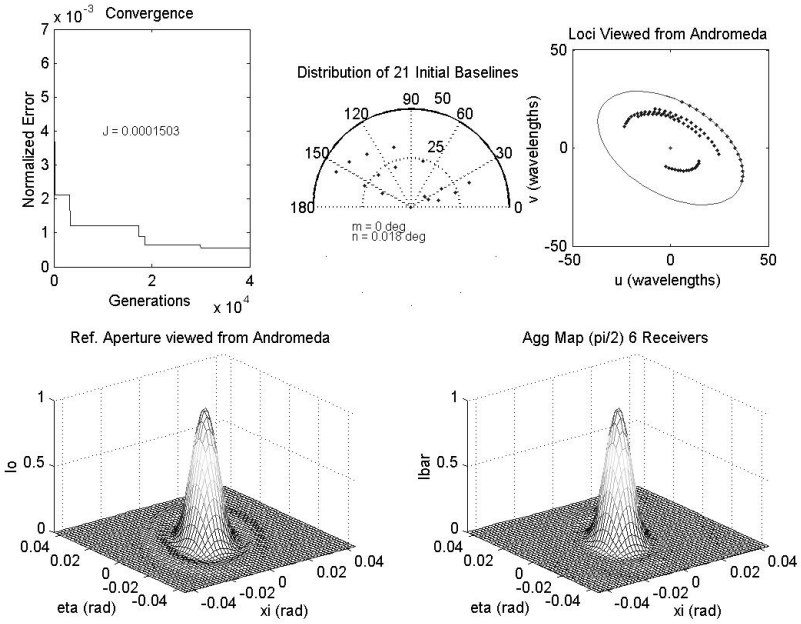

Figure F.3 Optimally placing six of seven receivers to image Andromeda yields these loci.

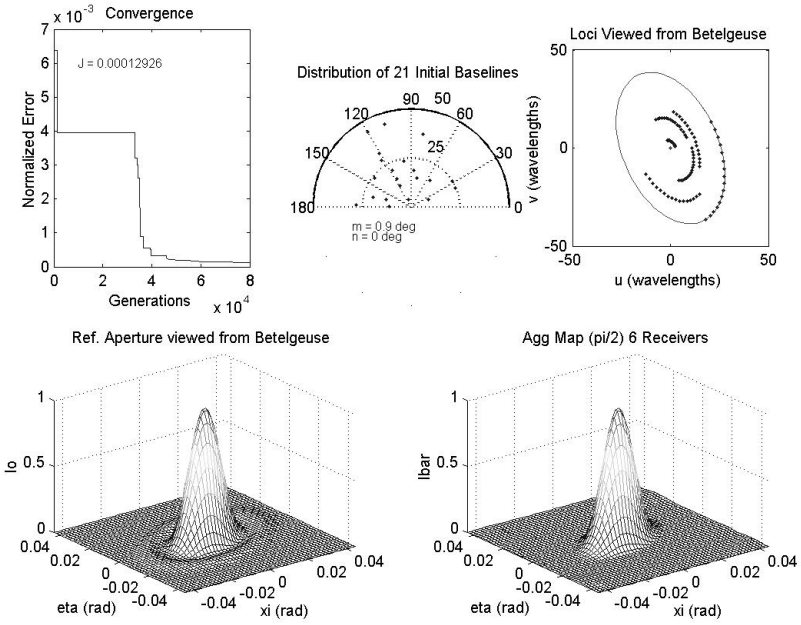

Figure F.4 Reoptimizing the same seven receivers for Betelgeuse yields these loci.

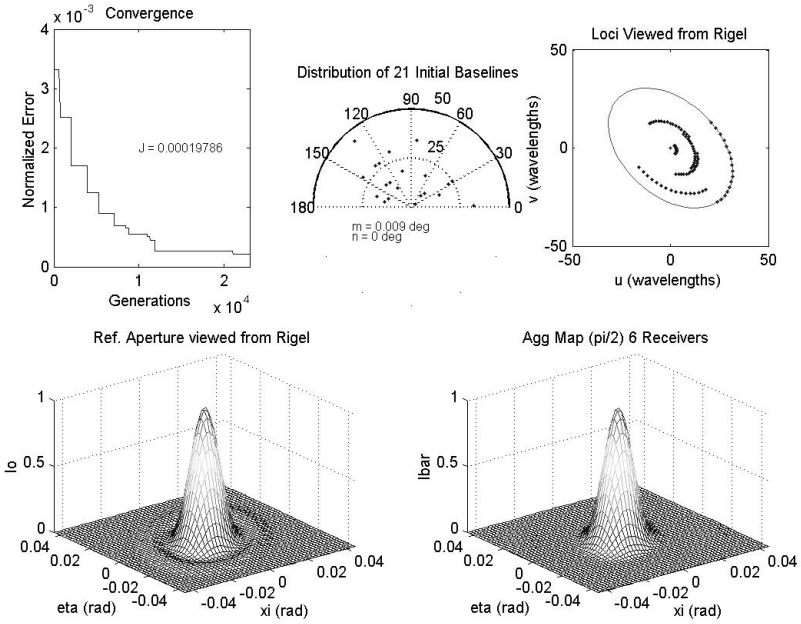

Figure F.5 Seven optimally placed receivers for viewing Rigel yields these loci.

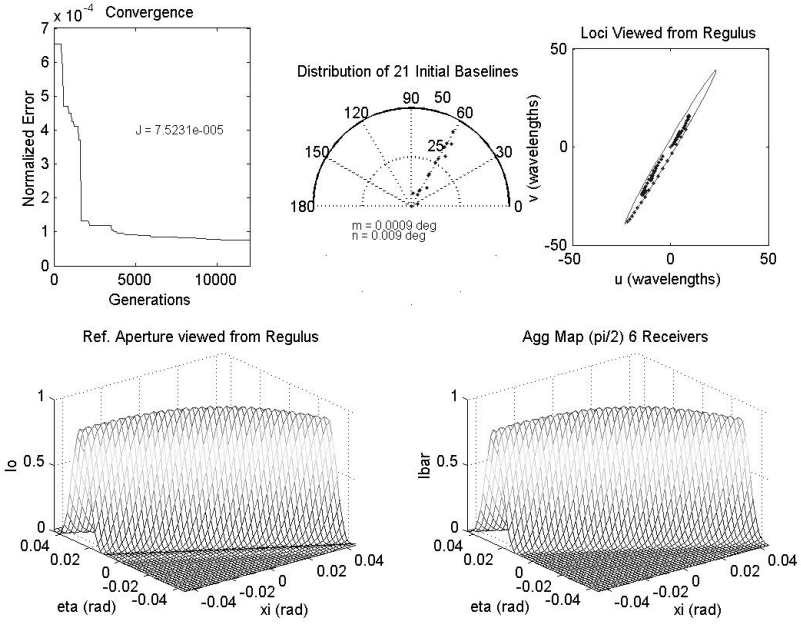

Figure F.6 Regulus's optimum placement of six receivers in the seven receiver formation.

F.2.2 Nine Receiver Formations. Expanding the formation further to nine receivers (eight movable) shows marginal improvements in synthesizing the filled aperture.

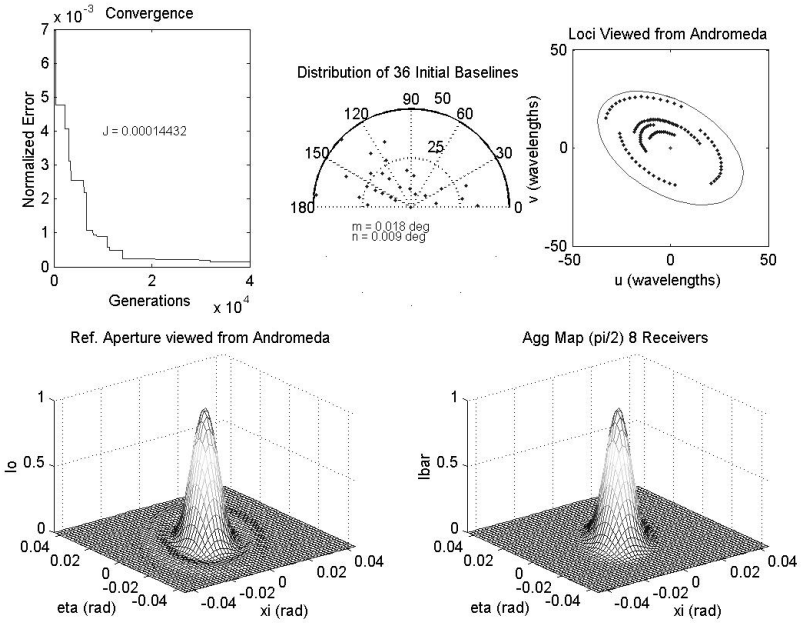

Figure F.7 Optimally placing eight of nine receivers to image Andromeda yields these loci.

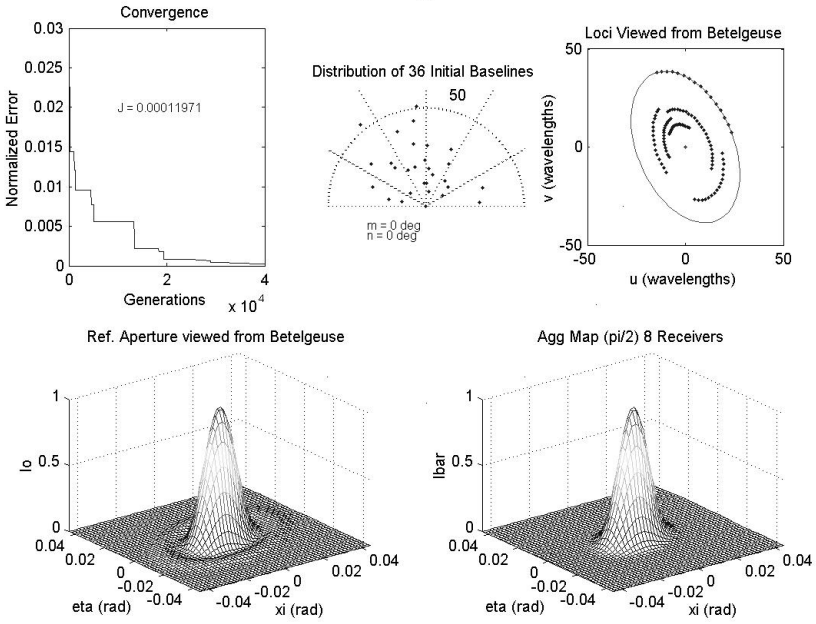

Figure F.8 Reoptimizing the same nine receivers for Betelgeuse yields these loci.

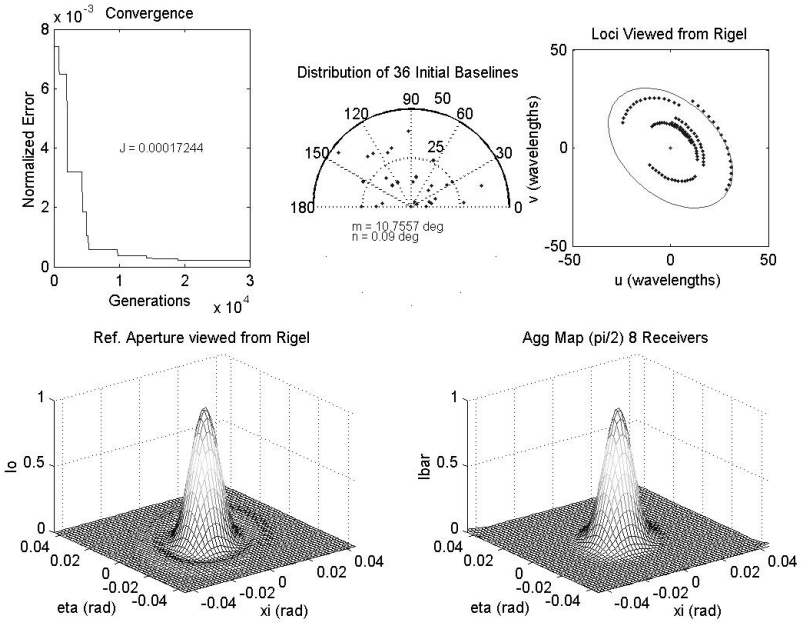

Figure F.9 Nine optimally placed receivers for viewing Rigel yields these loci.

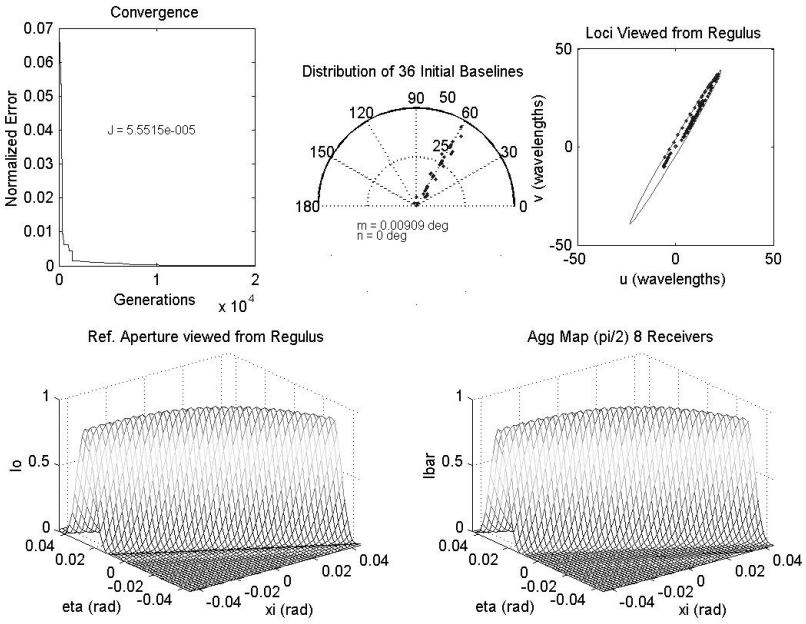

Figure F.10 Regulus's optimum placement of eight receivers in the nine receiver formation.

F.2.3 Eleven Receiver Formations. Expanding the formation further to eleven receivers (ten movable) shows marginal improvements in mimicking the filled aperture.

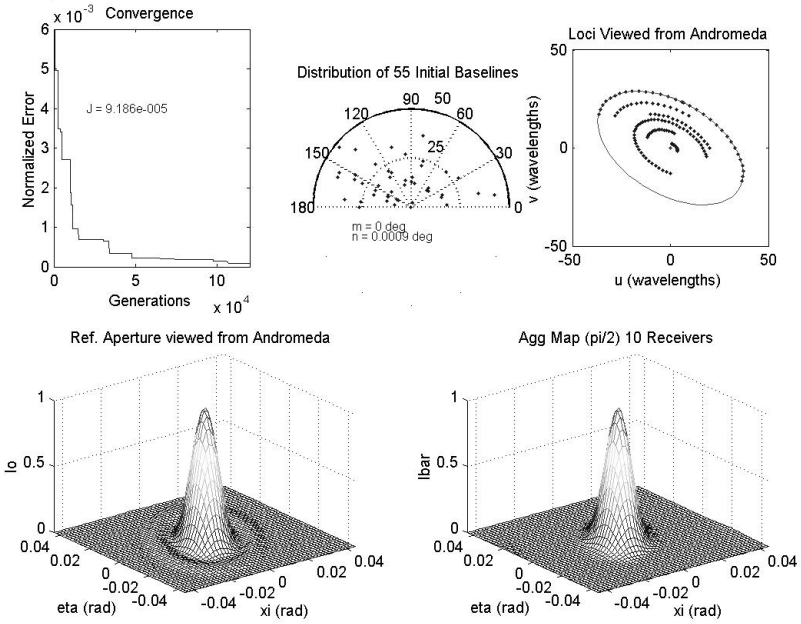

Figure F.11 Andromeda with eleven (ten movable) receivers has 22 degrees of freedom.

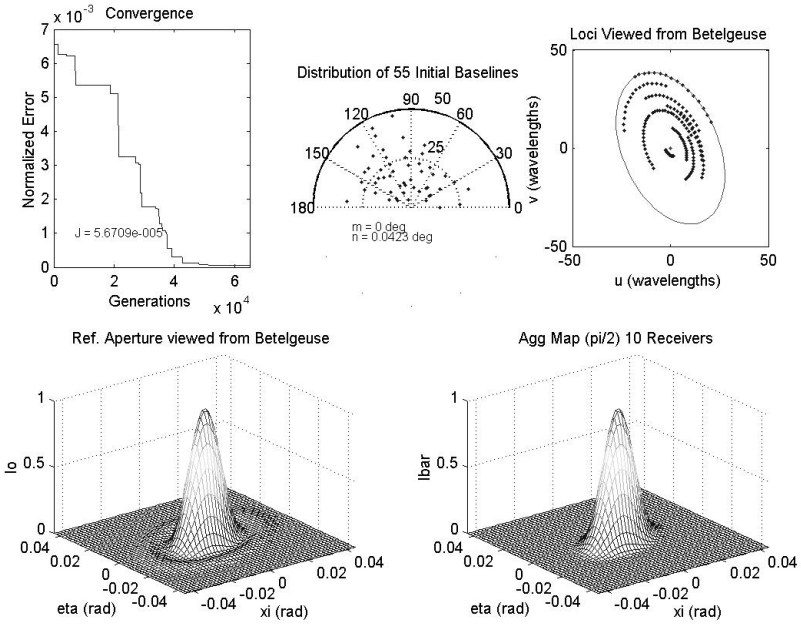

Figure F.12 Reoptimizing the formation with eleven receivers for Betelgeuse yields these loci.

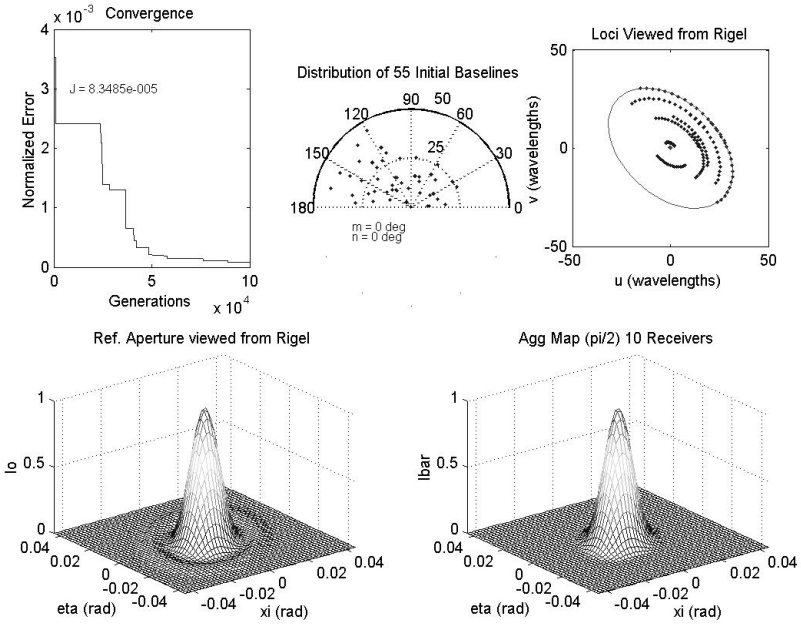

Figure F.13 Eleven optimally placed receivers for viewing Rigel yields these loci.

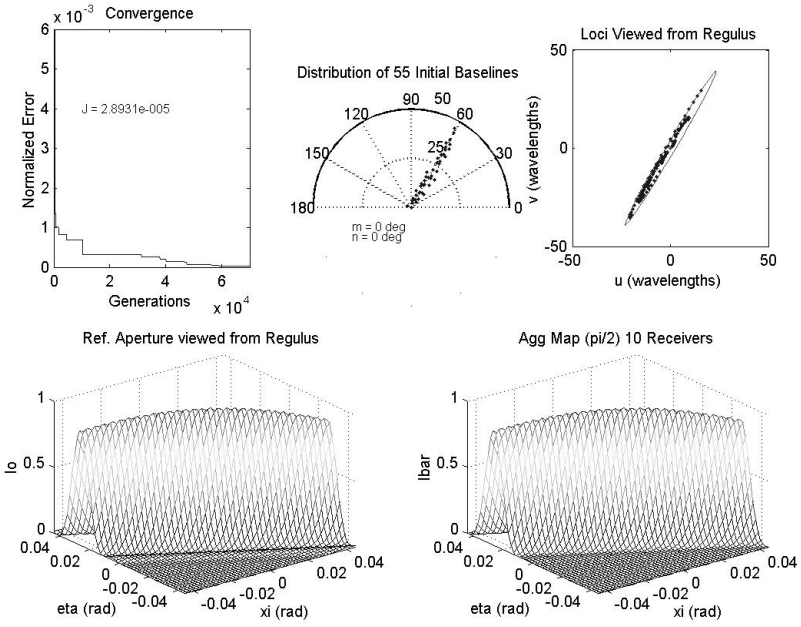

Figure F.14 Regulus's optimum placement of ten receivers in the eleven receiver formation.

Bibliography

1. Bordner, Ralph E. III. *Estimation of Relative Satellite Formation Element Positions in Near Circular Orbits*. MS thesis, Air Force Institute of Technology, 2001.

2. Bracewell, R. N. "Optimum Spacings for Radio Telescopes with Unfilled Apertures," *Progress in Scientific Radio*, *Vol. 1468*:pp. 243–244 1966.

3. Buckingham, E. "On Physically Similar Systems: Illustrations of the Use of Dimensional Equations," *Physics Review*, *Vol. 4* (No. 4):pp. 345–376 1914.

4. Chichka, David F. "Satellite Clusters with Constant Apparent Distribution," *Journal of Guidance, Control, and Dynamics*, *Vol. 24*:pp. 117–122 2001.

5. Clohessy, W. H. and Wiltshire, R. S. "Terminal Guidance System for Satellite Rendezvous," *Journal of the Aerospace Sciences*, *Vol. 27*:pp. 653–674 1960.

6. Cornwell, T. J. "Imaging at Radio Wavelengths," ESA SP-273. *ESA Workshop on Optical Interferometry in Space*. Grenada, Spain. June 16-18 1987.

7. Cornwell, T. J. "A Novel Principle for Optimization of the Instantaneous Fourier Plane Coverage of Correlation Arrays," *IEEE Transactions on Antennas and Propagation*, *Vol. 36* (No. 8):pp. 1165–1167 August 1988.

8. D'Angelo, Henry. *Linear Time-Varying Systems: Analysis and Synthesis*. 470 Atlantic Avenue, Boston: Allyn and Bacon, Inc., 1970.

9. DeCou, Anthony B. "Orbital Station-Keeping for Multiple Spacecraft Interferometry," *The Journal of the Astronautical Sciences*, *Vol. 39* (No. 3):pp. 283–297 July-September 1991.

10. Fogiel, M. *Handbook of Mathematical, Scientific, and Engineering Formulas, Tables, Functions, Graphs, and Transforms* (Fourth Edition). 61 Ethel Road West, Piscataway, New Jersey 08854: Research and Education Association, 1997.

11. Greenwood, Donald T. *Classical Dynamics*. New York: Dover Publications Inc., 1977.

12. Guelman, M. and Aleshin, M. "Optimal Bounded Low-Thrust Rendezvous with Fixed Terminal-Approach Direction," *Journal of Guidance, Control, and Dynamics*, *Vol. 24*:pp. 378–385 2001.

13. Hecht, Eugene. *Optics* (Third Edition). Reading Massachusetts: Addison Wesley Longman, Inc., 1998.

14. Hill, G. W. "Researches in the Lunar Theory," *American Journal of Mathematics*, *Vol. 1* (No. 1):pp. 5–26 1878.

15. Irvin, David J. Jr. *A Study of Linear vs. Nonlinear Control Techniques for the Reconfiguration of Satellite Formations*. MS thesis, Air Force Institute of Technology, 2001.

16. Jilla, Cyrus D. and Miller, David W. and Sedwick, Raymond J. "Application of Multidisciplinary Design Optimization Techniques to Distributed Satellite Systems," *Journal of Spacecraft and Rockets*, *Vol. 37*(No. 4):pp. 481–490 July-August 2000.

17. Johnston, M. Daniel and Nock, Kerry T. "Free Flyer Optical Interferometry Trajectory Analysis." *Workshop Proceedings: Technologies for Optical Interferometry in Space*. September 1991.

18. Kang, Wei and Sparks, Andy and Banda, Siva. "Coordinated Control of Multisatellite Systems," *Journal of Guidance, Control, and Dynamics*, *Vol. 24*:pp. 360–368 2001.

19. Kibblewhite, Edward. "Astronomical Criterial for Interferometric Arrays," ESA SP-226. *Colloquium on Kilometric Optical Arrays in Space*. Cargese, Corsica, France. October 1984.

20. Kong, Edmund M. and Miller, David W. "Optimization of Separated Spacecraft Interferometer Trajectories in the Absence of a Gravity-Well," SPIE 3350-13. *Astronomical Interferometry Conference*. Kona, Hawaii. March 1998.

21. Kong, Edmund M. and Miller, David W. and Sedwick, Raymond J. *Optimal Trajectories and Orbit Design for Separated Spacecraft Interferometry*. DSS MIT AFRL Contract No. 96-01, NASA Langley Research Center: Massachussets Institute of Technology, November 1998.

22. Kong, Edmund M. C. and Miller, David W. and Sedwick, Raymond J. "Exploiting Orbital Dynamics for Aperture Synthesis Using Distributed Satellite Systems: Applications to a Visible Earth Imager System," *The Journal of the Astronautical Sciences*, *Vol. 47*(Nos. 1 and 2):pp. 53–75 January-June 1999.

23. Mallory, G. J. and Jilla, C. D. and Miller, D. W. "Optimization of Geosynchronous Satellite Constellations for Interferometric Earth Imaging," *AIAA 98-4379* 1998.

24. Maybeck, Peter S. *Stochastic Models, Estimation, and Control, Volume 1*. Arlington: Navtech Book and Software Store, 1994.

25. Meirovitch, Leonard. *Methods of Analytical Dynamics* (first Edition). Advanced Engineering Series, New York: McGraw-Hill Book Company, 1970.

26. Menon, P. K. and Cheng, V. H. L. and Lam, T. and Crawford, L. S. and Sweriduk, G. D. and Dewell, L. D. *Genetic Search Toolbox for MATLAB and SIMULINK* (First Edition). 4966 El Camino Real, Suite 108, Los Altos, CA 94022: Optimal Synthesis Inc., 1998.

27. Napier, Peter J. and Thompson, A. Richard. "The Very Large Array: Design and Performance of a Modern Synthesis Radio Telescope," *Proceedings of the IEEE*, *Vol. 71*(No. 11):pp. 1295–1320 November 1983.

28. Noordam, J. E. and Atherton, P. D. and Greenaway, A. H. "OASIS: Optical Aperture Synthesis in Space," ESA SP-226. *Colloquium on Kilometric Optical Arrays in Space*. Cargese, Corsica, France. October 1985.

29. Ogata, Katsuhiko. *Modern Control Engineering*. New Jersey: Prentice Hall, 1997.

30. Parker, T. W. and Jacques, D. R. "Advanced Metrics for Optimizing Satellite Formation Geometries for Interferometry Missions," *submitted to Journal of Guidance, Control, and Dynamics* July 2002.

31. Parker, T. W. and Jacques, D. R. "Mean Performance Optimization of an Orbiting Distributed Aperture by Shaped Aperture Image Plane Comparisons," *submitted to AAS Journal of the Astronautical Sciences* July 2002.

32. Parker, T. W. and Jacques, D. R. and Wiesel, W. E. "Advanced Metrics for Optimizing Satellite Formations Performing Interferometry Missions," *to appear in Proceedings of AIAA/AAS Astrodynamics Specialist Conference*, (AIAA-2002-4740) August 2002. Monterey, California.

33. Preston, R. A. and Burke, B. F. and Doxsey, R. and Jordan, J. F. and Morgan, S. H. and Roberts, D. H. and Shapiro, I. I. "The Future of VLBI Observatories in Space," SPIE 3350-13. *Very Long Baseline Interferometry Techniques*. 111 rue Nicolas-Vauquelin 31100 Toulouse, France. 1983.

34. Rahmat-Samii, Yahya and Michielssen, Eric. *Electromagnetic Optimization by Genetic Algorithms* (First Edition). 605 Third Avenue, New York: John Wiley and Sons, Inc., 1999.

35. Rohlfs, Kristen and Wilson, Thomas L. *Tools of Radio Astronomy* (Third Edition). Astronomy and Astrophysics Library, Berlin, Heidelberg: Springer-Verlag, 2000.

36. Sabol, Chris and Burns, Richard and McLaughlin, Craig A. "Satellite Formation Flying Design and Evolution," AAS 99-121. *AAS/AIAA Space Flight Mechanics Meeting*. Breckenridge, Colorado. February 1999.

37. Schaub, Hanspeter and Alfriend, Kyle T. "J_2 Invariant Relative Orbits for Spacecraft Formations," *NASA Flight Mechanics Symposium* 1999.

38. Sedwick, R. J. and Hacker, T. L. and Miller, D. W. "Optimum Aperture Placement for a Space-Based Radar System Using Separated Spacecraft Interferometry," AIAA-99-4271. August 1999.

39. Sedwick, R. J. and Kong, E. M. C. and Miller, D. W. "Exploiting Orbital Dynamics and Micropropulsion for Aperture Synthesis Using Distributed Satellite Systems: Applications to TechSat 21," AIAA-98-5289. *Defense & Civil Space Programs Conference & Exhibit*. Huntsville, AL. October 28-30 1998.

40. Sedwick, R. J. and Miller, D. W. and Kong, E. M. C. "Mitigation of Differential Perturbations in Formation Flying Satellite Clusters," *The Journal of the Astronautical Sciences*, *Vol. 47*(Nos. 3 and 4):pp. 309–331 July-December 1999.

41. Space Vehicles Directorate, AFRL. "TechSat 21 - Space Missions Using Satellite Clusters," *http:/www.vs.afrl.af.mil/TechProgs/TechSat21/NGSC.html* 2001.

42. Stachnik, R. V. and Gezari, D. Y. "SAMSI: An Orbiting Spatial Interferometer for Micro-Arcsecond Astronomical Observations," ESA SP-226. *Colloquium on Kilometric Optical Arrays in Space*. Cargese, Corsica, France. October 1985.

43. Stakgold, Ivar. *Green's Functions and Boundary Value Problems*. New York: John Wiley and Sons Inc., 1998.

44. Thomas, George B. Jr. and Finney, Ross L. *Calculus and Analytic Geometry* (Sixth Edition), *Vol. 1*. Reading, Massachusetts: Addison-Wesley Publishing Company, 1984.

45. Thompson, A. Richard and Clark, B. G. and Wade, C. M. and Napier, Peter J. "The Very Large Array," *The Astrophysical Journal Supplement Series*, *Vol. 44*:pp. 151–167 October 1980.

46. Thompson, A. Richard and Moran, James M. and Jr., George W. Swensen. *Interferometry and Synthesis in Radio Astronomy*. Malabar, Florida: Krieger Publishing Company, 1998.

47. University of Wisconsin-Madison, Astronomy Department. "The Constellations and Their Stars," *http://www.astro.wisc.edu/dolan/constellations/constellationlist.html* 2002.

48. Wheeler, Anthony J. and Ganji, Ahmad R. *Introduction to Engineering Experimentation* (First Edition). Upper Saddle River, New Jersey 07458: Prentice Hall, 1996.

49. Wiesel, William E. *Spaceflight Dynamics*. New York: McGraw-Hill, Inc., 1989.

50. Wiesel, William E., "Advanced Astrodynamics." class notes for Mechanical Engineering 636, Air Force Institute of Technology, Wright Patterson AFB, January 2000.

51. Wiesel, William E., "Optimal Impulsive Control of Relative Satellite Motion." submitted to *Journal of Guidance, Control, and Dynamics*, November 2000.

52. Wiesel, William E., "Perturbations of Relative Satellite Motion about an Oblate Planet." submitted to *Journal of Guidance, Control, and Dynamics*, July 2000.

53. Wiesel, William E. "The Dynamics of Relative Satellite Motion," AAS 01-163. Santa Barbara, California. February 11-14 2001.

54. Wiesel, William E. "Relative Satellite Motion about an Oblate Planet," *Journal of Guidance, Control, and Dynamics*, *Vol. 25*(No. 4):pp. 776–785 July-August 2002.

55. Yeh, Hsi-Han and Nelson, Eric and Sparks, Andrew. "Nonlinear Tracking Control for Satellite Formations," *draft* 2001.

56. Yeh, Hsi-Han and Sparks, Andrew. "Geometry and Control of Satellite Formations." *Proceedings of the American Control Conference*. June 2000.

Vita

Major Timothy W. Parker, born in Okinawa, Japan, is a 1984 graduate of Wahkiakum High School in Cathlamet, Washington. He earned his bachelors degree in aeronautics and astronautics engineering in 1988 from the University of Washington in Seattle, Washington at which time he received a commission in the Air Force through ROTC. His initial assignment was with the 1st Space Operations Squadron at Schriever Air Force Base, Colorado where he performed launch and early orbit operations on Defense Support Program (DSP) early warning satellites, Defense Meteorological Satellite Program (DMSP) weather satellites, and Global Positioning System (GPS) navigation satellites. From 1991-93 he completed his masters program in aerospace engineering at the University of Colorado at Colorado Springs, specializing in high efficiency rocket design. He was then assigned to the 392nd Training Squadron at Vandenberg Air Force Base where he was an instructor and curriculum developer for Undergraduate Space and Missile Training. In 1997, he was assigned to the 76th Space Operations Squadron at Schriever Air Force Base where he served on the Air Force Space Support Teams (AFSST), deploying to exercises and real operations worldwide, including tours to Bahrain in support of SOUTHERN WATCH (Iraq) and Italy in support of DELIBERATE FORGE (Bosnia). In 1999 he came to the Air Force Institute of Technology for his PhD program under the direction of Lt Col David R. Jacques.

REPORT DOCUMENTATION PAGE

Form Approved
OMB No. 0704-0188

1. REPORT DATE *(DD-MM-YYYY)*	2. REPORT TYPE	3. DATES COVERED *(From - To)*
10-09-2002	Doctoral Dissertation	Sep 1999 - Sep 2002

4. TITLE AND SUBTITLE

MEAN PERFORMANCE OPTIMIZATION OF AN ORBITING DISTRIBUTED APERTURE BY WARPED APERTURE IMAGE PLANE COMPARISONS

5a. CONTRACT NUMBER

5b. GRANT NUMBER

5c. PROGRAM ELEMENT NUMBER

6. AUTHOR(S)

Parker, Timothy W., Major, USAF

5d. PROJECT NUMBER

5e. TASK NUMBER

5f. WORK UNIT NUMBER

7. PERFORMING ORGANIZATION NAME(S) AND ADDRESS(ES)

Air Force Institute of Technology
Graduate School of Engineering and Management (AFIT/EN)
2950 P Street, Building 640
WPAFB OH 45433-7765

8. PERFORMING ORGANIZATION REPORT NUMBER

AFIT/DS/ENY/02-3

9. SPONSORING/MONITORING AGENCY NAME(S) AND ADDRESS(ES)

AFRL/VACA
Attn: Dr. Andrew Sparks
2210 Eighth Street
Wright Patterson AFB, OH 45433-7521
DSN: 785-8682
e-mail: Andrew.Sparks@wpafb.af.mil

10. SPONSOR/MONITOR'S ACRONYM(S)

11. SPONSOR/MONITOR'S REPORT NUMBER(S)

12. DISTRIBUTION/AVAILABILITY STATEMENT

APPROVED FOR PUBLIC RELEASE; DISTRIBUTION UNLIMITED

13. SUPPLEMENTARY NOTES

14. ABSTRACT

This work models the aggregate performance of satellite receiver formations functioning as orbiting interferometers as compared to filled apertures of similar geometries.These models facilitate selecting initial conditions for formations such that their control-free dynamics yield interferometry performance with minimal errors as compared to the filled apertures. The solution method draws on the dynamic models of an orbiting planar satellite formation to define the size and shape of a reference aperture and to define the degrees of freedom for the formation members. The paths of formation elements yield geometries for which the aggregate performance of the array of discrete receivers may be calculated. The objective of the optimization process is therefore minimizing the time-averaged square of the difference between the filled aperture's intensity map and that generated by the discrete receiver array. This yields a formation whose configuration offers minimum errors for imaging processes beginning at any arbitrary start time. The problem as posed is non-convex, and requires implementation of a global search method. Genetic algorithms are used. The solution method includes a new analytic solution for the intensity map of an elliptical aperture and a technique for generalizing this solution to include the effects of non-ideal viewing geometries.

15. SUBJECT TERMS

Satellite Formations, Interferometry, Optimization, Genetic Algorithms, Synthetic Apertures

16. SECURITY CLASSIFICATION OF:			17. LIMITATION OF ABSTRACT	18. NUMBER OF PAGES	19a. NAME OF RESPONSIBLE PERSON
a. REPORT	b. ABSTRACT	c. THIS PAGE			David R. Jacques, Lt Col, USAF (ENY)
U	U	U	UU	156	19b. TELEPHONE NUMBER *(Include area code)* (937) 255-3069; e-mail David.Jacques@afit.edu